Reaction rim growth in the systems $MgO\text{-}SiO_2$ and $CaO\text{-}MgO\text{-}SiO_2$: Diffusion pathways and the effect of water

vorgelegt von

Diplom-Geowissenschaftler

Bastian Joachim

aus Bremen

Von der Fakultät VI Planen | Bauen | Umwelt der Technischen Universität Berlin zur Erlangung des akademischen Grades

Doktor der Naturwissenschaften

Dr. rer. nat. genehmigte Dissertation

Promotionsausschuss:

Vorsitzender: Prof. Dr. rer. nat. Dietmar Stephan
Berichter: Prof. Dr. rer. nat. Wilhelm Heinrich
Berichter: Prof. Dr. rer. nat. Gerhard Franz
Berichter: Prof. Dr. rer. nat. Rainer Abart

Tag der wissenschaftlichen Aussprache: 13.07.2011

Berlin 2011

D83

Danksagung

Ich möchte mich bei Kollegen, Helfern und Freunden bedanken, welche diese Arbeit erst ermöglicht haben.

Zuerst möchte ich mich bei meinem Betreuer Wilhelm Heinrich und bei Rainer Abart bedanken, die jederzeit bereit für Diskussionen waren und mich in jeglicher Hinsicht unterstützt haben. Hierzu zählt nicht nur die wissenschaftliche Diskussion sondern auch die Ermöglichung zahlreicher Konferenzbesuche und Forschungsaufenthalte sowie Rat bei allen anderen Problemen und Anliegen, die während einer Doktorarbeit auftreten können. Weiterhin danke ich Gerhard Franz, der die Promotion an der TU Berlin kurzfristig ermöglicht hat. Ein weiterer Dank gilt der Deutschen Forschungsgemeinschaft für die Finanzierung dieser Arbeit im Rahmen der Forschergruppe 741. Insbesondere möchte ich mich bei Emmanuel Gardés bedanken, der jederzeit ein Ansprechpartner in wissenschaftlichen und menschlichen Fragen war und wesentlich zum Gelingen dieser Arbeit beigetragen hat. Für Ideen, Verbesserungsvorschläge und Kommentare zu dieser Arbeit möchte ich mich bei Svenja Germerott bedanken. Für die Unterstützung bei Versuchen an der IHPV und dem Pistonzylinder bedanke ich mich bei Bernd Wunder, Max Wilke, Andreas Ebert und Rainer Schulz. Ein großer Dank gilt Hans Peter Nabein, der bei fast allen Problemen, die am Rechner oder im Labor auftraten eine Lösung hatte. Für ihre Hilfe bei der Probenpräparation danke ich Gerhard Berger, Matthias Kreplin und Otto Diedrich. Weiterhin möchte ich mich bei Oona Appelt und Dieter Rhede bedanken, die eine große Hilfe bei den Mikrosondenmessungen waren und auch mal kurzfristig Messzeit ermöglichten. Anja Schreiber danke ich für das Schneiden von FIB-Folien und Richard Wirth für seinen Support bei TEM-Messungen. Ein weiterer Dank gilt Monika Koch-Müller für ihre Geduld und Hilfe bei infrarotspektrokopischen Messungen. Roland Stalder und Felix Prechtel danke ich für die Einladung nach Innsbruck und die Unterstützung bei der Erstellung von IR-mappings. Ganz besonders danken möchte ich allen Mitarbeitern der Sektion 3.3. des GFZ-Potsdam, die jederzeit hilfsbereit waren. Ein weiterer Dank gilt Gregor und Ralf von der FU Berlin sowie Parveen. Bei Dan Harlov möchte ich mich vor allem für seine Hilfe während der AGU bedanken. Weiterhin danke ich allen, die meine Zeit in Berlin während und abseits der Arbeit zu etwas Unvergesslichem gemacht haben. Und schließlich möchte ich mich ganz besonders bei Maria, Nic, Marie, Josepha, meiner Familie und speziell bei Svenja bedanken, die immer da waren, vor allem als es besonders darauf ankam.

Table of contents

1. Summary

Growth of reaction rims and metamorphic coronas is recorded in many metamorphic rocks. Many parameters such as pressure, temperature, time, the chemical composition of a system or the presence of fluids may affect reaction rim growth. Laboratory experiments are the method of choice to derive transport mechanisms, reaction rates and component mobilities in polycrystalline rims as a function of these parameters. At the beginning of this study, data only existed for simple binary systems. The major goal of this study is to derive component mobilities in rim growth experiments in the ternary system CaO-MgO-SiO_2 and get based on that a better understanding of the growth of complex natural coronas.

Chapter 3.1. provides a general introduction in metamorphic coronas and shows sequences and textures of different complexity found in nature. In chapter 3.2. already performed laboratory experiments in binary systems and pathways for diffusion of components in a polycrystalline reaction rim are introduced. Chapter 3.3. gives an introduction in the effect of water on reaction rim growth, which significantly enhances growth rates of monomineralic rims. This has already been observed in studies dealing with experiments as well as natural samples. Chapter 3 concludes with the goals of this study, which have all in common to gain a better understanding of the growth of complex natural reaction rims.

Chapter 4 describes performed experiments in the piston cylinder apparatus and Internally Heated Pressure Vessel (IHPV) and the analytical methods. The results of this thesis are presented and discussed in chapter 5, 6 and 7.

In chapter 5, growth of a monomineralic, polycrystalline åkermanite ($Ca_2MgSi_2O_7$) reaction rim between monticellite ($CaMgSiO_4$) and wollastonite ($CaSiO_3$) is described. Rim growth is solely controlled by MgO-diffusion with $D^{Ak}_{eff,MgO} = 10^{-15.8\ +/-\ 0.1}\ m^2s^{-1}$ at 1200°C and 0.5 GPa. Between 1000°C and 1200°C, the effective bulk diffusion coefficient follows an Arrhenius law with $E_a = 204 \pm 18$ kJ/mol and $D_0 = 10^{-8.6\ +/-\ 1.6}\ m^2s^{-1}$. With increasing run duration, growth of åkermanite grains led to a successive decrease of the grain boundary area fraction. This does not affect $D^{Ak}_{eff,MgO}$, which implies that rim growth is essentially controlled by volume diffusion.

Chapter 6 focuses on the effect of small, undefined amounts of water on the microstructure of bimineralic diopside ($CaMgSi_2O_6$) - merwinite ($Ca_3MgSi_2O_8$) reaction rims growing between monticellite and wollastonite at 900°C and 1.2 GPa. Overall rim

growth rates are solely controlled by diffusion of MgO with $D^{di+mer}_{eff,bulk,MgO} = 10^{-16.3 +/- 0.2}$ m^2s^{-1} and are not affected by increasing water concentration at least in the range of the conditions used in this study. A "cellular" microstructure develops at relatively dry conditions when MgO is substantially more mobile than the other components CaO and SiO_2, whereas a "segregated multilayer" microstructure develops, if either CaO or SiO_2 or both have relatively high diffusivities that are comparable to MgO-diffusivities. The fact that a segregated microstructure develops at more humid conditions implies that small amounts of water may significantly change relative component mobilities and consequently the internal rim organization.

In chapter 7, the effect of small amounts of water on multilayered reaction rims is discussed. The usage of OH-doped periclase (MgO) as starting material provides a method to introduce very small controlled amounts of water in rim growth experiments. Growth of a forsterite (Mg_2SiO_4)-enstatite ($MgSiO_3$) double-layered reaction rim between periclase and quartz (SiO_2) in presence or absence of minute amounts of water shows that changes in the present water concentration affect the forsterite-enstatite thickness ratio and therefore the relative mobility of the growth rate controlling component(s) between the layers of a reaction rim. Rim growth reactions between periclase and wollastonite in presence of various water concentrations show that small amounts of water are a necessary catalyst to nucleate metamorphic reaction products. The water concentration that is required to nucleate åkermanite is smaller than for forsterite, followed by monticellite and finally merwinite. The final succession in presence of a water concentration allowing the nucleation of all product phases gives periclase | forsterite | monticellite | merwinite | åkermanite | wollastonite. In addition, the relative mobility of either CaO or SiO_2 or both compared to MgO increases with increasing water concentration, which may affect the layer sequence.

Consequently this study shows that minute amounts of water have not only an effect on the overall growth rate but also on the microstructure, the relative thickness ratio and the sequence and organization of reaction rims.

2. Zusammenfassung

Metamorphe Koronen und Reaktionssäume sind ein charakteristisches Merkmal zahlreicher natürlicher metamorpher Gesteine, deren Wachstum von Parametern wie Druck, Temperatur, Zeit, dem Chemismus der Ausgangsmaterialien oder der Verfügbarkeit von Fluiden beeinflusst wird. Anhand von Laborexperimenten lassen sich unter kontrollierten Bedingungen Transportmechanismen, Reaktionsraten und die Mobilität der beteiligten Komponenten in polykristallinen Reaktionssäumen bestimmen. Zu Beginn dieser Arbeit gab es bereits experimentelle Studien, die das Saumwachstum in vergleichsweise einfachen binären Systemen behandeln. Das Ziel dieser Arbeit ist es, Komponentenmobilitäten in experimentell produzierten Säumen im ternären Systems $CaO\text{-}MgO\text{-}SiO_2$ zu bestimmen und anhand dessen ein besseres Verständnis für das Wachstum natürlicher Reaktionssäume zu erlangen.

Kapitel 3.1. gibt eine Einleitung in die Thematik und zeigt Saumabfolgen natürlicher Proben von unterschiedlicher Komplexität. Bereits durchgeführte Laborexperimente in binären Systemen werden in Kapitel 3.2. zusammengefasst. Weiterhin werden mögliche Diffusionspfade in polykristallinen Säumen beschrieben. Kapitel 3.3. gibt einen Überblick über bestehende Modelle, welche Reaktionsraten und Komponentenmobilitäten in Abhängigkeit von den oben genannten Parametern in binären und Multikomponentensystemen beschreiben. In Kapitel 3.4. wird der bereits gezeigte Einfluss von Wasser auf die Wachstumsraten experimentell gebildeter monomineralischer und natürlicher Säume dargestellt. Kapitel 3 schließt mit den Fragestellungen, die in dieser Arbeit beantwortet werden sollen und alle zum Ziel haben, das Verständnis für das Wachstum natürlicher komplexer Reaktionssäume zu verbessern. Sowohl die im Piston Zylinder und der intern beheizten Gasdruckanlage (IHPV) durchgeführte Experimente als auch die verwendeten Analysemethoden werden in Kapitel 4 beschrieben. Ergebnisse und deren Diskussion sind in den Kapiteln 5, 6 und 7 aufgeführt.

Kapitel 5 behandelt das Wachstum eines einphasigen, polykristallinen Åkermanitsaumes ($Ca_2MgSi_2O_7$) zwischen Monticellit ($CaMgSiO_4$) und Wollastonit ($CaSiO_3$). Das Saumwachstum wird einzig durch die Diffusion von MgO kontrolliert und lässt sich anhand des effektiven Diffusionskoeffizienten $D^{Ak}_{eff,MgO} = 10^{-15.8 \pm 0.1}$ m^2s^{-1} bei 1200°C und 0.5 GPa beschreiben. Zwischen 1000°C und 1200°C folgt $D^{Ak}_{eff,MgO}$ einer Arrhenius-Beziehung mit $E_a = 204 \pm 18$ kJ/mol und $D_0 = 10^{-8.6 \pm 1.6}$ m^2s^{-1}. Mit zunehmender

Reaktionsdauer wachsen die Åkermanitkörner im Saum. Dies führt zu einer Abnahme der Anzahl von Korngrenzen pro Volumeneinheit, hat jedoch keine Auswirkungen auf $D^{Ak}_{eff,MgO}$, was darauf hindeutet, dass es sich bei dem Transport von MgO im Åkermanitsaum hauptsächlich um Volumendiffusion handelt.

In Kapitel 6 wird der Einfluss sehr kleiner Wassermengen auf das Wachstum und die Mikrostruktur von bimineralischen Diopsid ($CaMgSi_2O_6$) - Merwinit ($Ca_3MgSi_2O_8$) Säumen behandelt, die sich zwischen Monticellit und Wollastonit bei 1200°C und 1.2 GPa bilden. Die Saumwachstumsrate wird erneut ausschließlich durch die Diffusion von MgO kontrolliert und lässt sich mit $D^{di+mer}_{bulk,MgO} = 10^{-16.3 +/- 0.2}$ m^2 s^{-1} beschreiben. Die MgO-Mobilität wird nicht durch zunehmende Wasserverfügbarkeit, zumindest im Rahmen der vorliegenden Studie, beeinflusst. Eine zelluläre Mikrostruktur bildet sich bei vergleichsweise trockenen Bedingungen und nur wenn MgO deutlich mobiler ist als die übrigen Komponenten CaO und SiO_2. Eine lagige Mikrostruktur bildet sich, wenn entweder CaO oder SiO_2 oder beide Komponenten ähnlich hohe Mobilitäten aufweisen wie MgO. Die Tatsache, dass sich eine lagige Mikrostruktur im Vergleich zur zellulären Struktur bildet, wenn höhere Wassermengen verfügbar sind, lässt darauf schließen, dass die Verfügbarkeit von Wasser entscheidenden Einfluss auf die relativen Komponentenmobilitäten und folglich die Mikrostruktur von Reaktionssäumen hat.

In Kapitel 7 wird der Einfluss von kleinen Wassermengen auf mehrlagige Reaktionssäume diskutiert. Die Verwendung von OH-gedoptem Periklas (MgO) als Ausgangsmaterial gibt uns die Möglichkeit sehr kleine, quantifizierbare Wassermengen in Saumwachstumsexperimente einzubringen. Anhand des Wachstums eines Forsterit (Mg_2SiO_4)-Enstatit ($MgSiO_3$) Doppelsaumes lässt sich zeigen, dass Änderungen in der Wasserkonzentration das Dickenverhältnis der beiden Phasen und folglich das Verhältnis der relativen Mobilität der saumwachstumskontrollierenden Komponente(n) zwischen den einzelnen Phasen beeinflussen. Saumwachstumsexperimente zwischen Periklas und Wollastonit bei variierenden Wasserverkonzentrationen zeigen, dass Wasser für die Nukleation metamorpher Reaktionsprodukte benötigt wird. Die Wassermenge, welche für die Nukleation von Åkermanit benötigt wird, ist kleiner als diejenige für Forsterit, gefolgt von Monticellit und schließlich Merwinit. Die finale Abfolge bei ausreichend hoher Wasserkonzentration, welches die Nukleation aller Reaktionsprodukte ermöglicht, ist Periklas | Forsterit | Monticellit | Merwinit | Åkermanit | Wollastonit. Mit zunehmender Wasserkonzentration nimmt entweder die relative Mobilität von CaO oder SiO_2 oder

beider Komponenten im Vergleich zur MgO-Mobilität zu. Dies beeinflusst die Abfolge der Phasen innerhalb des Reaktionssaumes.

In dieser Arbeit wird gezeigt, dass Wasser nicht nur die Reaktionsrate, sondern auch die Mikrostruktur, das relative Dickenverhältnis und die Saumabfolge von Reaktionssäumen beeinflusst.

3. Introduction

3.1. Metamorphic coronas - reaction rim growth in nature

Reaction rims and metamorphic coronas are common features in many metamorphic rocks. They are the result of a non-equilibrium reaction between adjacent minerals. Rims or coronas separate reactants that were initially in contact and were metastable with respect to the pressure and temperature conditions of metamorphism. Figure 1 shows an example of a monomineralic naturally grown reaction rim in the three-component system CaO-SiO_2-CO_2 according to the reaction:

$$CaCO_3 + SiO_2 = CaSiO_3 + CO_2 \quad (1)$$

A quartz nodule that was found 100 m away from the Christmas Mountains contact aureole (Texas) shows a wollastonite reaction rim of 5 mm thickness that is separating the core from the calcite matrix (Joesten and Fisher 1988).

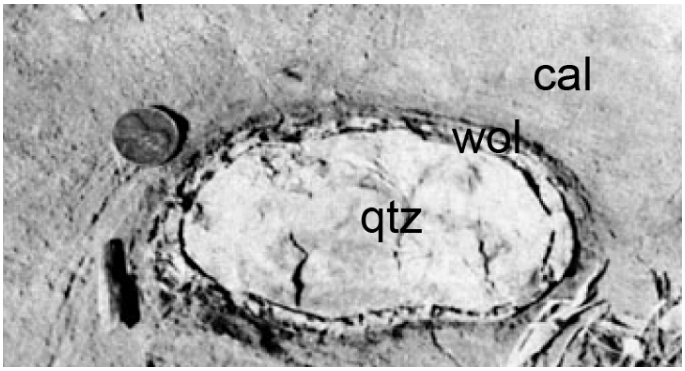

Fig.1: Natural monomineralic reaction rim consisting of a single wollastonite (wol) layer separating quartz (qtz) and calcite (cal) (from Joesten and Fisher 1988).

A very simple reaction rim may consist of a single monomineralic layer. However, very complex reaction rims showing bimineralic and multilayered sequences are observable in natural samples. In binary systems reaction educts and products always represent a straight line in compositional space, so that the individual layers are always monomineralic, if local equilibrium at the reaction interfaces is assumed. In systems that are composed of more than two components, crossing tie lines in compositional space between educts and products and consequently growth of bimineralic layers is possible. Figure 2 shows a garnet that was originally in contact with quartz and feldspar. At places where garnet was in contact with quartz, the rim consists of an internal symplectitic layer of cordierite and orthopyroxene, surrounded by a monomineralic layer of orthopyroxene. Where garnet was in contact with feldspar, the corona consists of an internal symplectitic

layer of cordierite and orthopyroxene, surrounded by an outer symplectitic layer of orthopyroxene and plagioclase.

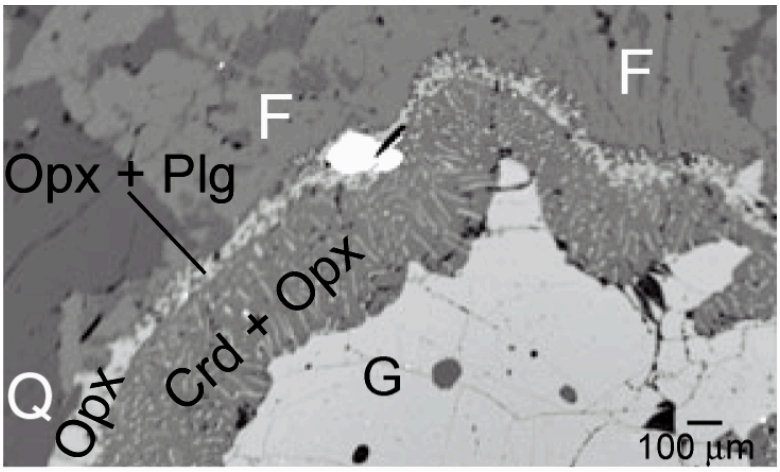

Fig.2: Natural garnet (G) that was originally in contact with quartz (Q) and feldspar (F, plagioclase and potassium feldspar). In regions where garnet was in contact with quartz, a double-layered rim consisting of symplectitic cordierite (Crd) and orthopyroxene (Opx) surrounded by monomineralic orthopyroxene, in regions where garnet was in contact with feldspar a double-layered rim consisting of symplectitic cordierite and orthopyroxene surrounded by symplectitic orthopyroxene and plagioclase (Plg) formed (modified after Carlson, 2010).

In a multi-component system very complex coronas may develop. Figure 3 displays an example published by Keller et al. 2008, which shows experimentally grown coronas at 900°C and 1.8 GPa in a natural gabbro.

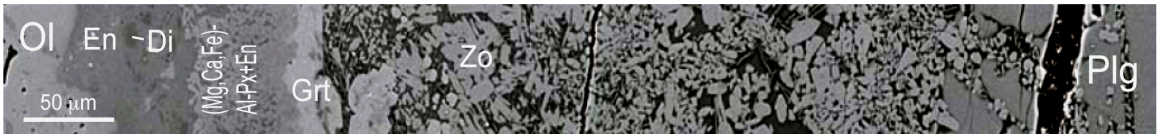

Fig.3: Experimentally (900°C, 1.8 GPa) produced reaction rim between olivine and plagioclase. A natural gabbro was used as starting material. Between the reactant phases olivine (Ol) and plagioclase (Plg) the layer sequence "enstatite (En) | diopside (Di) | pyroxene (Px) | garnet (Grt) | partially molten domain with zoisite (Zo)" is observed.

A complex multilayered reaction rim developed between a former olivine-plagioclase contact showing the rim sequence olivine | enstatite | diopside | pyroxene |garnet | partially molten domain with zoisite. Another example for complex olivine corona textures is given by Markl et al. (1998), which was found in samples from Lofoten, Norway. They observed the succession olivine | orthopyroxene + magnetite | orthopyroxene + garnet | plagioclase respectively olivine | orthopyroxene + magnetite | amphibole | K-feldspar with olivine being originally in contact with plagioclase respectively K-feldspar.

Effective bulk diffusion coefficients or at least relative diffusivities have been extracted from a variety of reaction bands and corona structures in natural rocks by applying non-equilibrium thermodynamic models. (e.g. Fisher 1973; Frantz and Mao 1976; Joesten

1977; 1991a, 1991b, Fisher 1978; Joesten and Fisher 1988; Johnson and Carlson 1990; Ashworth and Birdi 1990; Ashworth and Sheplev 1997; Ashworth et al. 1998; Markl et al. 1998; Abart et al. 2001; Carlson 2002; and references therein). All these models reproduce modal amounts of product minerals and the sequential arrangements of layers in coronal reaction zones only, if appropriate relative rates of diffusion for components participating at the reaction are assumed. Keller et al. (2006, 2007 and 2008) as well as Prenzel et al. (2008) developed models in which they address the relative contributions of volume and grain boundary diffusion in natural corona structures. Consequently, models that explain reaction rim growth in nature are able to give reasonable but no definitive solutions concerning the diffusion pathways and the mobility of all components in every individual layer of a complex rim sequence.

Several parameters may affect the growth rate, microstructure and layer sequence of a reaction rim such as the chemical composition of starting materials, pressure and temperature conditions during metamorphism, reaction time, availability of fluids or the oxygen fugacity. This has the advantage that a reaction rim records detailed information about the metamorphic history of a sample. However, as a naturally grown complex reaction rim was affected by a variety of processes, the exact determination of a single parameter is posing a challenge. Laboratory experiments are the method of choice for performing rim growth experiments under controlled conditions in relatively simple chemical systems and allow the determination of definite component diffusivities. They also allow describing the effect of a single parameter on component diffusivities. By getting stepwise more complex, they will allow us to get a better understanding of the growth of natural coronas and therefore the metamorphic history of rocks.

3.2. Rim growth in laboratory experiments

3.2.1. Binary systems

So far, temperature-time-dependent experimental growth of polycrystalline reaction rims has been mainly focused on simple binary model systems such as the system MgO-Al_2O_3, where reaction rims of spinel ($MgAl_2O_4$) were grown between periclase (MgO) and corundum (Al_2O_3) (Rossi and Fulrath 1962; Whitney and Stubican 1971; Watson and Price 2001; Götze et al. 2009). A reaction in the binary system MgO-SiO_2, which is shown in Figure 4, where an enstatite rim grows between forsterite and quartz has been investigated repeatedly (Thompson 1959; Yund 1997; Fisler et al. 1997; Milke et al. 2001; Abart et al. 2004, 2009; Milke et al. 2007, 2009 a, 2009 b, Gardés et al. 2011)

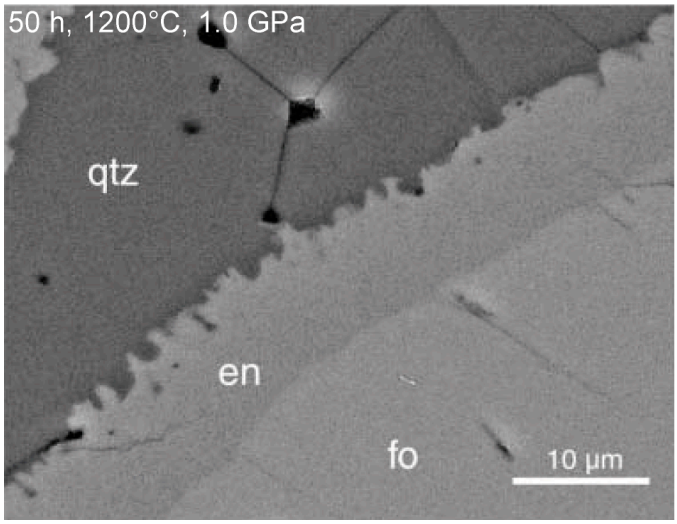

Fig.4: Backscattered electron image of a polycrystalline enstatite reaction rim, growing between seeds of San Carlos Olivine ($fo_{92}fa_8$) and a quartz matrix. The experiment was performed in a conventional piston cylinder apparatus at 1200°C, 1.0 GPa for 50 h (Milke et al. 2001).

The results have been interpreted in terms of MgO as rate controlling component, temperature-dependent effective MgO diffusivities inside the rim, influence of the matrix rheology, the effect of the FeO-component in MgO-rich olivine and the effect of small amounts of water.

Gardés et al (2011) showed that not only enstatite (en) single rim growth between forsterite and quartz but also forsterite (fo)-enstatite double-rim growth between periclase (per) and quartz (qtz) is largely controlled by MgO-diffusion at very dry conditions, whereas SiO_2 remains relatively immobile.

Also well understood is the growth of monomineralic single layered rims in the ternary system $CaO\text{-}SiO_2\text{-}CO_2$, where calcite ($CaCO_3$) and quartz ($SiO_2$) react to wollastonite ($CaSiO_3$) and CO_2 (Milke and Heinrich, 2002).

3.2.2. Diffusion pathways

Three main kinetic regimes exist according to Harrison (1961) in a polycrystal, which describe the transport pathways of components through a rim.

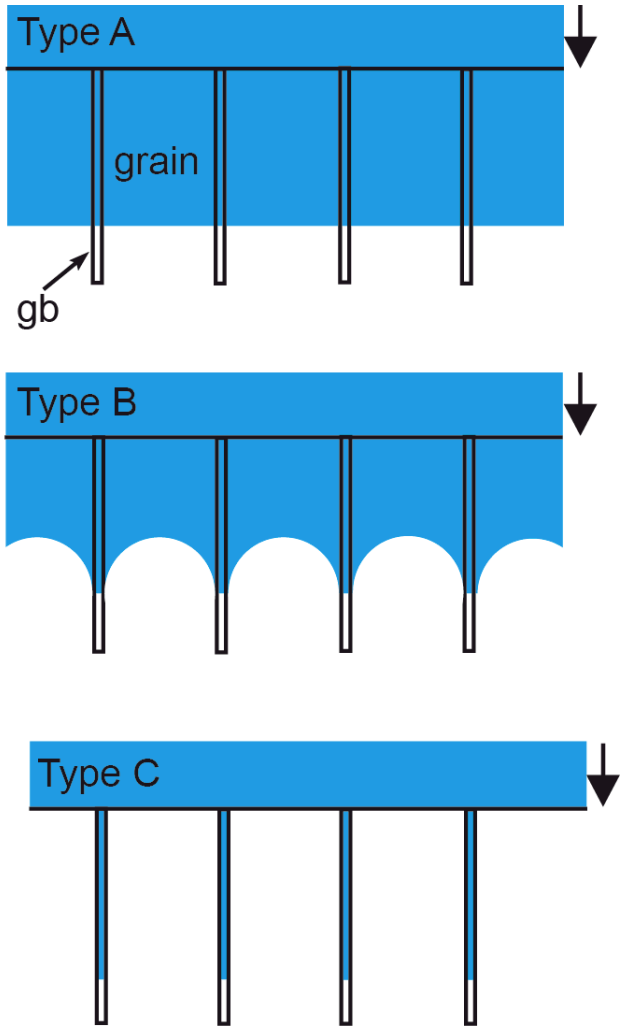

Fig.5: Three kinetic regimes describing diffusion pathways in a polycrystal according to Harrison (1961). Arrows are indicating direction of flow from the source of diffusing components. For further explanations see text.

In kinetic regime C, the diffusive flow in a polycrystal propagates mainly along the grain boundaries and diffusion in the volume is insignificant. In contrast to that, grain boundary und volume diffusion are almost identical in kinetic regime A. In this regime, it may also appear that the diffusion path in the volume is considerably longer than the distance between adjacent grain boundaries so that the fields of volume diffusion overlap each other. In accordance with regime A, diffusion in kinetic regime B takes place at the boundaries and in the volume of the grains but in contrast to regime A, grain boundary diffusion is significantly faster than volume diffusion and diffusion flows from adjacent grain boundaries do not overlap. A diffusive flux of the growth rate controlling

component is from now on described as effective diffusivity, if the kinetic regime i.e. the pathway of diffusion is not specified.

The growth of a reaction rim may be interface controlled or transport controlled. If the reaction is interface controlled, growth of layers in a reaction rim should be direct proportional to the reaction time (e.g. Kirkaldy and Young 1987). If rim growth is parabolic, i.e. the rims grow with the square root of time, reaction rim growth is diffusion controlled. This is what was observed in many experimental studies in the system MgO-SiO_2 (Fisler et. al. 1997; Yund 1997; Milke et al. 2001, 2007, 2009a, 2009b). However, Gardés, et al. (2011) have demonstrated that diffusion controlled rim growth may show deviations from parabolic behavior.

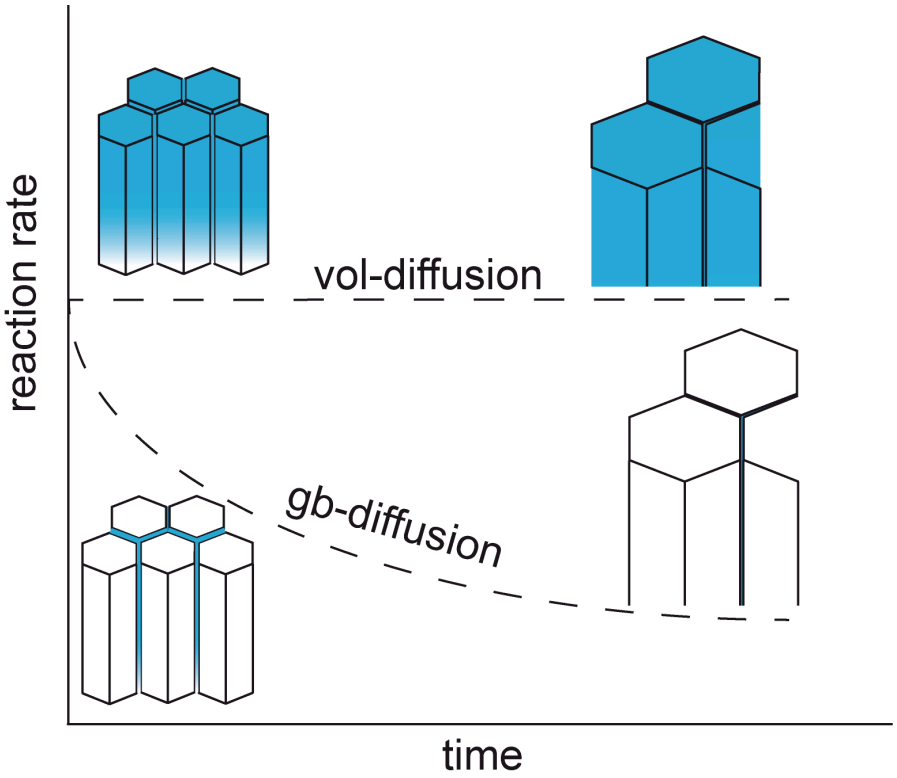

Fig.6: Temporal evolution of the reaction rate. It is assumed that the grains of a polycrystalline reaction rim are coarsening as reaction proceeds. The reaction rate remains constant, if rim growth is volume diffusion controlled and is decreasing, if rim growth is grain boundary diffusion controlled.

Figure 6 shows schematically the grains of a polycrystalline reaction rim. It is assumed that these grains are growing as reaction proceeds. This results in a successive decrease of the grain boundary density. If rates of volume diffusion are comparable to those of grain boundary diffusion (kinetic regime type A), the bulk diffusivity is independent of grain coarsening and remains constant as reaction proceeds. If grain boundaries are fast pathways for diffusion (kinetic regime type B or C), they contribute significantly to the bulk mass transfer. In this case, the decreasing grain boundary density results in

decreasing bulk diffusivity, so that rim growth rates do not follow a parabolic rate law (Gardés et al. 2011). Therefore, the temporal evolution of the reaction rates provides information whether rim growth is mainly controlled by interface processes, grain boundary or volume diffusion.

3.3. Effect of water

Several studies showed that the presence of small amounts of water has a significant effect on rim growth reaction rates. Carlson (2010) showed that rates of intergranular diffusion of Al in garnets at a constant temperature as well as corresponding length- and timescales of metamorphic reactions may vary by as much as seven orders of magnitude across the range of H_2O activities found in nature. Concerning laboratory experiments, several studies have shown that the introduction of small amounts of water to a dry experiment may have a significant effect on rim growth rates in the binary system MgO-SiO_2 (e.g. Yund 1997). Milke et al. (2009b) demonstrated that the mobility of MgO in very dry orthopyroxene rims growing between forsterite and quartz at 1000°C is about 4 orders of magnitude lower compared to the mobility in similar experiments, in which small amounts of water were present (Fig. 7).

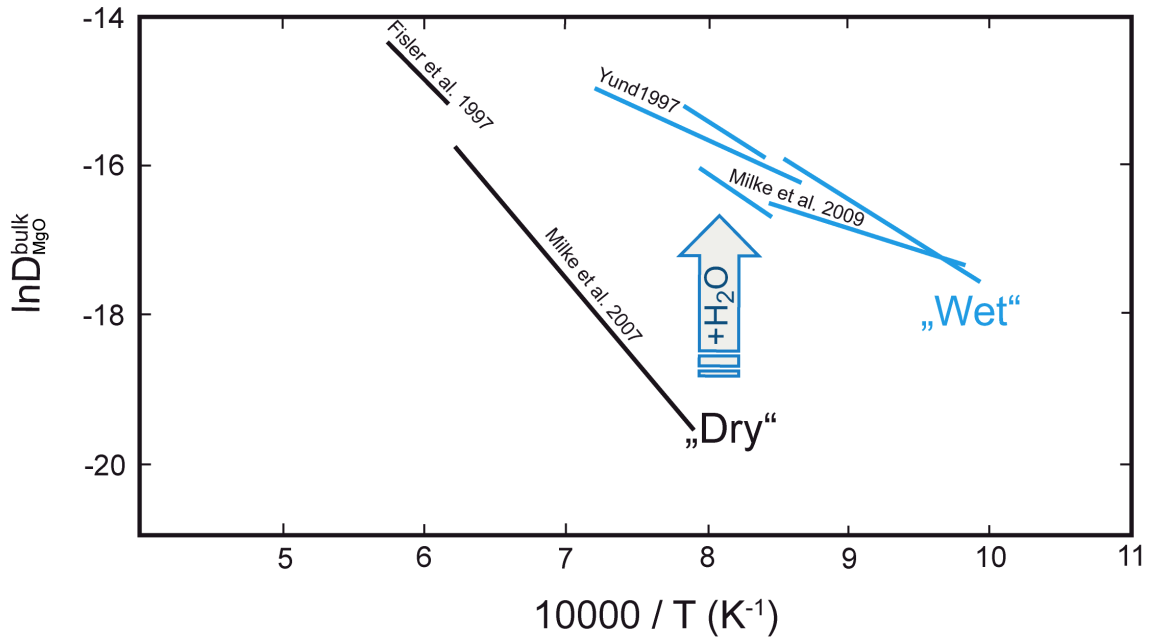

Fig.7: Arrhenius diagram, showing the comparison of different experimental rim growth studies, in which an enstatite reaction rim grows between forsterite and quartz (modified after Milke et al. 2009b). Very dry experiments performed in 1-atm-furnaces (Fisler et al. 1997; Milke et al. 2007) are orders of magnitude slower than humid experiments, in which small amounts of water ranging from several ppm (Milke et al. 2009b) up to 0.1 wt% (Yund 1997) were added. Significant differences in bulk diffusivities are interpreted as an effect of the availability or absence of minute amounts of water during rim growth.

Water may be directly introduced in rim growth experiments as molecular H_2O (Yund 1997; 0.1 wt%), by adsorption on the surface of even pre-dried starting materials (Milke et al. 2009b; about 7-20 ppm), which is of particularly significance, if small-grained powders are used. Other possibilities are given by fluid inclusions or OH-defects that are present in natural starting materials (Milke et al. 2009b; 60 ppm) or in the case of piston cylinder experiments by diffusion of fluids initially located in the pressure medium through the noble metal capsule into the charge (Truckenbrodt and Johannes 1999). Remarkably, the introduction of different amounts of water ranging from several ppm up to 0.1 wt% has no significant effect on the reaction rates (Fig. 7). It seems that especially the introduction of minute amounts of water to a formerly dry system significantly affects rim growth kinetics.

In addition to that water may change the relative component mobilities of the growth rate controlling component(s) in different layers of a rim sequence. The ternary diagram at 0.5 GPa and 1200°C (Fig. 8b) shows that a reaction of periclase and quartz will produce a double layered rim with the sequence periclase | forsterite | enstatite | quartz. An effect of minute amounts of water on relative component mobilities in forsterite respectively enstatite may be visible in variations of the thickness ratio of the layers in this reaction rim. In the CMS-system, the reaction of periclase and wollastonite was performed at 1200°C and 0.5 GPa. The simplest possible rim sequence that may develop is periclase | monticellite | åkermanite | wollastonite, if local equilibrium is expected. This is only possible if the CaO/SiO_2-ratio remains constant throughout the overall rim sequence. An effect of water on the relative component mobilities may have an effect on this ratio and consequently on the layer sequence.

3.4. Goals of this study

The overall goal of this study is to gain a better understanding of the metamorphic history of a natural sample. Metamorphic reaction rims suit perfectly for this goal. They are recorded in many metamorphic rocks; they may be described by a reaction, which involves time as one of the controlling parameters and they are affected by many different parameters such as temperature, pressure or the presence of fluids (3.1.). However, this complicates the gain of the overall goal because growth of a complex natural reaction rim is the result of a combination of effects of all these parameters. Laboratory experiments are the method of choice to perform rim growth experiments under controlled conditions. So far, rim growth experiments were only produced in

relatively simple binary systems, whereby especially the growth of a monomineralic, polycrystalline enstatite (en) single rim between forsterite (fo) and quartz (qtz) in the binary system (MgO-SiO_2) is quite well understood (3.4.). In this study, we want to get closer to the understanding of the processes that control formation of natural reaction rims by performing more complex laboratory experiments. For this reason, the binary MgO-SiO_2 (MS) -system is extended to a ternary system by using CaO as a third component (CMS-system). Figure 8 displays the configuration of the stable phases in a ternary diagram at 0.5 GPa and 1200°C and the phase relations in a P-T-projection.

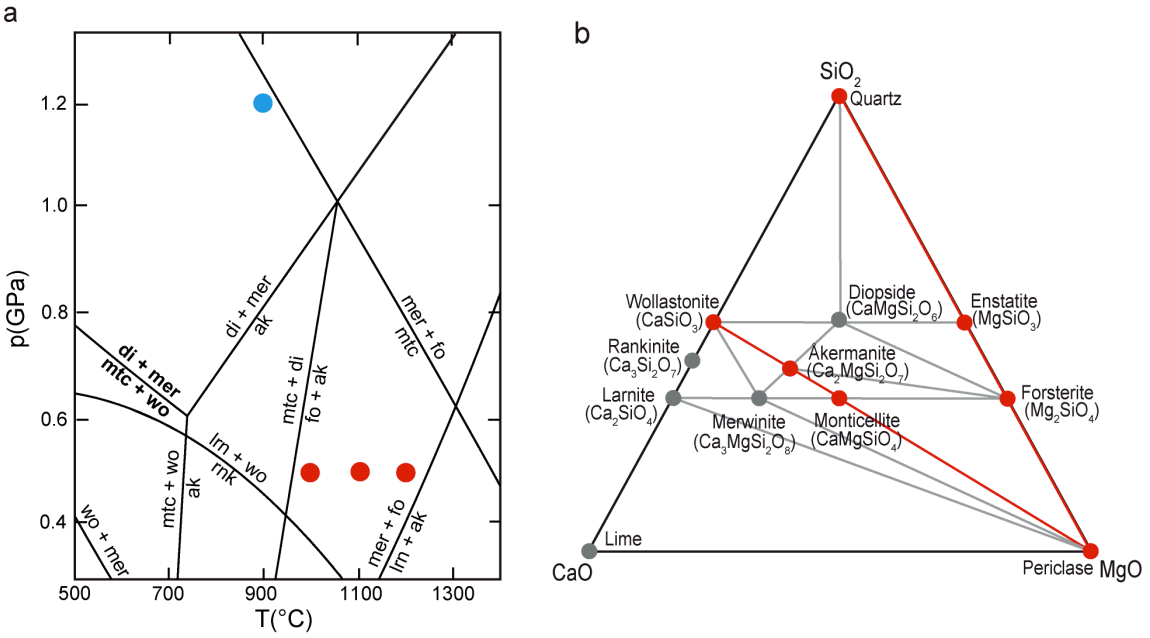

Fig.8: Phase relations of relevant phases in the ternary system MgO-CaO-SiO_2. **a:** P-T projection; blue circle indicates the experimental conditions applied for the reaction monticellite + wollastonite => diopside + merwinite, red circles indicate the experimental conditions for the reactions: Monticellite + wollastonite => åkermanite, periclase + wollastonite => monticellite + åkermanite and periclase + quartz => forsterite + enstatite. **b:** Ternary diagram showing the stable phase relations at 1000 to 1200°C and 0.5 GPa. Red lines represent the reactions described above. Note that reactants and educts are always collinear. This is only possible, if the CaO/SiO_2 ratio remains constant all over the rim. This must not necessarily be the case (*see chapter 7.2.2.2.*). Data from Holland and Powell (1998). Mineral abbreviations after Kretz (1983) with the addition of "mer" for merwinite.

The first part of this study will focus on the reaction:

monticellite ($CaMgSiO_4$) + wollastonite ($CaSiO_3$) = åkermanite ($Ca_2MgSi_2O_7$) (2)

at 1000-1200°C, 0.5 GPa and durations between 5 min and 60 h. Following questions will be answered:

- What is (are) the growth rate controlling component(s)?
- What are the diffusion constants?
- What are the diffusion pathways of the growth rate controlling component(s)?
- What is the effect of small amounts of water on the overall growth rate?

In ternary systems, it is possible that reaction rim with a bimineralic layer develops, even if local equilibrium at the reaction interfaces is assumed. At 900°C and 1.2 GPa a reaction rim forms comprising two phases, merwinite (mer) and diopside (di), growing at wollastonite (wo)-monticellite (mtc) contacts (Fig. 8a). This is represented by crossing tie lines in the ternary diagram (Fig. 9).

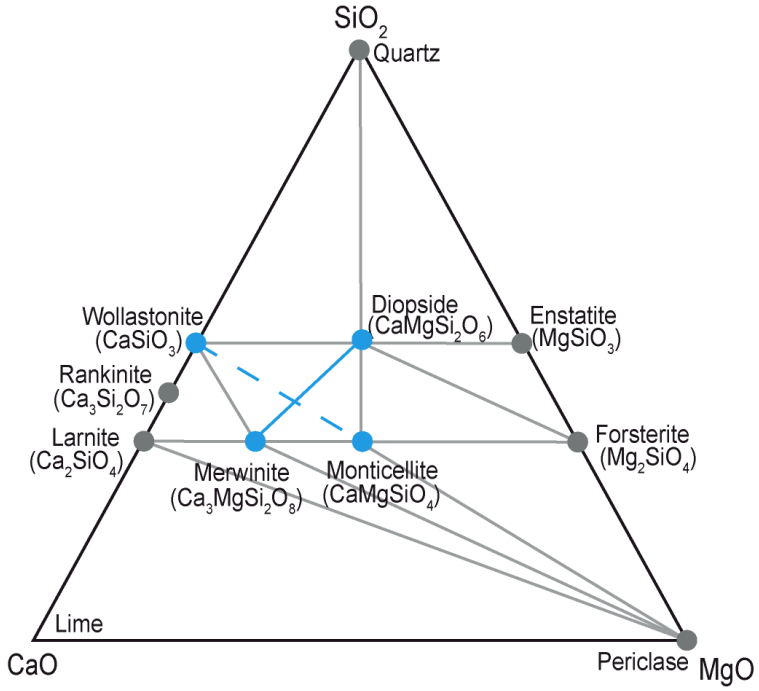

Fig.9: Configuration of stable phase relations at 900°C and 1.2 GPa. Rim growth reaction is represented by crossing tie lines between unstable monticellite + wollastonite and stable diopside + merwinite assemblages. Calculations are based on the thermodynamic data of Holland and Powell (1998).

A reaction that is represented by crossing tie lines in a ternary diagram implies that the reaction product is potentially a bimineralic reaction rim. According to that, the second part will answer the questions:

- How does a bimineralic reaction rim grow in the ternary system CaO-MgO-SiO_2?
- What are the effects of the presence of small amounts of water on relative component mobilities and the microstructure of bimineralic reaction rims?

It seems obvious that water, even in minute amounts, has a significant effect on rim growth rates (3.4.). However, the addition of very small controlled amounts of water to a rim growth experiment turns out to be an experimental challenge. A possible solution is the use of water-doped nominally anhydrous minerals as starting materials. In this study, defined minute amounts of water will be introduced in rim growth experiments in form of OH-defect in periclase. During rim growth, periclase will be consumed so that water will be released. After the release, water may be present as a separate phase. Other

possibilities are that it may dissolve in the product phases, be stored in the newly produced grain boundaries of the polycrystalline reaction rim or create new OH-defects in the starting materials. It is important to know how water is exactly present during rim growth reactions in order to understand its effect on nucleation and growth of reaction rims. The third part of this study will answer the questions:

- Are we able to introduce very small controlled amounts of water in reaction rim growth experiments by using OH-doped periclase as starting material?
- What is the effect of these small amounts of water on rim growth rates, rim sequences and the relative component mobilities in multilayered rim growth experiments in the binary system $MgO\text{-}SiO_2$ and in the ternary $CaO\text{-}MgO\text{-}SiO_2$ system?
- Where is the water located after the experiment?

4. Experimental Methods

4.1. Experiments

4.1.1. Sample preparation

Rim growth reactions were performed between monticellite and wollastonite, periclase and wollastonite as well as periclase and quartz. Synthetic optical periclase was provided by CRYSTEC (Berlin), synthetic monticellite and wollastonite by the Institut für Kristallzüchtung (IKZ, Berlin-Adlershof) and natural wollastonite from Ciclova-Romina (Banat, Romania) was granted by the Museum of Natural Science (Berlin). Both starting materials have within the accuracy of the microprobe analysis an ideal composition of $Ca_{1.0}Si_{1.0}O_3$ and $Mg_{1.0}O_1$, whereas the synthetic monticellite deviates from endmember composition and has some forsterite component; EMP analysis gave $Ca_{0.89}Mg_{1.11}Si_{1.00}O_4$ (Table 1).

Table 1: Composition of starting materials. Values based on 30 point analysis using a JEOL FEG-EMP instrument.

	Wo natural (start)	**Wo synthetic (start)**	**Periclase (start)**	**Mtc (start)**
CaO	48.50(11)	48.55(10)	0.06	32.28(23)
MgO	0.14(01)	0.02(01)	100.01	28.76(21)
SiO_2	51.61(08)	51.67(07)	0.05	38.82(13)
Total	100.25	100.24	100.12	99.86
No. of cations based on	3 O	3 O	1 O	4 O
Ca	1.00	1.00	0.00	0.89
Mg	0.00	0.00	1.00	1.11
Si	1.00	1.00	0.00	1.00

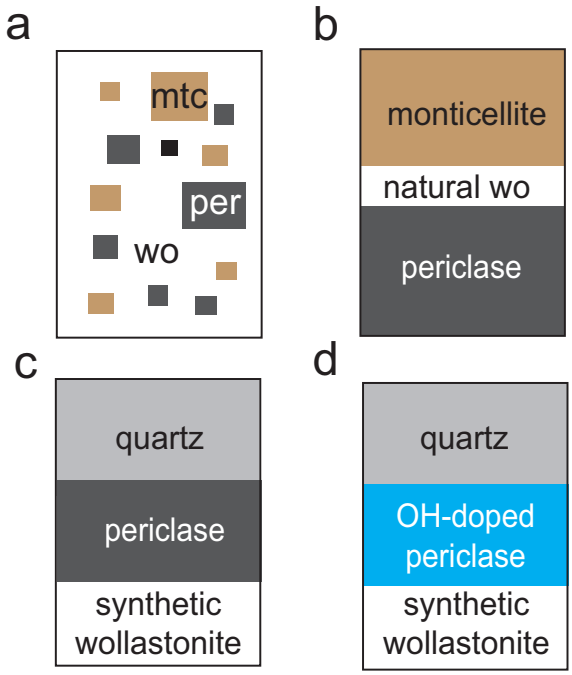

Fig.10: Schematic setup for rim growth experiments. A platinum capsule surrounds all setups. **a**: Monticellite and periclase crystal fragments (100-200 μm) embedded in wollastonite powder **b:** Setup consisting of a sandwich of monticellite | natural wollastonite | periclase. **c:** Setup consisting of a sandwich of quartz | dry periclase | synthetic wollastonite. **d:** Setup consisting of a sandwich of quartz | OH-doped periclase | synthetic wollastonite.

Experiments were performed in four different setups, which are schematically displayed in Figure 10. Setup **a** (mtc and per seeds in wo-matrix) consisted of grain fragments of periclase and monticellite (100-200 μm in size) embedded in a fine-grained matrix (≤ 20 μm) composed of natural wollastonite. Starting materials (periclase, monticellite and natural wollastonite) were crushed and dried at 800°C for 1 h. Grain size fractions were obtained by wet sieving and subsequent drying at 110°C for 30 min. Mixtures consisting of 10 vol% periclase, 10 vol% monticellite (both with a grain size of 100-200 μm) and 80 vol% wollastonite (grain size ≤ 20 μm) were prepared. Starting materials were subsequently transferred into a platinum capsule with 3.0 mm inner diameter, 3.2 mm outer diameter and 1 cm length, which was immediately sealed shut using a plasma-welder.

Setup **b** (per | natural wo | mtc) consisted of a sandwich of periclase | natural wollastonite | monticellite single crystals and setup **c** (synthetic wo | per | qtz) of a sandwich of synthetic wollastonite | dry synthetic periclase | quartz. For these setups cylindrically shaped chips (2.8 mm in diameter, 0.5-3 mm thick) were drilled from the starting

materials and dried at 800°C for 1h. The contact surfaces of all prepared chips were carefully polished, cleaned with acetone, ethanol and water and dried at 110°C for 30 min. Crystal cylinders were put into a platinum capsule with 3.0 mm inner and 3.2 mm outer diameter, which was cold-sealed immediately. In one sandwich experiment (IHPV 10, Table 2), both wollastonite surfaces were initially sputtered with platinum for a few seconds so that dispersed platinum particles were deposited on the surface. These particles act as inert markers to trace the original interface between starting materials.

Setup **d** (synthetic wo │OH-doped per│qtz) consisted of a sandwich of synthetic wollastonite | OH-doped periclase | quartz. Preparation of OH-doped periclase used for this setup is described in the following chapter. OH-doped periclase has not been dried at 800°C to avoid water loss, all other preparation steps are similar to the ones of setups **b** and **c** described above.

4.1.2. OH-doping of periclase starting materials

The use of OH-doped periclase as starting material may provide a method to introduce very small controlled amounts of water in rim growth experiments. Results of these experiments are shown and discussed in chapter 7. During consumption of the OH-doped reactant, water is released. Cylindrical (2.8 mm diameter), dry, synthetic single crystals of periclase were sealed in a platinum capsule with excess amounts of pure H_2O. Water doping experiments were performed in a vertical Harwood type Internally Heated Pressure Vessel (IHPV) at 0.5 GPa and 1200°C for 20 h. Type R thermocouples were used for temperature control. The pressure medium was argon. After the doping-experiment, a thin layer of brucite powder was observed on the surface of the periclase single crystals. This was removed by polishing the crystals on both flat surfaces. Polished periclase single crystals were cleaned in acetone and ethanol and dried at 110°C for 15 min. The dried cylinders were analyzed via IR-spectroscopy and transmission electron microscopy. Afterwards, the outer rim of the periclase cylinder was removed by polishing so that the overall diameter was reduced to about 2.5 mm. The downsized crystal cylinder was cleaned in acetone, ethanol and water and dried at 110°C for 15 min. As starting material for rim growth experiments, a periclase is needed that shows a homogenous distribution of OH-defects in the whole crystal. This was made sure via IR-spectroscopy (*see chapter 7.2.2.1.*).

4.1.3. Internally Heated Pressure Vessel (IHPV)

The Internally Heated Pressure Vessel (IHPV) was used for experiments between monticellite and wollastonite at 1000-1200°C and 0.5 GPa, which are presented in chapter 5, and in experiments using OH-doped periclase as starting material (chapter 7) Experiments were performed at o.5 GPa in a vertical Harwood type IHPV. Pressure was controlled automatically and argon was used as dry pressure medium. Temperature conditions were between 1000-1200°C. Type R thermocouples were used for temperature control. Run durations were between 5 min and 60 h. All experiments that used cold-sealed capsules (setup **b**, per⎪natural wo ⎪mtc; setup **c**, synthetic wo ⎪per ⎪qtz; setup **d**, synthetic wo ⎪OH-doped per⎪qtz), were put into a second outer platinum capsule of 4.0 mm inner and 4.4 mm outer diameter and immediately sealed shut using a plasma-welder. This is necessary to keep the water availability constant during IHPV-experiments, which would not be the case in cold-sealed capsules that are permeable for water molecules. Because reaction kinetics are strongly temperature dependent, construction of a new sample holder was required that minimizes the temperature gradient along the sample (Fig. 11).

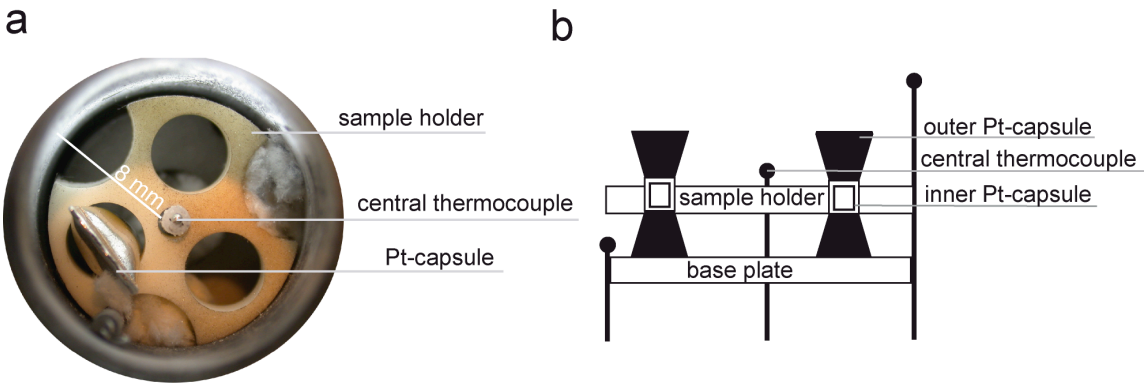

Fig.11: a: Image of a newly developed sample holder that minimizes temperature gradients in the IHPV. **b:** Side view of the sample holder illustrating the position of the samples and the thermocouples, which record the horizontal and vertical temperature distribution. For further explanation see text.

The sample holder consists of corundum. Three thermocouples are fixed in the center and at either side of the sample chamber. The tips of these thermocouples are located at different heights. The two outer thermocouples control the temperature of the respective furnace zone independently. In combination with the central thermocouple, the temperature distribution may be controlled vertically and horizontally. The sample holder has three round holes that carry the capsule (Fig. 11a). After insertion, the capsules are fixed by flattening both ends with pliers and sealed shut using a plasma-welder. Semicircle-shaped holes at the rim of the sample holder provide additional empty space and allow for convective gas flow in the sample chamber. A further advantage of the

device is that spaces between the three thermocouples and the capsules remain constant throughout the course of the experiment, so that a potential temperature gradient in the sample chamber could be monitored by using the three thermocouples and extrapolated for the exact sample position. However, this is not necessary as the maximum temperature difference between the three thermocouples at 0.5 GPa and 1000-1200°C was 4-10°C, which is small enough to allow for determination of a temperature dependence of the reaction rates. Run durations were corrected in order to include the additional diffusion occurring during heating ramps (Lasaga 1983)

$$t' = \int_0^t \exp\left\{-\frac{E_a}{R}\left[\frac{1}{T_{(t)}} - \frac{1}{T_0}\right]\right\} dt \qquad (3)$$

with t' being the corrected run duration, E_a the activation energy, R the gas constant, T_0 the plateau temperature and T_t the temperature after time t during heating. The target temperature was reached via a heating rate of 30 K/min. According to Lasaga (1983), 0.04 h must be added to the effective run duration at a plateau temperature of 1200°C, which is only significant for very short experiments. Quenching was sufficiently rapid (< 1 min) even for very short run durations, so that correction is not necessary. After the runs, the capsules were embedded in epoxy and polished. It is important to note that sandwich experiments were polished perpendicular to the original interfaces. In chapter 7, the effect of water on rim growth is discussed. Therefore, dry and water-bearing samples (IHPV-d-1, IHPV-w-1 and IHPV-w-3; Table 2) were both-sided polished for IR-spectroscopic measurements, which is the method of choice to visualize OH-defects in crystalline materials.

4.1.4. Piston Cylinder

Experiments producing a bimineralic reaction rim consisting of merwinite and diopside, which grows between monticellite and wollastonite, as shown in chapter 6, were performed at a pressure of 1.2 GPa and 900°C in a conventional piston cylinder apparatus. In contrast to experiments performed in the Internally Heated Pressure Vessel, platinum capsules are permeable for traces of water in piston cylinder assemblies at the P-T-conditions of our experiments (Douce and Beard, 1994; Truckenbrodt and Johannes, 1999). For that reason, a pressure medium that contains fluid inclusions may directly effect the water availability during rim growth as traces of fluid stemming from this pressure medium may infiltrate into the platinum capsule during the course of the

experiment. In order to vary the water availability, three different assemblies were used that consist of either natural, fluid inclusion containing, calcium fluorite, or very dry, pure Al_2O_3 or a combination of both. For powder experiments (capsule setup a, mtc and per seeds in wo-matrix), natural calcium fluorite was used as pressure medium (Fig. 12-1, assembly 1, direct contact to fluid inclusion bearing CaF_2), which means that the capsule was in direct contact with fluid containing CaF_2 at the start of the experiment.

Two piston cylinder-experiments used pure, dry Al_2O_3 as pressure medium (Fig. 12-2, assembly 2, dry Al_2O_3). For these experiments capsule setup b (per | natural wo | mtc) was used. Finally a setup was used, in which a 3 mm thick inner layer of Al_2O_3 protected the Pt-capsule for a certain time from fluids stemming from the outer layer consisting of natural CaF_2 placed as an envelope around the dry Al_2O_3 (Fig. 12-3, assembly 3, Al_2O_3-protection layer + CaF_2). The capsule setup was identical to that used in assembly 2.

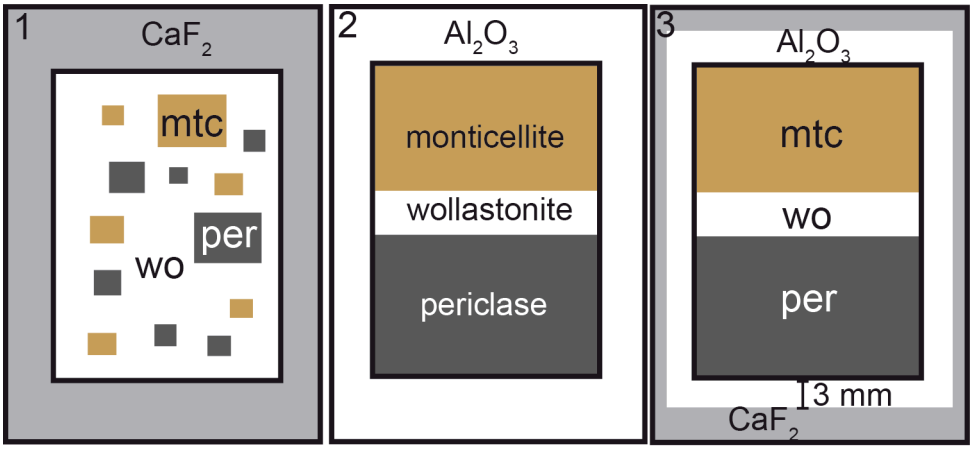

Fig.12: Schematic demonstration of experimental charges for piston cylinder experiments. **1:** Assembly only used for capsule setup **a** (mtc and per seeds in wo-matrix). The solid pressure medium is natural CaF_2 (assembly **1**, direct contact to fluid inclusion bearing CaF_2). **2:** Assembly only used for capsule setup **b** (per | natural wo | mtc). The solid pressure medium is Al_2O_3 powder (assembly **2**, dry Al_2O_3). **3:** Capsule setup identical as used in assembly 2**.** The pressure medium consists of a 3 mm thick inner layer of Al_2O_3 that is surrounded by an outer layer of natural CaF_2 (assembly 3, Al_2O_3-protection layer).

Run durations were between 5 and 65 h. Heating (> 50 K/min) and quenching (< 1 min) was sufficiently rapid compared to overall run duration so that correction is not necessary. Run products were embedded in epoxy and polished. The per | wo | mtc sandwiches were polished perpendicular to the original interfaces. Two samples, stemming from experiments performed in assembly 2 (P13, Table 5) and assembly 3 (P8, Table 5) were both-sided polished for IR-spectroscopic measurements.

4.2. Analytics

4.2.1. Electron Microprobe

All samples were examined with an electron microprobe using a JEOL JXA-8500F instrument equipped with a field emission gun. Rim thicknesses of all experiments were determined by using backscattered electron images. The rim thicknesses within each run were measured at 20-100 different locations and averaged. Average grain width was measured on BSE-images obtained with the same instrument. Here about 10-20 individual grains were measured for each sample. It is important to note that a 2D-section does not necessarily correspond to the actual grain size. Nevertheless the effect of grain growth may safely be shown by the usage of the measured grain width on BSE-images. Chemical compositions of starting materials and reaction products were obtained by wavelength dispersive EMP analysis. For analyzing starting materials before and after rim growth experiments, conditions were 15 kV and 20 nA; analyses of the layers in the reaction rim were performed at 6 kV and 10 nA, both with focused beam. Uncertainties are derived from the standard deviation of the single measurements. Well-known synthetic and natural standards were used for EMP-standardization.

4.2.2. Infrared Spectroscopy (IR)

Infrared spectroscopy is the method of choice to analyze the water distribution in reaction rim growth experiments and was therefore applied to selected starting materials and sandwich samples. IR-spectra were taken at room temperature in transmission mode using an FTIR-spectrometer IFS 66v manufactured by Bruker. The measurement range was 2000-5000 cm^{-1} and 256 scans per spectra were averaged with a resolution of 2 cm^{-1}. The aperture size was 20·100 μm, with the 100 μm long edge oriented parallel to the rim of the sample. A globar served as light source, a KBr beam splitter and an InSb detector were used. Measurements were performed in unpolarized light. Recorded spectra were fitted using the PeakFit software from Jandel Scientific.

Spots for IR-spectroscopic measurements of undoped and doped periclase starting materials before rim growth experiments were chosen in the center and close to the outer edge of the periclase cylinder (Fig. 13), to get information about the OH-defect distribution.

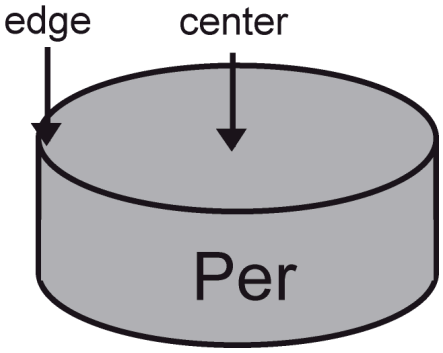

Fig.13: Position of spots (center and edge) for IR-spectroscopic measurements taken on dry and OH-doped periclase starting materials. Aperture size was 20·100 μm. Same positions were used for the extraction of an ion-thinned foil for TEM-measurements (*see chapter 4.2.4.*).

Periclase is the material of choice for performing IR-spectroscopic analyses after rim growth experiments, because it incorporates very small amounts of water (~2 ppm at 24 GPa and 1600°C, Bolfan-Casanova et al. 2000) that are clearly visible in IR-spectra as absorption bands that may be attributed to OH-defects (e.g. Freund and Wengeler 1982). Consequently, initially dry, synthetic, periclase starting material was analyzed after a piston cylinder experiment (P1, Table 5) and originally dry as well as OH-doped periclase starting materials were analyzed after IHPV-experiments (IHPV-d1, IHPV-w1, IHPV-w3, Table 7). The IR spot was taken as close as possible towards the reaction rim that grows between wollastonite and periclase.

In order to examine the effect of water on reaction rim growth, detailed information about the water distribution in a sample after water-bearing rim growth experiments are required. For that reason, a detailed map of the OH-defect distribution of an OH-doped periclase starting material after a rim growth experiment (IHPV-w1, Table 7) was generated. IR-mapping was performed at the University of Innsbruck (Faculty for Geo- and Atmospheric Sciences) by using a Bruker Vertex 70 FTIR spectrometer combined with a Hyperion 3000 microscope equipped with a single element MCT detector, a focal plane array (FPA) detector, a globar light source and a KBr beam splitter. By using an FPA-detector, the spatial resolution of the MIR-signal is only limited by the wavelength of the IR-radiation (e.g. 3.3 μm at 3000 cm^{-1}, Prechtel and Stalder, 2009). Measurements were performed in unpolarized light in transmission mode. Spectra were taken in the 3000 to 4000 cm^{-1} range, which is the characteristic interval for vibrations of hydrous species, whereby 64 scans were averaged for each single spectrum. Data reduction was performed by recognizing absorption bands that can safely be attributed to OH-defects in

the crystal structure, defining the left and right margin of these bands, subtracting a linear background in between these points and calculating the area of the absorption band. The values were color-coded which allows to graphically display them as a map that shows the OH-defect distribution in the analyzed area of the sample.

4.2.3. Transmission Electron Microscopy (TEM)

For images that require extremely high spatial resolution below the μm-scale, transmission electron microscopy was used. Ion thinned-foils were cut using a focused ion beam instrument FEI FIB200TEM (Wirth 2004). An ion-thinned foil was cut out of the edge and the center of a well-polished OH-doped periclase cylinder starting material (Fig. 13) to examine whether OH-doping has an effect on the periclase microstructure. Another ion-thinned foil was cut across the expected reaction zone located at the interface between monticellite and wollastonite after a rim growth experiment that was performed in the piston cylinder apparatus at very dry conditions (sample P13, Table 3; setup b, per │ natural wo │ mtc; assembly 2, dry Al_2O_3). The investigation of the foils was performed using a transmission electron microscope (TEM) FEI Tecnai G2 F20 X-Twin. Results are displayed as bright-field images in transmission mode. Chemical composition of specific areas of interest were analyzed using energy dispersive X-ray spectroscopy

4.2.4. Raman spectroscopy

Infrared spectroscopy only allows for quantification of the OH-content in silicates, if the absorption coefficient is well known. This is not the case for periclase. A rough estimation of the absorption coefficient was made by using the calibration of Libowitzky and Rossman (1997, *see chapter 7.2.1.1.*). In order to check the accuracy of this calibration, Raman spectroscopy was used as a second method to determine the water content in OH-doped periclase starting materials. Raman spectra were obtained on polished OH-doped periclase cylinders using a LabRam HR800 UV-VIS spectrometer with a focal length of 800 mm and a 1800 grooves/mm grating. This confocal, notch-filter based system is equipped with a motorized XY-stage, an Olympus optical microscope (100× long working distance objective, numerical aperture 0.80) as well as a Peltier-cooled CCD detector. During all measurements a confocal pinhole of 100 μm was used. Sample excitation was done using the 488 nm (blue) line of a coherent Ar^+ Laser Model Innova 70-3, operated at 300 mW, which gives a spotsize of about 1.4 μm. As periclase is a cubic mineral, initial and scattered laser light was unpolarized to increase

the signal. The focal point of the laser beam was adjusted approximately 5 μm beneath the polished sample surface in order to reduce artifacts due to surface effects. Raman spectra were obtained in multi window acquisition mode provided by the Labspec Software package in the frequency range of 2800 to 4000 cm^{-1}, representing the spectral interval, characteristic for vibrations of hydrous species. Acquisition time was 2000 s. Recorded spectra were fitted using the PeakFit software from Jandel Scientific. A glass standard with a known H_2O-content of 332 ppm was used as a reference and measured before and after the sample measurements at identical conditions except acquisition time, which was set to 500 s.

Chapter 5

This chapter is modified according to the publication:

"Experimental growth of åkermanite reaction rims between wollastonite and monticellite: evidence for volume diffusion control" (Contributions to Mineralogy and Petrology 161:389-399, 2011)

by

Bastian Joachim, Emmanuel Gardés, Rainer Abart, Wilhelm Heinrich

5.1. Results

All experiments described in this chapter were performed in the Internally Heated Pressure Vessel. A summary of performed experiments and experimental results is given in Table 2.

Table 2: Run conditions and results of IHPV-experiments. Used capsule setups (a, mtc and per seeds in wo-matrix; b, per │ natural wo │ mtc) are shown in Fig. 10. All experiments were performed at 0.5 GPa dry argon pressure. Effective run durations, which integrate diffusion during heating were calculated according to Lasaga (1983). Mean values for average rim thickness and grain width are based on 20-100 single measurements. Uncertainties for average rim thickness, average grain width and the effective bulk diffusion coefficient are given in terms of 1 σ.

No. of Experiment	Capsule setup	Temperature (°C)	Effective run duration (h)	Rim thickness (μm)	Grain width (μm)	log D (m^2/s)
IHPV 2	b	1200	33.71	10.6 (13)	3.8 (09)	-15.8 (08)
IHPV 5	b	1200	48.04	14.4 (35)	4.8 (06)	-15.7 (09)
IHPV 9	b	1200	40.04	13.7 (11)	4.7 (25)	-15.6 (08)
IHPV 10	b	1200	10.04	5.3 (04)	1.7 (05)	-15.9 (07)
IHPV 11	b	1200	60.04	16.3 (14)	5.4 (20)	-15.6 (08)
IHPV 15	b	1200	2.04	2.3 (04)	0.9 (03)	-16.0 (09)
IHPV 16	b	1200	0.54	1.3 (02)	0.6 (02)	-15.8 (09)
IHPV 17	b	1200	0.12	0.4 (01)	0.4 (01)	-16.0 (10)
IHPV 12	b	1100	20.03	4.5 (09)	3.6 (07)	-16.2 (09)
IHPV 14	b	1000	12.02	1.5 (03)	n.a.	-17.0 (09)
IHPV 3	a	1200	33.71	57.3 (94)	n.a.	-14.3 (08)

All experiments produced a monomineralic rim of åkermanite along the interface between monticellite and wollastonite according to the overall reaction mtc + wo ⇒ ak (eq. 1) confirming the stability of åkermanite relative to the assemblage monticellite + wollastonite at the experimental conditions of 1000°C to 1200°C at 0.5 GPa (Fig. 8a,b). Educts composition has not changed during rim growth experiments and no compositional variation was detected across åkermanite reaction rims within error limits (Table 3).

Table 3: Composition of run products and starting materials after rim growth experiments. Values represent averages based on 5 to 20 point analyses using a JEOL FEG-EMP instrument. Composition of starting materials is reported in Table 1. Uncertainties are given in terms of 1 σ.

	wo (final)	mtc (final)	ak
CaO	46.71 (58)	32.28 (23)	40.38 (34)
MgO	0.49 (07)	28.76 (21)	13.93 (28)
SiO_2	52.25 (83)	38.82 (13)	41.74 (26)
Total	99.45	99.86	96.05
No. of cations based on	3 O	4 O	7 O
Ca	0.98	0.89	2.03
Mg	0.01	1.11	0.99
Si	1.01	1.00	1.98

Åkermanite analysis gives only a total of 96.05 %. This is explained by the fact that the analyzed sample volume was very small due to the analyzing conditions of 6 kV and 10 nA. Results of the analysis may be affected by neighbored phases and surface roughness of the sample. Åkermanite only formed along the monticellite and wollastonite interfaces. A time series of eight sandwich experiments done at 1200°C with run durations ranging from 5 min to 60 h yields reaction rims with widths ranging between 0.4 and 16.3 μm.

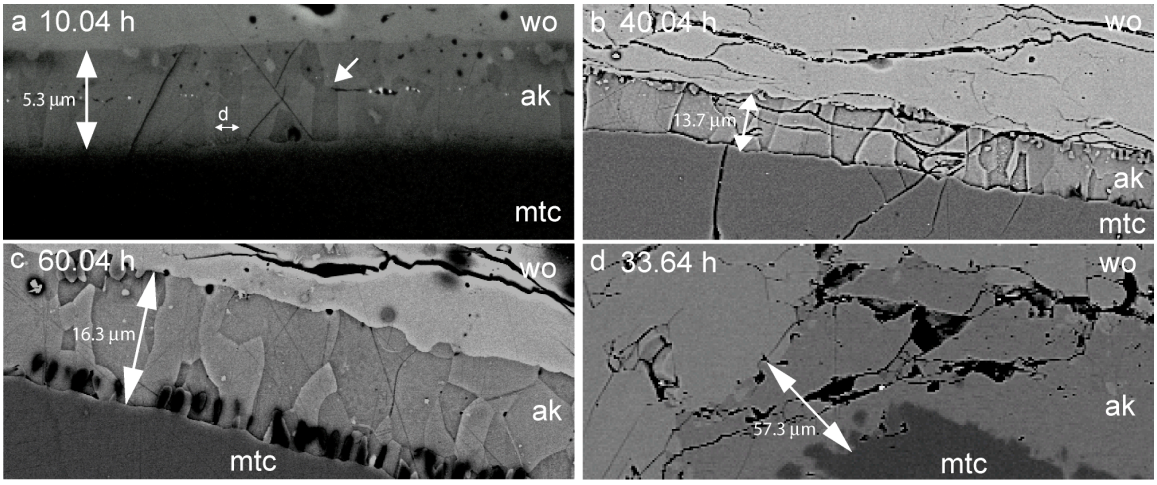

Fig.14: Backscattered electron micrographs of åkermanite (ak) rims produced between monticellite (mtc) and wollastonite (wo) at 1200°C, 0.5 GPa at different run durations (Table 1). **a-c:** sandwich experiments (setup b, per | natural wo | mtc). **d:** powder experiment (setup a, mtc and per seeds in wo-matrix). **a:** Run No. IHPV10, after 10.04 h effective run duration. Bright spots in the center of the åkermanite reaction rim are platinum markers placed at the original mtc-wo interface. Ak grains display a palisade texture oriented normal to the original interface. At places, it is evident that palisade growth occurred from the original interface into both directions (*arrow*). *D* denotes the grain width measured normal to the palisade elongation. **b:** Run No. IHPV 9, after 40.04 h. Palisade-shaped åkermanite single grains extend across the entire rim. **c:** Run No. IHPV 11, after 60.04 h. Palisades start to break down resulting in (partly) randomly oriented grain boundaries. Black dots at the lower part of the rim are artifacts due to sample preparation. **d:** Run No. IHPV 3 after 33.64 h. The åkermanite rim in a powder experiment (setup a, mtc and per seeds in wo-matrix) is much wider compared to that in sandwich experiments (setup b, per | natural wo | mtc) at longer run durations.

In run IHPV 10, the distance between the mtc-ak interface and the platinum markers is 2.6 ± 0.2 μm. The distance between the platinum markers and the ak-wo interface is 2.7 ±

0.2 μm. Hence, the inert markers are located within error exactly in the center of the rim (Fig. 14a). In sandwich experiments, the åkermanite crystals develop a palisade microstructure with their long axes perpendicular to the original monticellite-wollastonite interface (Fig. 14a). After 10.04 h run duration palisade-shaped åkermanite crystals grow at either side of the original interface that is clearly visible as a suture, across which the palisades are discontinuous (Fig. 14a). During longer runs, åkermanite grains from both sides of the reaction rim tend to join up and form continuous grains. This produces a continuous palisade microstructure across the entire reaction rim (Fig. 14b). The long axes of the individual åkermanite grains are still about perpendicular to the original interface. At 60.04 h and rim widths of more than 16 μm, the palisade microstructure evolved to a mosaic microstructure with more isometric åkermanite grains (Fig. 14c). The interfaces of the reaction rim with the monticellite and wollastonite reactants are sharp and rim widths are uniform along the entire sandwich within each particular run. Neither voids nor solid inclusions occur within the åkermanite rims.

The overall thickness of the åkermanite rims increases linearly with the square root of time (Table 2; Fig. 14a-c, Fig. 15). This indicates that rim growth is diffusion-controlled (e.g. Laqua, 1978; Abart et al. 2009). The intercept of the regression line in Figure 15 clearly shows that the reaction starts immediately and is not hampered by sluggish nucleation during the incipient stage. Sandwich experiments at 1100°C and 1000°C produced significantly narrower rims than the 1200°C experiments at similar run durations (Table 2).

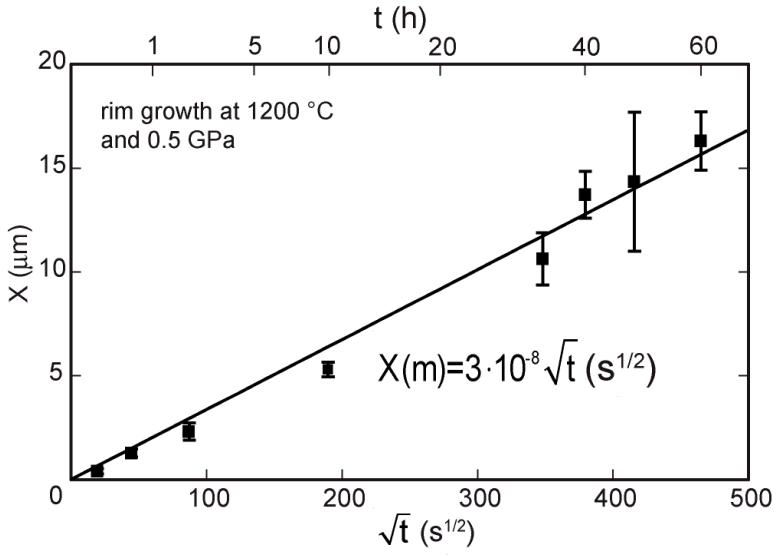

Fig.15: Plot of åkermanite rim width (μm) versus square root of time ($s^{1/2}$) for eight sandwich experiments at 1200°C, 0.5 GPa. Values are from Table 4.

Average grain widths measured parallel to the original monticellite-wollastonite interface increase with time from 0.4 to 5.4 μm, as rim widths increase from 0.4 to 16.3 μm (Table 2). Within the reaction rims, the grain widths increase with the square root of time (Fig. 16), which is consistent with the model for diffusion-controlled grain coarsening in oxides and silicates developed by Joesten (1991b). From our measurements we obtain

$$d = 0.0115\sqrt{t(s)}\,, \qquad (4)$$

where d is the grain width (μm), t the time (s) and 0.0115 the slope of the regression line (μm $s^{-1/2}$) in Figure 16.

In Figure 15 and 16, long runs show larger error bars. This is due to the fact that the interfaces of the reaction rim as well as the shape of the grains in the palisade structure become more irregular as reaction proceeds (Fig. 14a-c). Hence, the deviation of measured rim thicknesses from the average is larger in longer runs.

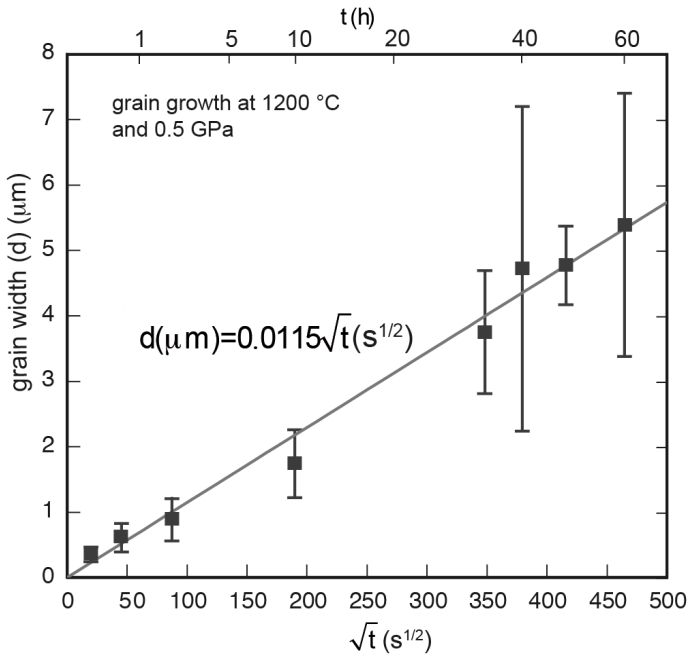

Fig.16: Plot of åkermanite grain width (μm) versus square root of time ($s^{1/2}$) for eight sandwich experiments at 1200°C, 0.5 GPa. Values are from Table 4.

In powder-experiments (setup a, mtc and per seeds in wo-matrix) åkermanite reaction rims were also produced along the monticellite-wollastonite contacts (Fig. 14d). The wollastonite matrix, which was initially introduced as fine powder, displays strong recrystallisation with concomitant grain coarsening during the experiment. The most striking feature of powder experiments is that reaction rims are five times thicker than in sandwich experiment at identical conditions and almost identical run durations with 57.3

μm at 1200°C and 33.6 h versus 10.6 μm at 1200°C and 40 h (Table 2). The åkermanite rims are largely monomineralic, however, several very small monticellite and wollastonite inclusions are present. The monticellite inclusions are located close to the monticellite seeds and the wollastonite inclusions are located close to the wollastonite matrix. They are therefore interpreted as remnants of the wollastonite and monticellite reactants, which were overridden by the quickly advancing reaction fronts. The distribution of the inclusions indicates that, similarly to the sandwich experiments, the åkermanite rim grew from the original monticellite-wollastonite interface in both directions. Altogether, the rims from the powder experiments are more irregular than those produced during sandwich experiments. Rim widths vary significantly within one experiment and both reaction fronts are strongly corrugated (Fig. 14d).

5.2 Discussion

5.2.1 Component mobility in dry single crystal sandwich experiments

5.2.1.1. Mass balance considerations

The platinum markers in experiment IHPV 10 (Table 2; Fig. 14a) and the suture in the internal structure are located exactly in the center of the reaction rim. The corresponding partial reactions may be written at the monticellite-åkermanite interface as

$$2\ CaMgSiO_4 = Ca_2MgSi_2O_7 + MgO_m, \quad (5)$$

and at the åkermanite-wollastonite interface as

$$2\ CaSiO_3 + MgO_m = Ca_2MgSi_2O_7. \quad (6)$$

Subscript “m” indicates a mobile component. This implies that rim growth exclusively occurred by the transfer of the MgO component and that CaO and SiO_2 were essentially immobile (Fig. 17a-c). Consequently, the åkermanite rim grew from the original interface into both directions, replacing wollastonite on one and monticellite on the other side. The reaction fronts at both, the åkermanite-monticellite and the åkermanite-wollastonite interfaces propagated at the same rate and equal amounts of åkermanite were produced at either side of the reaction rim. If the CaO and SiO_2 components had also been transferred across the growing reaction rim, the position of the platinum markers would have been shifted off the center of the rim towards the åkermanite-wollastonite interface (Fig. 17d).

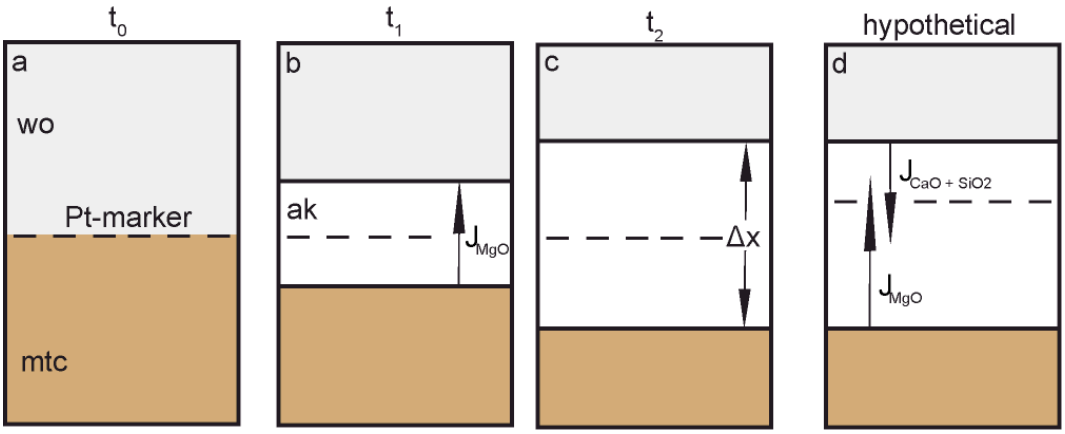

Fig.17: Sketch of successive stages of rim growth in sandwich experiments. **a:** Starting setup displaying the position of the original interface marked with platinum between wollastonite (wo) and monticellite (mtc) at t_0. **b:** reaction rim at t_1. The original interface remains at the center, indicating that equal amounts of åkermanite are produced at both reaction interfaces, which implies that MgO is the only mobile component. J_{MgO} shows the direction of the MgO flux. **c:** reaction rim at t_2 with Δx being the overall rim thickness. **d:** Hypothetical case with significant flux of $CaO+SiO_2$ in addition to MgO flux, indicated as arrow of $J_{CaO+SiO2}$. If this had occurred, the original interface would have been shifted away from the center towards the ak-wo boundary.

5.2.1.2 Thermodynamic model of reaction rim growth

Because CaO and SiO_2 are essentially immobile, these two components are combined into a single $CaSiO_3$ component. Åkermanite rim growth is therefore considered as occurring in the (pseudo)binary system MgO-$CaSiO_3$, where MgO is identified as the only mobile and $CaSiO_3$ as the immobile component.

In the following, we adopt the thermodynamic model of Abart et al. (2009) to extract the effective diffusion coefficient of the MgO component within åkermanite polycrystalline aggregates from our measured rim growth rates. This model considers chemical mass transfer, i.e. diffusion of the MgO component in the present case, across a growing reaction rim as the only dissipative process involved in rim formation. It disregards the potential contributions of nucleation and finite interface mobility to the total free energy dissipation. The dissipation through nucleation and finite interface mobility may be important during the incipient stages of reaction rim growth. However, it was shown in Figure 4 that reaction rim growth started immediately after reaching the target temperature, so that these effects can safely be ignored in our analysis.

The thermodynamic model is based on equating the chemical driving force for reaction rim growth, which is the Gibbs free energy change per unit volume åkermanite produced and the dissipation through diffusion. In their general formulation for a binary system, the rate equations developed by Abart et al. (2009; their equations 21, 26, 36) that describe reaction rim growth in planar geometry, may be rearranged to express the effective

diffusion coefficient D_{eff} that, in our case, would account for simultaneous diffusion of the MgO and $CaSiO_3$ components.

$$D_{eff} = \frac{\Delta x^2 n_{wo}^3 R_g T \left(X_{MgO}^{ak} - X_{MgO}^{wo}\right)^2 \left(X_{MgO}^{mtc} - X_{MgO}^{wo}\right)}{2\Delta_r G n_{ak}^2 t \left(X_{MgO}^{ak} - 1\right)^2 X_{MgO}^{ak} \left(X_{MgO}^{ak} - X_{MgO}^{mtc}\right)} \quad (7)$$

where R_g and T are the gas constant and absolute temperature, t is time and X_i^e is the mole fraction of component i in phase e. Δx is the total rim thickness, n_i is the total number of components in phase i and $\Delta_r G$ is the molar Gibbs free energy of reaction. The thermodynamic properties of the phases involved in the reaction are given in Table 4.

Table 4: Thermodynamic properties of educt and product phases used for the calculation of the Gibbs free energy of reaction at 0.5 GPa. Values from Holland and Powell (1990).

	$\Delta_f G$ (J/mol) (1000°C)	$\Delta_f G$ (J/mol) (1100°C)	$\Delta_f G$ (J/mol) (1200°C)
Monticellite	-2346010	-2380430	-2416170
Åkermanite	-4052660	-4113770	-4177160
Wollastonite	-1701610	-1726470	-1752280

The effective diffusion coefficient D_{eff} then accounts for simultaneous diffusion of the two components MgO and $CaSiO_3$:

$$D_{eff} = kD_{eff,CaO+SiO_2}^{ak} + (1-k) D_{eff,MgO}^{ak} \quad (8)$$

where k gives the proportion of the fluxes of the two components through the åkermanite reaction rim. We have shown above that $CaSiO_3$ is immobile compared to MgO, therefore k = 0 and D_{eff} represents the effective diffusion coefficient of MgO in åkermanite: $D_{eff,MgO}^{ak}$. The effective bulk diffusion coefficient $D_{eff,MgO}^{ak}$ is calculated to $10^{-15.8\ +/-\ 0.1}$ m^2 s^{-1} as average at 1200°C, $10^{-16.2\ +/-\ 0.1}$ m^2 s^{-1} at 1100°C, and $10^{-17.0\ +/-\ 0.2}$ m^2 s^{-1} at 1000°C. Uncertainties include the uncertainty in the temperature measurement (*see chapter 4.1.3.*) and the deviation of the rim thicknesses. In the temperature range between 1000°C and 1200°C, the temperature dependence of $D_{eff,MgO}^{ak}$ follows an Arrhenius relation (Fig. 18)

$$D_{eff,MgO}^{ak} = D_0 e^{\left(\frac{-E_a}{R_g T}\right)} \quad (9)$$

with an activation energy of E_a = 204 ± 18 kJ/mol and a preexponential factor of D_0 $=10^{-8.6\ +/-\ 1.6}$ $m^2 s^{-1}$. Uncertainties are derived from the uncertainty of the slope respectively the uncertainty of the intercept of the linear regression.

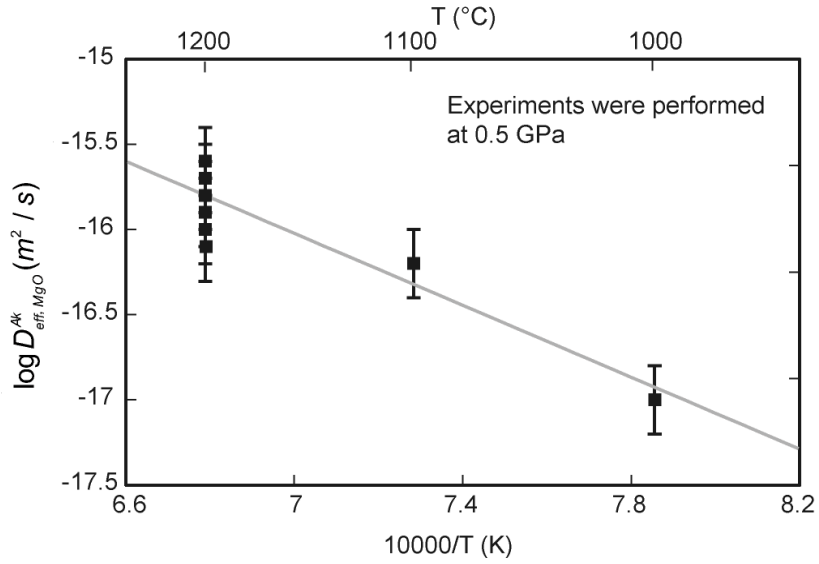

Fig.18: Arrhenius plot of the effective diffusion coefficient of MgO in åkermanite $D^{ak}_{eff,MgO}$ in the range of 1000°C to 1200°C. Values are from Table 2.

5.2.2. Effect of åkermanite grain growth

Åkermanite crystals display pronounced grain coarsening with increasing run duration (Table 2; Fig. 16). This results in a successive decrease of the grain boundary density. The structural grain boundary width, which can be measured with high-resolution-TEM (HRTEM), and the effective grain boundary width δ, that is the size of the zone across which the transport properties differ significantly from those of a bulk crystal, do not necessarily have to be identical (Abart and Sperb 2001). Thus, the effective grain boundary width is not well constrained with respect to diffusive transport. However, provided that the effective grain boundary width remains constant and irrespective of its actual size, the grain boundary area fraction in cross sections parallel to the reaction interfaces decreases with increasing grain size as reaction proceeds. Grain boundaries may be considered as two-dimensional defects in the crystal structure and it is reasonable to assume that diffusion is faster along grain boundaries than through the volume of the adjacent crystals (Joesten 1991a). Accordingly, if grain boundary diffusion was extremely fast compared to volume diffusion and hence contributed significantly to bulk mass transfer across the åkermanite rim (kinetic regime b and c according to Harrison, 1961, *see chapter 3.2.2.)*, the effective bulk diffusion would decrease with increasing grain width as reaction proceeds (Carlson and Gordon, 2004; Gardés et al., 2011). In contrast, if grain boundary diffusion occurred at a comparable rate as volume diffusion (kinetic regime a according to Harrison, 1961), the effective bulk diffusion coefficient

would be independent of the observed grain coarsening. As the grain size is large compared to the grain boundary width, this latter case would imply that grain boundary diffusion contributed a negligible fraction to bulk mass transfer and that the overall rim growth was mainly controlled by volume diffusion.

These scenarios are investigated for our 1200°C experimental time series using the approach of Harrison (1961). According to this, the effective diffusion coefficient $D^{ak}_{eff,MgO}$ may be split into the contributions from grain boundary diffusion and from volume diffusion

$$D^{ak}_{eff,MgO} = \phi_{\mathrm{gb}} D^{ak}_{gb,MgO} + \left(1-\phi_{\mathrm{gb}}\right) D^{ak}_{vol,MgO}\,, \tag{10}$$

where $D^{ak}_{gb,MgO}$ and $D^{ak}_{vol,MgO}$ are the respective diffusion coefficients and Φ_{gb} is the grain boundary area fraction, which is given by

$$\phi_{\mathrm{gb}} = \frac{\delta}{d}, \tag{12}$$

when $\delta << d$, where d is the grain width and δ the grain boundary width. Grain widths are determined in two-dimensional sections and these measurements are taken as approximations of the real grain widths (Fig. 14a-c).

Combining eqs. (9) and (10), we calculate the effect of varying proportions of $D^{ak}_{vol,MgO}$ compared to $D^{ak}_{gb,MgO}$ on the effective diffusion coefficient $D^{ak}_{eff,MgO}$ at proceeding reaction and corresponding enlargement of grains for two different grain boundary widths. We set $D^{ak}_{gb,MgO}$ to the average of the bulk diffusion coefficients for our eight 1200°C experiments ($10^{-15.8}$ m^2s^{-1}) and the initial time to 100 s. The results are shown in Figure 19.

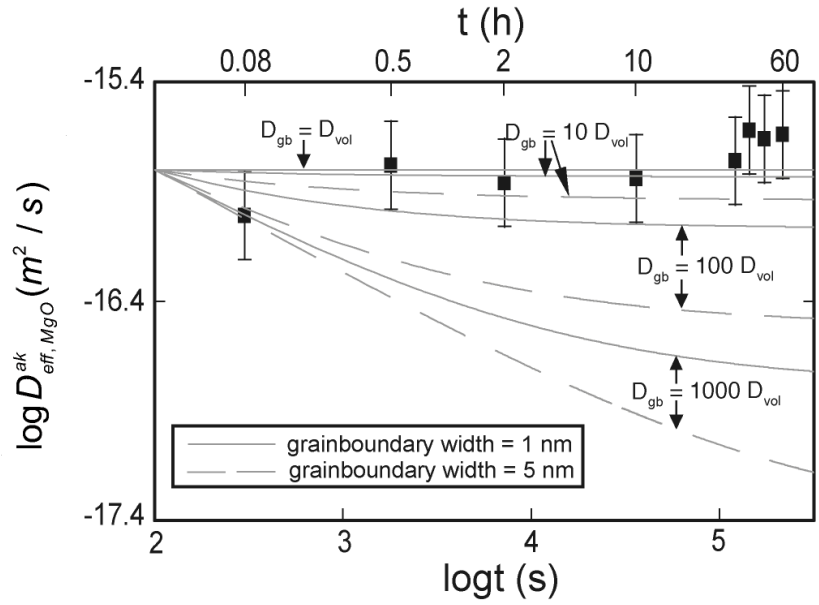

Fig.19: log $D^{ak}_{eff,MgO}$ vs log t plot illustrating how varying proportions of D_{gb} compared to D_{vol} would affect the bulk diffusion coefficient $D^{ak}_{eff,MgO}$ during ongoing reaction progress and corresponding coarsening of grains for two hypothetical grain boundary widths of 1 nm (continuous lines) and 5 nm (dashed lines). The evolution of log $D^{ak}_{bulk,MgO}$ is illustrated for D_{gb}/D_{vol} = 1, 10, 100 and 1000, with a starting point at 100 s and log $D^{ak}_{eff,MgO}$ (m^2s^{-1}) = -15.8 (average of the eight effective bulk diffusion coefficients at 1200°C). Black squares represent the experimental values from Table 2. Effective diffusivity can be described by volume diffusion alone.

It is clear that, if grain boundary diffusion equals volume diffusion ($D_{gb} = D_{vol}$ in Fig. 19), the effective bulk diffusion coefficient along the experimental time scales remains constant. Calculated curves in Figure 19 represent D_{gb}/D_{vol} = 10; D_{gb}/D_{vol} = 100, and D_{gb}/D_{vol} = 1000 and for δ = 1 nm and 5 nm, respectively. The experimentally determined bulk diffusion coefficients are also plotted along with their error bars (values from Table 2). For the observed grain coarsening and corresponding reduction of the grain boundary area fraction, it is evident that the overall diffusivity would markedly decrease, if $D^{ak}_{gb,MgO}/D^{ak}_{vol,MgO} > 100$ for δ = 1 nm and if $D^{ak}_{gb,MgO}/D^{ak}_{vol,MgO}$ > about 10 for δ = 5 nm. In case of $D^{ak}_{gb,MgO}/D^{ak}_{vol,MgO} > 1000$, $D^{ak}_{eff,MgO}$ would have been dropped by more than one log unit after 10 hours run duration, irrespective of which grain boundary widths were assumed. Concerning results of this study, $D^{ak}_{eff,MgO}$ remained unaffected (eight squares in Fig. 19) implying that the $D^{ak}_{gb,MgO}/D^{ak}_{vol,MgO}$ - ratios did not exceed a value of 10 as indicated above. This implies that the contribution of grain boundary diffusion to the effective diffusivity is negligible. Consequently, growth of the åkermanite reaction rim is

dominantly controlled by volume diffusion of MgO at our experimental conditions of 1000°C to 1200°C and 0.5 GPa dry argon pressure. This only holds under the assumption that the grain boundary width and consequently the transport properties of grain boundaries remain constant as reaction proceeds. The transport properties along grain boundaries are significantly affected by the orientation of the adjacent grains (Kaur et al. 1995, Marquardt et al. 2011) and one cannot exclude that this latter changes during rim growth. For instance, an increase of the grain boundary width during grain coarsening would result in a higher transport efficiency of the grain boundary, but this would be restrained by the decrease in grain boundary density. If these two effects were perfectly counterbalancing, this would also yield to a constant bulk diffusion coefficient. Electron backscatter diffraction (EBSD) gives information about the orientation of åkermanite crystals within the reaction rim at different time steps. This is required to examine if transport properties of grain boundaries change during rim growth.

5.2.3 Comparison with self-diffusion coefficients of Mg and O in åkermanite single crystals

Volume diffusion coefficients of Mg and O in åkermanite single crystals were determined experimentally by Yurimoto et al. (1989), Ryerson and McKeegan (1994), Ito et al. (2001) and Ito and Ganguly (2009). Diffusion experiments were performed at atmospheric pressure over a wide range of temperatures using isotopically doped åkermanite crystals. The resulting isotopic profiles were subsequently measured using secondary ion mass spectrometry (SIMS). The literature data are displayed in Figure 20, along with our experimentally determined MgO bulk diffusion coefficients for rim growth between 1000°C and 1200°C. Within uncertainty**,** the published self-diffusion coefficients for oxygen in åkermanite agree with the effective MgO component diffusivities determined from our rim growth experiments. The published self-diffusion coefficients for Mg are somewhat lower but in the range of the effective MgO diffusion coefficient (Fig. 20).

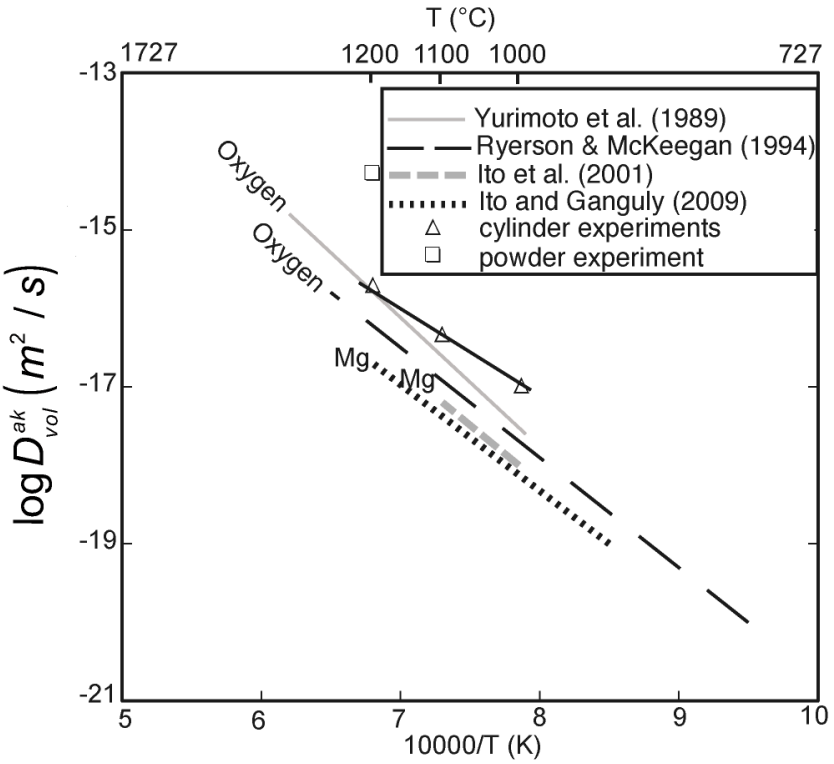

Fig.20: Arrhenius diagram of self-diffusion coefficients of O (Yurimoto et al. 1989; Ryerson and McKeegan 1994) and Mg (Ito et al. 2001; Ito and Ganguly 2009) in åkermanite single crystals. Literature data are based on dry diffusion experiments with isotopically doped crystals and isotopic concentration profiles measured by SIMS. Also plotted are effective MgO diffusion coefficients that control åkermanite rim growth between 1000°C and 1200°C (triangles: sandwich experiments, setup b, per │ natural wo │ mtc; squares: powder experiment, setup a, mtc and per seeds in wo-matrix; values from Table 2). Rim growth diffusion coefficients at dry conditions fall in the range of oxygen and magnesium self-diffusion coefficients. Our effective diffusion coefficient derived at 1200°C from the powder experiment is higher by almost two log units.

Even though the transport mechanisms may be completely different, the overall agreement between self- diffusion and rim growth data corroborates the view that growth of åkermanite reaction rims in the ternary system CaO-MgO-SiO_2 is dominantly controlled by volume diffusion of MgO and not by grain boundary diffusion.

This is in sharp contrast to the findings from dry experiments in the binary system MgO-SiO_2, where MgO grain boundary diffusion controls the kinetics of rim growth (Gardés et al. 2011) and it holds for single enstatite rims between forsterite and quartz, as well as for forsterite-enstatite double rims between periclase and quartz. Volume diffusion of the MgO component may be divided into diffusion of Mg and O. The diffusion rate of the slower part of this pair may control diffusion of the MgO-component. In enstatite, volume diffusion of oxygen is significantly slower than Mg volume diffusion (Chakraborty et al. 1994; Dohmen et al. 2002; Gardés & Heinrich 2010). In åkermanite, Mg diffusion is slower than oxygen diffusion (Fig. 20). However, at 1200°C, diffusivities

of rate limiting oxygen in enstatite are significantly lower in both, polycrystalline enstatite and forsterite, compared to Mg-diffusivities in åkermanite. Lower volume diffusivities of oxygen in enstatite and forsterite compared to Mg-diffusivities in åkermanite may suppress volume relative to grain-boundary diffusion, provided that grain boundary diffusivities are similar in both systems. Otherwise, it is quite conceivable that the two systems may fundamentally differ in the type of grain boundaries that are present in the reaction rim, which certainly will affect grain boundary diffusivities.

5.2.4. Component mobility in the presence of traces of water in powder experiments

At given P-T conditions, experiments with monticellite fragments embedded in powdered wollastonite (setup a, mtc and per seeds in wo-matrix) produced much wider åkermanite reactions rims than experiments where single crystals were used as starting material. For the experiment at 1200°C and 0.5 GPa, the effective bulk diffusion coefficient D_{eff} is $10^{-14.3 +/- 0.1}$ m^2s^{-1} (Table 2; Fig. 20), i.e. one and a half orders of magnitude higher than in dry sandwich experiments. This is interpreted as resulting from traces of water that are adsorbed on the surface of the wollastonite powder. Minute amounts of water are adsorbed even on pre-dried powder and may drastically enhance component mobility. The acceleration of reaction rates by water may result from: (i) enhanced grain boundary diffusion, (ii) formation of OH defects in åkermanite and associated enhancement of volume diffusion or (iii) changes in the reaction mechanism by additional mobilization of the CaO and SiO_2 components. The latter gains some plausibility because a similar effect was observed in the MgO-SiO_2 system for enstatite growth between forsterite and quartz (e.g. Yund 1997; Abart et al. 2004). Likewise, Milke et al. (2009b) showed that traces of water introduced by reactant powders accelerate growth rates of enstatite by several orders of magnitude. They argued that water saturation of the forsterite-enstatite-quartz charge is already achieved at H_2O concentrations below 100 ppm and speculated that in dry systems, MgO actually is the only mobile component, whereas presence of water also mobilizes SiO_2. This probably holds just as well for åkermanite growth in the CaO-MgO-SiO_2 system. Carlson (2010) calculated differences of nearly three orders of magnitude in diffusivity at 600°C between natural systems that were nearly anhydrous and those that were hydrous but fluid-undersaturated. Accordingly, it seems obvious that natural mineral coronas of a specific bulk composition, e.g. in metamorphic rocks, do not only contain the P-T-t record of a particular rock, but may also record the water content of a presumably dry system.

5.3. Conclusions

(i) In the ternary system CaO-MgO-SiO_2, single crystals of monticellite and wollastonite produce a polycrystalline åkermanite reaction rim between 1000°C and 1200°C at 0.5 GPa dry argon pressure. This is in line with the calculated åkermanite stability field in P-T-space. (ii) The direction of mass transport identified by Pt-markers in combination with mass balance considerations allows for determining the diffusing components. Growth of åkermanite under dry conditions is controlled by fast diffusion of MgO. CaO and SiO_2 are relatively immobile. On this note, the system can be treated as MgO-$CaSiO_3$ (pseudo)binary. (iii) The polycrystalline åkermanite reaction rims grow linearly with the square root of time. (iv) Åkermanite grains strongly coarsen with reaction progress. This results in a pronounced drop of the grain boundary density normal to the reaction interfaces. (v) Grain coarsening and corresponding reduction of the grain boundary density does not affect the overall rim growth rate. The effective diffusivity of MgO does not depend on the amount and density of grain boundaries. (vi) Åkermanite reaction rim growth is dominantly controlled by volume diffusion of MgO at P-T conditions relevant for the reaction mtc + wo => ak and dry vapor pressure. (vii) Minute amounts of water drastically accelerate rim growth. (viii) It is unlikely that diffusion coefficients derived from dry experiments are applicable to rim-forming reactions between nominally anhydrous minerals in rocks because presence of water, for example in form of structural OH-defects, is rather the rule than the exception.

Chapter 6

Second part

This chapter is modified after the manuscript:

"Experimental growth of diopside + merwinite reaction rims: the effect of water on microstructure development"

(submitted to American Mineralogist, 2011)

by

Bastian Joachim, Emmanuel Gardés, Boza Velickov,
Rainer Abart, Wilhelm Heinrich

6.1. Results

6.1.1. Reaction rim growth and monticellite decomposition

All experiments described in this chapter were performed in a conventional piston cylinder apparatus. A summary of used setups and pressure media, experimental conditions and the calculated effective bulk diffusion coefficients of MgO in the reaction rim ($D^{di+mer}_{eff,bulk,MgO}$, *see chapter 6.2.1.2.*) are given in Table 5.

Table 5: Run conditions, used capsule setup (a, mtc and per seeds in wo-matrix; b, per │ natural wo │ mtc) and pressure medium (assembly 1, direct contact to fluid inclusion bearing CaF_2; assembly 2, dry Al_2O_3; assembly 3, Al_2O_3-protection layer + CaF_2; for further explanation *see chapter 4.1.1.*), run duration, measured average rim thickness, average grain size (measured parallel to the original interface) and derived effective bulk diffusion coefficient of MgO in the diopside + merwinite reaction rim. All experiments were performed in a conventional piston cylinder apparatus at 900°C and 1.2 GPa. Uncertainties are given in terms of 1σ.

No. of Experiment	Capsule setup	Assembly	Run duration (h)	Rim thickness (μm)	Average grain size (μm)	$\log D^{di+mer}_{eff,bulk,MgO}$ (m^2/s)
P1	a	1	42	18.2(25)	4.3(04)	-16.3(01)
P5	a	1	20	12.2(24)	2.1(04)	-16.3(01)
P14	a	1	6,5	6.9(21)	1.3(04)	-16.3(01)
P19	a	1	5	6.63(12)	1.2(03)	-16.2(01)
P8	b	3	15	8.6(16)	0.9(02)	-16.4(01)
P9	b	3	65	20.9(15)	4.8(04)	-16.3(01)
P11	b	3	5	3.8(05)	0.6(02)	-16.6(02)
P12	b	2	15	n.a.	n.a.	n.a.
P13	b	2	25	n.a.	n.a.	n.a.

This chapter reports on growth of reaction rims produced at monticellite-wollastonite interfaces, where two settings must be discerned: (i) rims formed at the contacts between monticellite seeds and a wollastonite matrix (setup a, mtc and per sees in wo-matrix) and (ii) rims formed at the interfaces between cylindrically shaped monticellite and wollastonite single crystals (setup b, per │ natural wo │ mtc).

In experiments where only Al_2O_3 was used as pressure medium (assembly 2, dry Al_2O_3) no reaction rims were produced with the exception of rare isolated single lenses of diopside + merwinite that show a maximum thickness of 200 nm as revealed by TEM (Fig. 21a). In all other experiments, bimineralic reaction rims consisting of diopside and merwinite were grown (Fig. 21b-f), representing the stable assemblage at 1.2 GPa and 900°C (Fig. 8a, blue circle) in the CaO-MgO-SiO_2 ternary system. The corresponding reaction is represented by crossing tie lines (Fig. 9) in the ternary CaO-MgO-SiO_2 diagram.

$$2CaMgSiO_4\ (mtc) + 2CaSiO_3\ (wo) = 1CaMgSi_2O_6\ (di) + 1Ca_3MgSi_2O_8\ (mer) \quad (11)$$

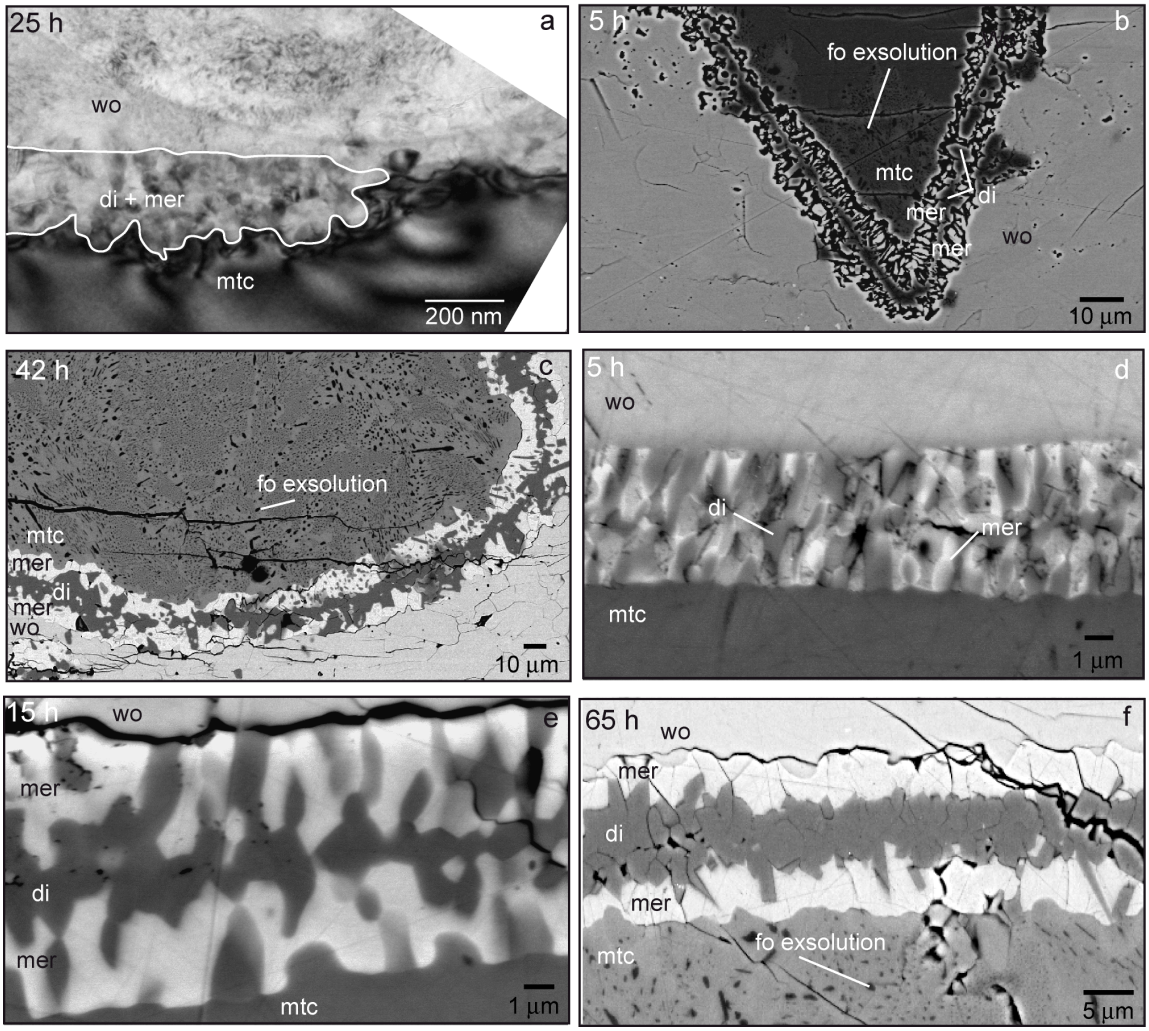

Fig.21: Backscattered electron images and TEM-image of merwinite (mer) + diopside (di) reaction rims produced between monticellite (mtc) and wollastonite (wo) at 900°C, 1.2 GPa and different run durations. **a**: sandwich experiment using setup b (per │ natural wo│ mtc), and Al_2O_3 as solid pressure medium (assembly 2, dry Al_2O_3). **b, c**: powder experiments (setup a, mtc and per seeds in wo-matrix) using solely natural CaF_2 (assembly 1, direct contact to fluid bearing CaF_2) as pressure medium. **d-f:** sandwich experiments (setup b, per │ natural wo│ mtc) using assembly 3 (Al_2O_3-protection layer + CaF_2) as pressure medium. Note different scale bars. **a:** TEM-image of run No. P13. In general, no reaction was observed after 25 h with the exception of rare isolated lenses with a maximum thickness of 200 nm consisting of diopside + merwinite. **b:** BSE image of run No. P19 showing a 6.6 µm thick diopside + merwinite reaction rim. Diopside is mainly located in the center of the rim. The monticellite reactant partly shows exsolved forsterite inclusions, indicating segregation. **c:** BSE-image of run No. P1. The overall thickness of the diopside + merwinite reaction rim increased to 20.9 µm after 42 h. The reaction rim roughly shows a "segregated multilayer type" mer | di | mer configuration. Forsterite inclusions are distributed across the whole reactant, indicating that segregation of the monticellite starting material is completed. **d:** BSE-image of run No. P11 after 5 h. Mer + di grains in the reaction rim form a cellular microstructure comprised of

elongated, palisade shaped merwinite and diopside that is oriented perpendicular to the original interface. The overall rim thickness is 3.8 μm. **e:** BSE-image of run No. P8. Run duration was 15 h. The reaction rim shows the initial stage of a reorganization towards a mer | di | mer sequence. Total rim thickness is 8.6 μm. **f:** BSE-image of run No. P9 after 65 h. Segregation into largely monomineralic layers with the sequence mer | di | mer is almost complete. The overall rim thickness is 20.9 μm. Forsterite inclusions in the monticellite reactant again indicate exsolution.

Diopside and merwinite were the only reaction products in all reaction rims and only developed along the monticellite and wollastonite interfaces. Merwinite and diopside have almost stoichiometric compositions (Table 6) and no compositional variation was detected across the reaction rim.

Table 6: Composition of reaction products merwinite and diopside and reactants after rim growth experiments (final). Values are based on the average of 15-20 single measurements. For monticellite, results are separated in one experiment using assembly 2 (dry Al_2O_3) and one experiment using assembly 3 (direct contact to fluid bearing CaF_2). The use of different assemblies has no effect on the composition of the other phases.

	Wo (final)	Mtc (final in non-exsolved assembly 3)	Mtc (final- in exsolved assembly 2)	Mer	Di
CaO	48.83(20)	32.15	35.35(04)	51.99(12)	26.76(33)
MgO	0.17(04)	28.86	27.29(19)	12.21(10)	18.41(24)
SiO_2	51.38(12)	38.92	38.84(01)	36.49(24)	55.03(28)
Total	100.38	99.93	101.48	100.69	100.20
No. of cations based on	3O	3O	3O	5O	5O
Ca	1.01	0.89	0.97	3.02	1.01
Mg	0.01	1.11	1.04	0.99	1.00
Si	0.99	1.00	0.99	1.99	1.99

The chemically homogeneous monticellite starting material (mtc I) had some forsterite component (Table 1). Monticellite seeds from powder experiments (assembly 1, mtc and per seeds in wo-matrix) and those from long-duration (t > 15 h) sandwich experiments where CaF_2 was partly used as pressure medium (assembly 3, Al_2O_3-protection layer + CaF_2) decomposed by a segregation reaction producing cellular nodules of forsterite and a less magnesian monticellite. This decomposition is not pervasive but occurs in patches that are preferentially located at the surfaces of the monticellite crystals (Fig. 21b) close to the reaction rims or spread from fractures and cracks within the original monticellite crystals. The decomposed monticellite (mtc II) has a composition of $Ca_{0.97}Mg_{1.04}Si_{0.99}O_4$ (Table 6). Consequently, it has a lower forsterite content than the original starting material. The new monticellite composition lies close to the solvus published by

Warner and Luth (1973) at 1.0 GPa and 900°C. The forsterite precipitates are too small for reliable EMP-analysis.

The spatial distribution of decomposed monticellite + forsterite patches with cellular microstructure indicates that the segregation reaction propagates from the surfaces of the monticellite crystals into the grain interiors. Forsterite is never present in the reaction rims and we therefore assume that the mtc I => mtc II + fo segregation reaction does not significantly affect rim growth. Wollastonite remained homogeneous in all used setups and assemblies. In addition to that, the compositions of the reaction products inside the reaction rims are not affected by the decomposition of monticellite.

In infrared spectra of periclase starting material, absorption bands in the range between 3100-3500 cm^{-1}, which are typical for OH-stretching vibrations, are absent. In sandwich experiments (setup b, per | natural wo | mtc), in which natural fluid inclusion bearing CaF_2 was part of the pressure medium (assembly 3, Al_2O_3-protection layer + CaF_2), IR spectra of remaining periclase taken close to complex reaction rims growing between wollastonite and periclase show three characteristic bands at 3295.5, 3301.3 and 3310.5 cm^{-1} after the experiments (Fig. 22).

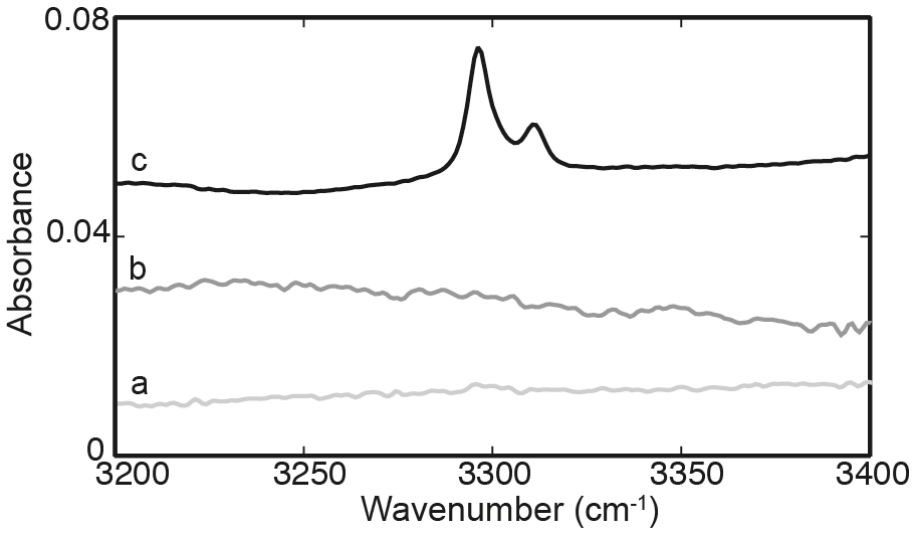

Fig.22: IR-spectra of periclase crystals. **a:** From periclase starting material used for experiment P8. **b:** From run No. P13 after the experiment, in which only Al_2O_3 served as pressure medium (assembly 2, dry Al_2O_3). **c:** From run No. P8 after an experiment, in which assembly 3 (Al_2O_3-protection layer + CaF_2) was used. Here, the IR-spectrum of periclase shows characteristic bands at 3295.5, 3301.3 and 3310.5 cm^{-1} indicating OH-defects. It was not possible to acquire IR-spectra on periclase in powder experiments (assembly 1, direct contact to fluid inclusion bearing CaF_2) after the runs, due to the small grain size used.

At least two of these bands, namely that at 3295.5 cm^{-1} and 3310.5 cm^{-1}, can safely be associated to OH-defects in the MgO-structure (e.g. Freund and Wengeler 1982). Periclase of runs performed in assembly 2 (dry Al_2O_3) with only crushed Al_2O_3 powder as pressure medium, does not show this effect (Fig. 22). This indicates that traces of water stemming from the natural CaF_2 pressure medium infiltrated into the capsule during the run, so that the presence of OH-defects in periclase can be used as a monitor for minute amounts of water. The increasing availability of water probably allowed for the cellular segregation of forsterite from mtc I and triggered the mtc I => mtc II transformation.

In the ”driest” experiments using solely Al_2O_3 as pressure medium (assembly 2, dry Al_2O_3), the rim-reaction products are only present in very small isolated lenses after 15 and 25 h respectively with a maximum thickness of 200 nm after 25 h (Fig. 21a). We believe that the formation of these rare lenses is due to trace amounts of water derived from fluid inclusions that may have been present locally in the natural wollastonite reactant used as starting material. At places where no water was released no rim growth occurred even after 25 h run duration. From this observation, we infer that minute amounts of water were required to overcome the nucleation barrier and to trigger reaction rim growth respectively monticellite exsolution. This is in line with the fact that monticellite does not decompose in very dry experiments using assembly 2 (dry Al_2O_3), or in short experiments (t <15 h; Fig. 21 d and e) using assembly 3 (Al_2O_3-protection layer), in which a certain time is needed until water stemming from the outer CaF_2-layer reaches the capsule. It is reasonable to assume that the amount of water in the capsule in experiments using assembly 3 (Al_2O_3-protection layer + CaF_2) though very small, increases with run duration, so that sufficient water is finally available and catalyses rim growth as well as the decomposition of mtc I and formation of mtc II + fo (Fig. 21f).

Monticellite grains embedded in wollastonite powder (setup a, mtc and per seeds in wo-matrix) decompose rapidly to mtc II + fo and reaction rims evolve quickly (Fig. 21b and c). There is no significant delay for both reactions, rim growth and monticellite decomposition. This is interpreted as resulting from minute amounts of water adsorbed onto the surfaces of the grains of pre-dried wollastonite powder (setup a, mtc and per seeds in wo-matrix) in combination with direct contact of the capsule to the water bearing natural CaF_2 pressure medium (assembly 1, direct contact to fluid bearing CaF_2). If so, a small but sufficiently high amount of water was available within the charge at the very beginning of the reactions, contrary to setups using

chips of single crystals (setup b, per │natural wo │mtc) in assembly 2 (Al_2O_3-protection layer + CaF_2).

6.1.2. Rim growth rates

All experiments were performed at 900°C and 1.2 GPa. Four powder experiments (setup a, mtc and per seeds in wo-matrix) using assembly 1 (direct contact to fluid bearing CaF_2) produced mer + di rims with overall thicknesses between 6.6 and 18.2 μm at run durations from 5 h to 42 h (Table 5; Fig. 21b,c). Three sandwich experiments (setup b, per │ natural wo │ mtc) using assembly 3 (Al_2O_3-protection layer + CaF_2) produced rims with overall thicknesses ranging from 3.8 to 20.9 μm at run durations from 5 h to 65 h (Table 5; Fig. 21d-f). The overall thicknesses of the diopside + merwinite reaction rims increase linearly with the square root of time in both setups (Fig. 23), indicating that rim growth is actually diffusion-controlled (*e.g.* Laqua 1978, Abart et al. 2009).

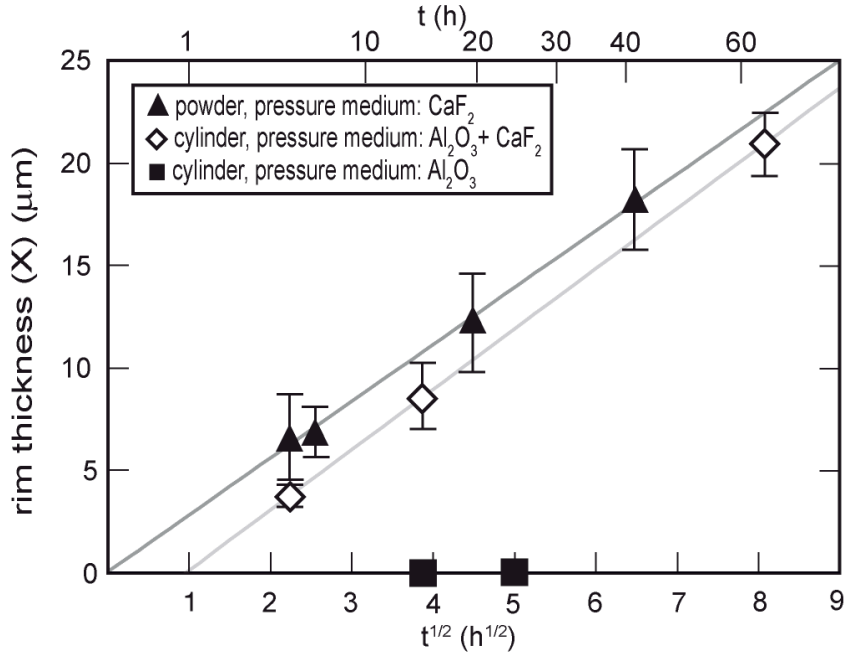

Fig.23: Plot of overall rim thickness (μm) versus square root of run duration ($h^{1/2}$) for piston cylinder rim growth experiments at 900°C and 1.2 GPa. Values are from Table 5. Black squares denote sandwich experiments (setup b, per │ natural wo │ mtc) in assembly 2 (dry Al_2O_3); triangles mark powder experiments (setup a, mtc and per seeds in wo-matrix) in assembly 1 (direct contact to fluid inclusion bearing CaF_2), and open squares sandwich experiments (setup b, per │ natural wo │ mtc) in assembly 3 (Al_2O_3-protection layer + CaF_2).

In the rim thickness versus square root of time plot (Fig. 23) both regression lines have, within error, identical slopes. This suggests identical growth rates for both experimental

settings, powder (setup a, mtc and per seeds in wo-matrix) and sandwich (setup b, per │ natural wo │ mtc) experiments. The experimental series using the two different assemblies (assembly 1, direct contact to fluid inclusion bearing CaF_2; assembly 3, Al_2O_3-protection layer + CaF_2) differ, however, with respect to the initial growth behavior. For powder experiments, the regression line hits the origin, indicating immediate nucleation and parabolic growth in the initial stages. In contrast, the regression line for sandwich experiments intersects the abscissa at about one hour, which is interpreted as a nucleation delay. The "dry" system (setup b, per │ natural wo │ mtc; assembly 2, dry Al_2O_3) did not yield any reaction except for isolated reaction lenses, supposedly in the vicinity of wollastonite hosted fluid inclusions. The "wet" system (setup a, mtc and per seeds in wo-matrix; assembly 1, direct contact to fluid inclusion bearing CaF_2) reacted instantaneously, due to adsorbed water at the surfaces of wollastonite grains in combination with direct contact to the fluid inclusion bearing CaF_2 pressure medium that causes fluid infiltration into the capsule right from the start of the experiment. A reasonable explanation for the nucleation delay in sandwich experiments (setup b, per │ natural wo │ mtc) using assembly 3 (Al_2O_3-protection layer + CaF_2) is that it takes about one hour for infiltration of water traces from the CaF_2 pressure medium into the capsules, which is necessary to catalyze nucleation and growth.

6.1.3. Development of the internal rim microstructure

Bimineralic and polycrystalline merwinite + diopside reaction rims display a distinct development with time regarding their internal intergrowth microstructure. This is highlighted in sandwich experiments (setup b, per │ natural wo │ mtc) using assembly 3 (Al_2O_3-protection layer + CaF_2). During the incipient stage of rim growth, merwinite and diopside are homogeneously distributed across as well as along the reaction rim. They form a palisade-like microstructure with merwinite and diopside microcrystals alternating at regular intervals, whereby the long axes of the grains are oriented about normal to the original monticellite-wollastonite interface (run P11, 5 h run duration; Fig. 21d). The width of the columnar grains is somewhat below 1 μm. The individual grains of both minerals are disrupted at about the center of the reaction rim, that way tracing the original wollastonite-monticellite interface and revealing that the rim grew from the original interface into both directions at about the same rates. The two compartments of the rim on either side of the original wollastonite-monticellite interface are similar in terms of modal proportions and internal microstructures. The reaction fronts towards the

wollastonite and monticellite reactants are smooth and clearly discernible. We refer to this microstructure as the "cellular type". After run durations of 15 hours, the microstructure changed. The "cellular type" microstructure developed into an intergrowth of more equidimensional and coarser crystals of merwinite and diopside, where anhedral, worm-shaped diopside tends to accumulate in the center of the reaction rim and merwinite is concentrated in the external portions on either side of the rim. Still, sporadic diopside crystals are in contact with either monticellite or wollastonite at the reaction fronts (run P8; Fig. 21e). After 65 hours, the diopside crystals have segregated completely into the center of the reaction rim. An almost perfectly segregated reaction rim has developed that consists of largely monomineralic merwinite | diopside | merwinite layers (run P9; Fig. 21f). The diopside layer is completely separated from the reactants by the two merwinite layers. Grain sizes have increased to about 4 μm and shapes have changed from anhedral to euhedral tabular. The interfaces between the two merwinite layers with the reactants at either side are smooth and occasionally show notches in the μm range. The fact that the rim is symmetric and that both merwinite layers have the same thickness strengthens the interpretation that the rim grew from the original interface, located in the center of the rim, with the same rate towards both reactants. We refer to this microstructure as the "segregated multilayer type". Powder experiments show already after short run durations an almost "segregated multilayer type" microstructure (run P19; Fig. 21b). With increasing time and overall rim thickness, the internal rim reorganization towards a mer | di | mer multilayer type becomes more pronounced (run P1; Fig. 21c). However, interfaces at both reaction fronts are more irregular here, and euhedral grains of merwinite and diopside may attain sizes of up to 10 μm or more.

6.2. Discussion

6.2.1. Overall rim growth

6.2.1.1. Mass balance considerations

We first discuss overall rim growth, which means that there is in a first step no difference between "cellular type" and "segregated multilayer type" development, i.e. that internal reorganization is disregarded. Separation of distinct merwinite and diopside layers is discussed in more detail below. We showed above that the disrupted palisade-like textures and symmetrical make-up of the reaction rims suggest that the original

monticellite-wollastonite interface was originally located precisely in the center of the reaction rim, indicating that the rim grew at the same rates from the original monticellite-wollastonite interface into both directions replacing wollastonite on the one and monticellite on the other side. This implies that equal amounts of merwinite + diopside were produced at either side of the original interface following the partial reactions.

$$2\ \text{mtc} = 0.5\ \text{mer} + 0.5\ \text{di} + 1\ \text{MgO}_m \quad (13)$$

at the monticellite | [diopside + merwinite] interface and

$$2\ \text{wo} + 1\ \text{MgO}_m = 0.5\ \text{mer} + 0.5\ \text{di} \quad (14)$$

at the wollastonite | [diopside + merwinite] interface. The subscript “m” indicates the mobile component. It is apparent that exclusively the transfer of MgO from the interface between the reaction rim and monticellite to the rim-wollastonite interface controls the overall growth rate. The observed rim geometry indicates that CaO and SiO_2 were not transferred in tandem across the rim. If the CaO and SiO_2 components had also been transferred simultaneously, the position of the original interface would have shifted off the center of the rim towards the wollastonite (Fig. 24d). Consequently, concerning overall rim growth, either CaO or SiO_2 or both were relatively immobile compared to MgO (Fig. 24a-c). This is directly comparable to experiments described in chapter 5, which showed the growth of a monomineralic single rim of åkermanite between wollastonite. These observations lead to the assumption that MgO is the growth-rate controlling component concerning reaction rim growth in the ternary system CaO-MgO-SiO_2 at dry conditions or in the presence of small amounts of water.

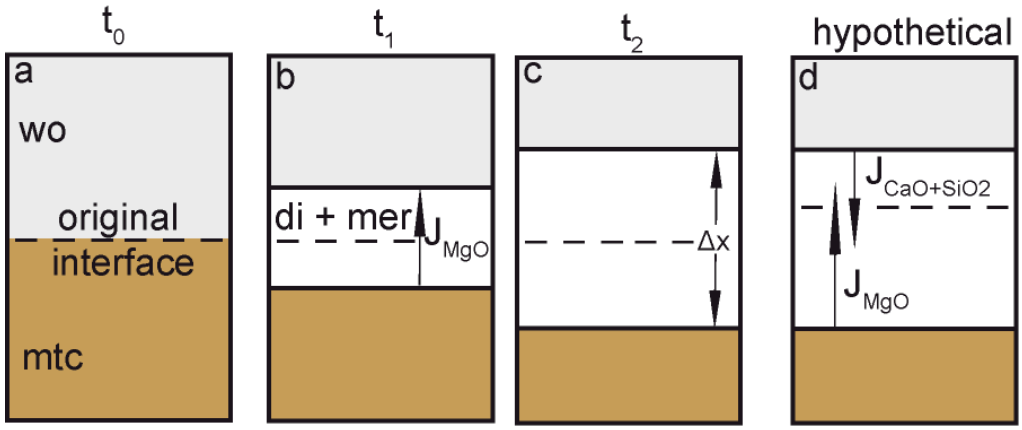

Fig.24: Sketch of successive stages of rim growth in sandwich experiments, disregarding internal rim reorganization. **a:** Starting setup displaying the position of the original interface between wollastonite and monticellite at t_0. **b:** Reaction rim at t_1. The position of the original interface remains at the center of the rim indicating that equal amounts of diopside + merwinite are produced at both reaction interfaces. This implies that solely the transfer of MgO controls overall rim growth. J_{MgO} shows the direction of MgO flux. **c:** Reaction rim at t_2. Δx is the overall rim width. **d:** Hypothetical case assuming significant flux of $CaO+SiO_2$ in addition to MgO flux, indicated as arrow of $J_{CaO+SiO2}$. If this had occurred, the original interface would have been shifted away from the center towards the [mer + di] rim | wo interface.

6.2.1.2. Thermodynamic model of reaction rim growth

Like in the previous chapter 5, overall rim growth is solely controlled by diffusion of MgO, so that two relatively "immobile" components CaO and SiO_2 are combined into a single $CaSiO_3$ component. Reaction rim growth is thus considered as occurring in the (pseudo-)binary system MgO-$CaSiO_3$, where MgO is identified as the only mobile, and $CaSiO_3$ as an immobile component. The reaction rim is approximated as a chemically homogeneous domain with the overall composition $Ca_2MgSi_2O_7$. It is important to note that this simplification is made here to develop a simple thermodynamic model for bulk reaction rim growth. It does not allow for consideration of the observed transition from the "cellular type" to the "segregated multilayer type" microstructure. This scenario is addressed below because it requires mobilization of at least one more component. The simplification appears reasonable for the analysis of bulk growth behavior.

In the following, we adopt the thermodynamic model of Abart et al. (2009) to extract the effective bulk diffusion coefficient of the MgO component within the merwinite + diopside polycrystalline aggregate from our measured overall rim growth rates. This model considers chemical mass transfer, i.e. diffusion of the MgO component in the present case, across a growing reaction rim as the only dissipative process involved in reaction rim formation. It disregards the potential contributions of nucleation and finite interface mobility to the total free energy dissipation. The dissipation through nucleation and finite interface mobility may be important during the incipient stages of reaction rim

growth (Abart and Petrishcheva, under revision). Regarding powder experiments (setup a, mtc and per seeds in wo-matrix; assembly 1, direct contact to fluid inclusion bearing CaF_2), the regression line in the rim thickness versus square root of time plot (Fig. 23) runs through the origin of the coordinate system justifying that nucleation and finite interface mobility are negligible.

The onset of rim growth in sandwich experiments (setup b, per │natural wo │mtc) using assembly 3 (Al_2O_3-protection layer) is retarded by about one hour. This is interpreted as the time span for diffusion of water traces into the capsule, which is necessary to promote the reaction. Consequently, for calculation of the effective bulk diffusion coefficient of MgO in sandwich experiments, the value of one hour was subtracted from the overall run duration. Because rim growth starts when small amounts of water are present, we treat MgO diffusion as the only dissipative process from that moment on. Still, we bear in mind that reorganization of merwinite and diopside requires internal mobility of at least one other component.

The thermodynamic model is based on equating the chemical driving force for reaction rim growth, which is the Gibbs free energy change per produced volume unit of merwinite + diopside and its dissipation through diffusion. In their general formulation for a (pseudo)binary system, the rate equations developed by Abart et al. (2009; their equations 21, 26, 36) that describe reaction rim growth in planar geometry are rearranged to express the effective bulk diffusion coefficient. In the general case this corresponds to a combined diffusion coefficient that accounts for simultaneous diffusion of both system components. In our case, this only refers to diffusion of MgO because the $CaSiO_3$ component is not transferred across the rim (*see chapter 5.2.1.2.*). The expression for the bulk diffusion coefficient of MgO in the reaction rim reads:

$$D_{eff,bulk,MgO}^{di+mer} = \frac{\Delta x^2 n_{wo}^3 \mathrm{R_g} T \left(X_{MgO}^{di+mer} - X_{MgO}^{wo}\right)^2 \left(X_{MgO}^{mtc} - X_{MgO}^{wo}\right)}{2\Delta_\mathrm{r}\mathrm{G} n_{di+mer}^2 t \left(X_{MgO}^{di+mer} - 1\right) X_{MgO}^{di+mer} \left(X_{MgO}^{di+mer} - X_{MgO}^{mtc}\right)} \qquad (15)$$

where R_g and T are the gas constant and absolute temperature, t is run duration and X_i^e is the mole fraction of component i in phase e. Δx is the total rim width, n_e is the total number of moles of components contained in one formula unit of phase e (n_{wo} = 1 and n_{mer+di} = 6) and $\Delta_r G$ is the molar Gibbs free energy of reaction at 900°C and 1.2 GPa (-12.2 kJ/mol; Holland and Powell 1998).

The mean value of the bulk diffusion coefficients of MgO in the diopside + merwinite reaction rim in powder experiments (setup a, mtc and per seeds in wo-matrix; assembly 1,

direct contact to fluid inclusion bearing CaF_2) is $10^{-16.3\ +/-\ 0.1}$ m^2s^{-1}. In cylinder experiments (setup b, per | natural wo | mtc; assembly 3, Al_2O_3-protection layer + CaF_2), we obtain $10^{-16.4\ +/-\ 0.2}$ m^2s^{-1}. No diffusion coefficient was calculated for the rare isolated lenses in very dry experiments (setup b, per | natural wo | mtc; assembly 2, dry Al_2O_3). Uncertainties represent the standard deviation of calculated effective bulk diffusion coefficients (Table 5) and include the variation in measured overall rim thicknesses. The time needed for heating and cooling was short compared to the total run duration, so that temperature correction is not necessary. In sandwich experiments (setup b, per | natural wo | mtc; assembly 3, Al_2O_3-protection layer + CaF_2), the effective experiment duration was calculated taking into account the nucleation delay of about one hour with an uncertainty of 15 min.

Except for the shortest cylinder experiment (P11, 5 h), the calculated mean bulk diffusion coefficients of MgO in the diopside + merwinite reaction rim are identical within errors for both the powder and sandwich assemblies (Fig. 25).

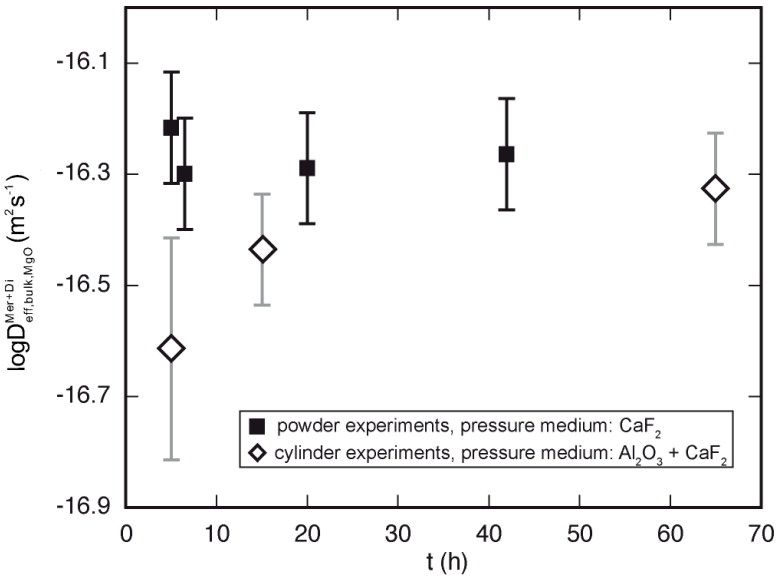

Fig.25: Effective bulk diffusivity of MgO in terms of a $D^{di+mer}_{eff,bulk,MgO}$ vs. time plot illustrating the temporal evolution of MgO mobility during ongoing reaction progress inside the merwinite + diopside reaction rim. Powder experiments (setup a, mtc and per seeds in wo-matrix; assembly 1, direct contact to fluid inclusion bearing CaF_2) show a constant MgO-mobility between 5 and 65 h. Sandwich experiments (setup b, per |natural wo | mtc; assembly 3, Al_2O_3-protection layer) show a slight increase of the effective bulk diffusivity of 0.3 log-units from -16.6 to -16.3 m^2s^{-1}.

Gardés and Heinrich (2010) showed that rim growth experiments in the MgO-SiO_2 system are governed by grain boundary diffusion as bulk diffusion of MgO decreases with grain coarsening. In contrast, Joachim et al. (2010) found in åkermanite-producing

single rim growth experiments in the MgO-CaO-SiO_2 system that the bulk diffusion coefficient was independent of grain size, which was interpreted as volume diffusion controlled rim growth.

The grain shape of the reaction products merwinite and diopside changes from anhedral to euhedral whereby the mean grain width measured parallel to the original interface increases from about 0.5 µm after 5 h to mean grain sizes in the layers of about 4 µm after 65 hours run duration (Table 5). At the same time, bulk diffusion of MgO remains almost unchanged. This suggests that rim growth mainly occurred by volume diffusion.

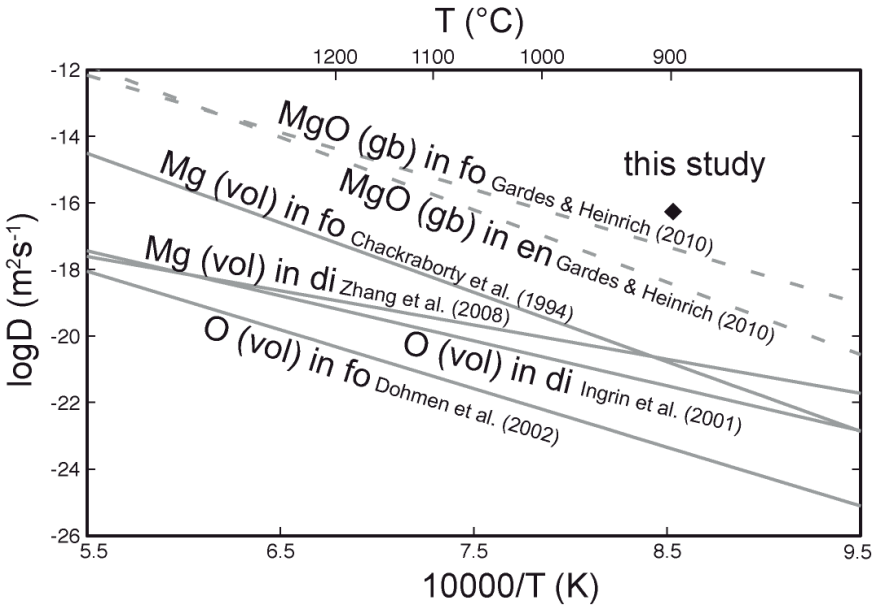

Fig.26: Comparison of the mean effective bulk diffusion coefficient of MgO in the overall diopside + merwinite reaction rim with experimentally determined grain boundary diffusivities of MgO in enstatite and forsterite (Gardés and Heinrich 2010) and volume diffusivities for Mg and O in diopside (Zhang et al. 2008; Ingrin et al. 2001) and in forsterite (Chackraborty et al. 1994; Dohmen et al. 2002). Forsterite is used because Mg and O diffusion data in merwinite are not available. Bulk diffusion data of MgO are slightly higher than grain boundary diffusion data but 4 to 6 orders of magnitude higher than volume diffusion data, indicating that reaction rim growth is mainly grain boundary diffusion controlled.

Figure 26 shows experimentally determined self-diffusion coefficients of Mg and O in diopside (Zhang et al. 2008; Ingrin et al. 2001) and, in absence of data for merwinite, in forsterite (Chackraborty et al. 1994; Dohmen et al. 2002) along with grain boundary diffusion data of MgO in enstatite and forsterite (Gardés and Heinrich 2010). The effective bulk diffusion coefficient of MgO derived in the present study is slightly higher than the grain boundary diffusion coefficients shown in Figure 26, but four to six orders of magnitude higher than the self-diffusion coefficients of Mg and O in diopside and forsterite derived by these authors. Comparison with these data suggests that reaction rim

growth in our experiments is not controlled by volume diffusion but rather by grain boundary diffusion. It remains unclear, however, why the effective bulk diffusion coefficient does not decrease during ongoing grain growth. One possible explanation is that the extent of coarsening observed in this study is about half an order of magnitude and therefore probably too small for such a correlation to be identified. For the shortest cylinder experiment (P11, 5 h; setup a, mtc and per seeds in wo-matrix; assembly 1, direct contact to fluid inclusion bearing CaF_2), the apparent bulk diffusion coefficient is somewhat lower than that for longer experiments using the same assembly (Fig. 25). This deviation may result from imprecise estimation of the nucleation delay, and therefore imposes a much larger relative error on the calculated diffusion coefficient. On the other hand, if a lower bulk diffusion coefficient at the initial stage is real, this may result from the increase in MgO mobility along grain and phase boundaries as response to progressive water uptake in the capsule during the runs. This is in line with results from our powder experiments, where adsorption of water on grain surfaces of reactants provided sufficient amounts of water to proceed the reaction from the very beginning. This is also in line with the fact that the apparent bulk diffusion coefficients for the sandwich experiments (setup b, per │ natural wo │ mtc; assembly 3, Al_2O_3-protection layer) converge at longer run durations to those for powder experiments (setup a, mtc and per sees in wo-matrix, assembly 1, direct contact to fluid inclusion bearing CaF_2; Fig. 25). Because of the differences between the two assemblies, we suggest that the MgO diffusivity in sandwich experiments attains a plateau value as soon as sufficient water had entered the system. If so, further water uptake does not affect the rim growth rate, at least within the range of our experimental conditions. This is in agreement with experiments of Milke et al. (2009b), which show that MgO diffusivities in enstatite grain boundaries were all similar in the presence of different water concentrations (Fig. 7). Results of this study imply that a plateau value, in which range diffusivities of the rim growth rate controlling component are not affected by variations in water availability, is not only observed in monomineralic enstatite reaction rims growing between forsterite and quartz but may also exist for bimineralic diopside + merwinite reaction rims growing between monticellite and wollastonite.

6.2.2. Effect of water on relative component mobilities and the internal rim organization

6.2.2.1. Diopside + Merwinite palisade rim growth

During the initial stage of rim growth in sandwich experiments (setup b, per | natural wo | mtc; assembly 3, Al_2O_3-protection layer), diopside and merwinite show palisade intergrowth referred to as "cellular type" microstructure. In our simplified model above we assumed that growth is only controlled by MgO diffusion across the rim. However, it is clear that the additional components have to be redistributed in either reaction front (e.g. Cahn 1959, Dégi et al. 2009), in this case CaO and SiO_2, because the product phases diopside and merwinite have different CaO/SiO_2-ratios, which are also different in the reactant phases. Figure 27a schematically illustrates the fluxes of all components associated with cellular type rim growth, resembling a symplectite as occurring in natural rocks.

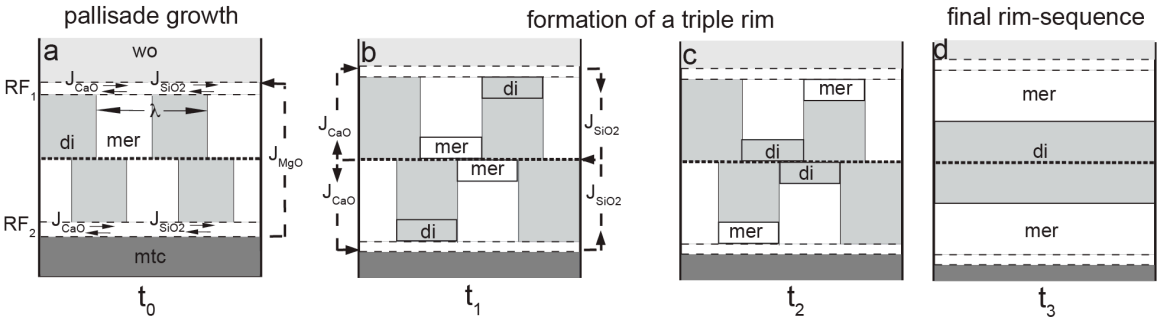

Fig.27: Sketch of successive stages of rim growth observed in sandwich experiments (setup b, per | natural wo | mtc) using assembly 3 (Al_2O_3-protection layer) as pressure medium showing the fluxes that cause evolution from a "cellular type" towards a "segregated multilayer type" microstructure. **a: "**Cellular type" microstructure. Overall rim growth is solely controlled by the diffusive flux of MgO. The original interface is located in the center of the rim. Diopside and merwinite grains are oriented normal to the original interface. Mobility of either CaO or SiO_2 or both parallel to the proceeding reaction fronts RF_1 and RF_2 is needed to produce alternating diopside and merwinite palisades. Wavelength λ is, among other factors, dependent on the relative mobilities of CaO and SiO_2 compared to MgO (Cahn 1959). **b:** "Cellular type" microstructure with fluxes that cause reorganization of the microstructure towards a "segregated multilayer type". This is generated by either a flux of CaO (left) from merwinite located in the center of the rim towards diopside located at the rim | educt interface or a flux of SiO_2 (right) in the opposite direction or a combination of both. **c:** Result of the fluxes described in b. Merwinite in the center of the rim reacted to diopside and diopside located close to the reaction fronts reacted to merwinite, indicating the initial stage of triple rim formation. **d:** "Segregated multilayer type" microstructure showing the sequence mtc | mer | di | mer | wo. Overall rim growth is still controlled by the flux of MgO. Segregation of the phases is most likely a result of increasing diffusivity of either CaO or SiO_2 or both relative to MgO (Abart et al., submitted).

In Figure 27a, the interface boundaries of the cellular reaction rim towards the reactants are outlined as reaction fronts (RF). The relative mobility of the CaO and SiO_2 components compared to MgO controls, among other parameters, the characteristic

wavelength (λ) of the palisade shaped grains of the symplectite (Cahn 1959). We developed a recently submitted thermodynamic model (Abart et al., submitted), which describes "cellular type" and "multilayer type" rim growth. It neglects the potential effects of finite interface mobility, changing grain size and associated non-ideal sources/sink of vacancies. It is assumed that the evolution of both, the cellular and the multilayer microstructure are governed exclusively by the diffusion of the CaO, MgO and SiO_2 components and only phase boundaries act as (ideal) sources and sinks for components. All diffusive fluxes are assumed to be linearly proportional to the corresponding driving forces (generalized Ficks law), where the proportionality is described by the phenomenological coefficient of diffusion. For "cellular type" rim growth, it is assumed that mobilities of the components CaO and SiO_2 are of the same order. An evolution equation for the growth of a "cellular type" reaction rim is then obtained by (Abart et al., submitted):

$$\frac{\Delta x^2}{\left(V_{di}+V_{mer}\right)\frac{L_{MgO\perp}}{L_{MgO}}}+\frac{\lambda^2\left(1-\frac{V_{mer}}{V_{di}}\right)^2\frac{L_{CaO}}{L_{MgO}}+\left(3-\frac{V_{mer}}{V_{di}}\right)^2+4\left(1-\frac{V_{mer}}{V_{di}}\right)}{12\frac{L_{CaO}}{L_{MgO}}\delta\left(V_{di}+V_{mer}\right)\left(1+\frac{V_{mer}}{V_{di}}\right)}=4L_{MgO\perp}\Delta_{rim}Gt_c \quad (16)$$

with δ being the thickness of the reaction front and λ being the characteristic palisade wavelength (Fig. 27a). V_i is the molar volume of phase i, t_c the run duration and Δx the overall rim thickness. $L_{i\perp}$ is the phenomenological coefficient of component i related to the bulk diffusion of this component across the rim. L_i is the phenomenological coefficient of component i related to diffusion in the reaction front. $\Delta_{rim}G$ is given by

$$\Delta_{rim}G=\frac{1}{2}\left[\Delta_r G+\frac{2\sigma\left(V_{di}+V_{mer}\right)}{\lambda}\right] \quad (17)$$

whereby Δ_rG is the Gibbs free energy of the reaction at 900°C and 1.2 GPa (-12.2 kJ/mol; Holland and Powell 1998). If it is assumed that the system always develops along the path that ensures a maximum rate of energy dissipation (de Groot and Mazur 1984), it is given in Abart et al. (submitted):

$$Q_c = \frac{4L_{MgO}\Delta_{rim}G^2}{\frac{\Delta x}{L_{MgO\perp}/L_{MgO}} + \frac{\lambda^2\left[\left(1-\frac{V_{mer}}{V_{di}}\right)^2\frac{L_{CaO}}{L_{MgO}} + \left(3-\frac{V_{mer}}{V_{di}}\right)^2 + 4\left(1-\frac{V_{mer}}{V_{di}}\right)^2\right]}{24\frac{L_{CaO}}{L_{MgO}}\delta\left(1+\frac{V_{mer}}{V_{di}}\right)^2}} \quad (18)$$

Assuming mobilities of CaO and SiO_2 are of the same order, it follows that $L_{CaO}/L_{MgO} = L_{SiO2}/L_{MgO}$.

According to the model, three parameters determine the microstructural development during growth, namely overall rim thickness, characteristic palisade wavelength and the relative component mobilities. A cellular microstructure develops, if two components have substantially lower diffusivities compared to the third. Provided that overall rim growth is determined by fast MgO diffusion, then formation of a cellular microstructure requires significantly slower diffusion of the two others, CaO and SiO_2. In the CaO-MgO-SiO_2 system, relative immobility of CaO and SiO_2 compared to MgO at very dry conditions was already observed in åkermanite-producing single rim reactions between monticellite and wollastonite at 1200°C and 0.5 GPa (Joachim et al. 2010; *see chapter 5*).

6.2.2.2. Segregation of monomineralic layers

As reaction proceeds, the internal microstructure in sandwich experiments (setup b, per | natural wo | mtc; assembly 3, Al_2O_3-protection layer) develops towards separated monomineralic merwinite | diopside | merwinite layers referred to as "segregated multilayer type". The thermodynamic model that we present in Abart et al. (submitted) compares the controlling parameters that produce either a "cellular type", on the one hand, or a "segregated multilayer" microstructure, on the other hand. In contrast to the "cellular", the "segregated multilayer" microstructure develops if all three components have nearly similar diffusivities, or if two components have comparable diffusivities with the third one significantly slower. We have shown above that MgO diffusivity is relatively high as it controls overall rim growth. Consequently, formation of a "segregated multilayer" microstructure would require comparably high diffusivities of either CaO or SiO_2 or both. Several cases are possible: (i) CaO diffusivity is in the same range as MgO diffusivity and the diffusivities of both are significantly higher than SiO_2 diffusivity. In this case, CaO flux from merwinite initially located in the center of the rim towards diopside initially located close to the rim-reactant interface (Fig. 27b) is required

to develop a "segregated multilayer type" microstructure. The partial reaction in the center of the rim is

$$\text{mer} - 2\ \text{CaO}_\text{m} \Rightarrow \text{di}, \qquad (19)$$

and close to the reaction fronts it is

$$\text{di} + 2\ \text{CaO}_\text{m} \Rightarrow \text{mer}. \qquad (20)$$

As a result, the merwinite located in the center of the rim reacts to diopside and the diopside located close to the reaction fronts reacts to merwinite (Fig. 21c).

(ii) Segregation may also occur by comparable MgO and SiO_2 diffusivities with low CaO diffusivity. For internal rim reorganization towards the "segregated multilayer type", flux of SiO_2 is required in opposite direction to that of CaO (Fig. 21b) following the partial reactions

$$3\ \text{di} - 2\ \text{MgO}_\text{m} - 4\ \text{SiO}_{2,\,\text{m}} \Rightarrow \text{mer} \qquad (21)$$

close to the reaction fronts and

$$\text{mer} + 2\text{MgO}_\text{m} + 4\text{SiO}_{2,\,\text{m}} \Rightarrow 3\text{di} \qquad (22)$$

in the center of the rim. (iii) If all 3 components have nearly similar diffusivities, reorganization of the internal microstructure towards a "segregated multilayer type" is a result of the additional flux of both, CaO and SiO_2. In the thermodynamic model published in Abart et al. (submitted) the simplest possible mass balance scenario is considered which is compatible with the observed geometry. This corresponds to case (i), in which it is assumed that CaO and MgO mobilities are in the same range and significantly higher than the SiO_2-mobility. An expression that describes the rate of change in Gibbs free energy during rim growth in terms of the evolution of multilayer overall rim thickness is given by Abart et al., submitted:

$$t_m = -\frac{\left(V_{di} + V_{mer}\right)/L_{MgO\perp} + V_{mer}/L_{CaO\perp}}{2\left(V_{di} + V_{mer}\right)^2 \Delta_r G} - \Delta x^2 \qquad (23)$$

It is again assumed, that the system follows the path that ensures maximum energy dissipation (de Groot and Mazur 1984). The corresponding expression describing the rate of energy dissipation for "segregated multilayer" type rim growth reads (Abart et al., submitted)

$$Q_m = \frac{\Delta_r G^2 L_{MgO} \dfrac{L_{MgO}}{L_{MgO\perp}}}{\Delta x \left(1 + \dfrac{V_{mer}/V_{di}}{\left(1 + \dfrac{V_{mer}/V_{di}}{(1+V_{mer}/V_{di})(L_{CaO}/L_{MgO})} \right)} \right)} \tag{24}$$

6.2.2.3. The effect of water on rim microstructure

Time-dependent experiments have shown that the internal microstructure developed from a "cellular type" to a "segregated multilayer type" during the course of the experiments.

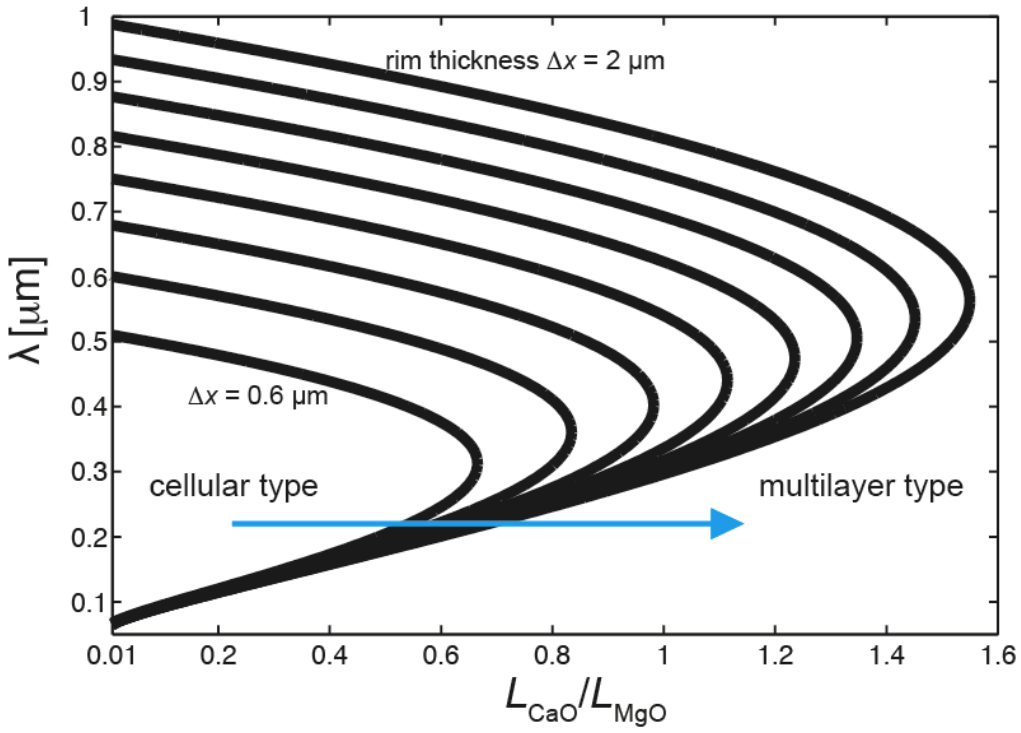

Fig.28: Kinetic regimes displayed as a function of palisade wavelength λ in the "cellular type" structure vs. L_{CaO}/L_{MgO}-ratio. Δx is the overall rim thickness, drawn between 0.6 and 2 µm with intervals of 0.2 µm. For a comparatively small L_{CaO}/L_{MgO}-ratio and a small grain width, the "cellular type" microstructure is preferred; for a high L_{CaO}/L_{MgO}-ratio, the "multilayer type" microstructure is preferred. The blue arrow displays the effect of H_2O, which is introduced in the platinum capsule during the course of the experiments. Increasing water availability results in an increasing L_{CaO}/L_{MgO}-ratio, so that the internal rim microstructure develops from a "cellular type" towards a "multilayer type" as reaction proceeds. Plot is modified according to Abart et al. (submitted).

In the thermodynamic model, that we recently submitted (Abart et al., submitted), it is assumed that the system develops always along a path that ensures maximum energy dissipation. Figure 28 shows the projection of the intersection between the two surfaces into the L_{CaO}/L_{MgO} – λ space for both microstructures the "cellular type" and the

"segregated multilayer type" (eq. 16 and 22) for different overall rim thicknesses ranging from 0.6-2 μm. As it is assumed that the maximum dissipation rate controls the development of the rim microstructure, the cellular type is preferred if $Q_c > Q_m$ and the multilayer is preferred if $Q_c < Q_m$. The parameter domain, where a "cellular type" microstructure is preferred is restricted to a comparatively low palisade wavelength and a low L_{CaO}/L_{MgO} ratio. Overall rim growth extends the "cellular type" domain (Fig. 28). For that reason, it is unlikely that a rim starts to grow in a "cellular type" microstructure and develops towards a "multilayer type" microstructure at a given L_{CaO}/L_{MgO}-ratio. This implies that relative diffusivities of either CaO or SiO_2 or both have increased compared to the diffusivity of MgO with increasing run duration, which is displayed by a blue arrow in Figure 28. It has also been shown that water infiltrated the platinum capsules during the course of the experiments, changing the system from initially dry to humid conditions. It is very likely that the increasing availability of water stemming from the solid pressure medium is responsible for the increase of the L_{CaO}/L_{MgO}-ratio and consequently for the development of the internal microstructure from a "cellular type" towards a "segregated multilayer" type.

Another observation that supports the assumption that the presence or absence of water may significantly affect the internal microstructure of a reaction rim is that powder experiments did not develop "cellular type" microstructure even after short run durations (Fig. 21b). The adsorption of water on the grain surfaces obviously provided enough water (*see also* Milke et al. 2009b, Joachim et al. 2010) to provoke directly at the beginning of an experiment a sufficiently high mobility of either CaO and/or SiO_2 compared to MgO, so that the phases in the reaction rim segregate immediately after the onset of rim growth. Thus, in addition to overall rim growth kinetics, the availability of small amounts of water significantly changes the internal rim organization. This calls for rim growth experiments with controlled low water activities.

6.3. Conclusions

(i) Reaction rims consisting of diopside and merwinite grow between monticellite and wollastonite at 900°C and 1.2 GPa. This reaction is represented by crossing tie lines in the ternary system CaO-MgO-SiO_2 and is in line with the calculated stability field in P-T-space. (ii) Textural arguments indicate that the original interface is always located in the center of the reaction rim. This and mass balance considerations let us conclude that overall reaction rim growth is solely controlled by the mobility of MgO whereas CaO and SiO_2 remain relatively immobile. (iii) The presence of small amounts of water is required to promote nucleation and initiation of growth. (iv) After reaching an MgO-diffusivity of $D_{eff,bulk,MgO}^{di+mer} = 10^{-16.3\ +/-\ 0.2}$ m^2/s at 1.2 GPa and 900°C, further water uptake at least in the frame of the here described experiments does not affect the MgO-diffusivity and consequently reaction rim growth rates. (v) An increase of the water availability significantly increases the mobility of either CaO or SiO_2 or both relative to the mobility of MgO. (vi) As a consequence, variations in the water availability affect the microstructure of the reaction rim. CaO- and SiO_2-mobilities are relatively low compared to the MgO-mobility, if only very small amounts are present, so that a cellular microstructure of alternating palisade shaped diopside and merwinite grains develops. If more water is available, either CaO or SiO_2 or both become more mobile relative to MgO, so that the product phases segregate into distinct monomineralic layers. In presence of higher amounts of available water, a triple layered rim develops with the sequence of monomineralic merwinite | diopside | merwinite.

Chapter 7

“The effect of controlled minute amounts of water on the organization of multilayered reaction rims in the binary MgO-SiO_2 and ternary CaO-MgO-SiO_2 system“

7.1. Results

7.1.1. Analysis of OH-doped Periclase

7.1.1.1. Transmission Electron Microscopy (TEM)

Synthesis of OH-doped periclase cylinders is described in the experimental methods section (chapter: 4.1.2.). OH-doped periclase starting materials were analyzed via Transmission Electron Microscopy. Before extracting foils, the periclase cylinders were carefully polished on both sides. Ion thinned foils were extracted from the center and the edge of the crystal cylinder (Fig. 13). Figure 29a shows a bright field image in transmission mode of a foil extracted from the edge of a polished, OH-doped periclase cylinder.

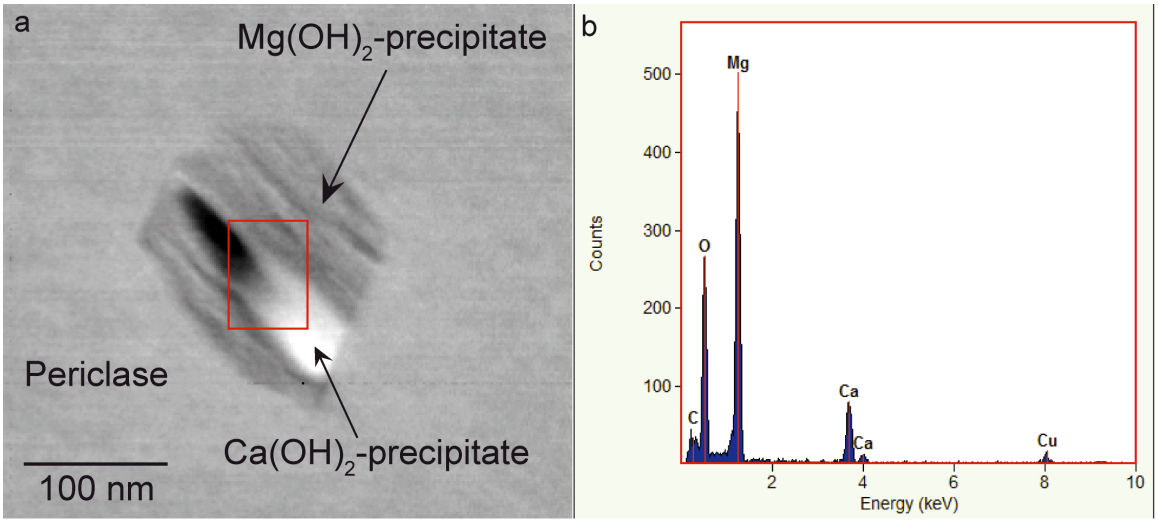

Fig. 29: TEM-analysis of an ion-thinned foil extracted from the edge (Fig. 13) of a well-polished, OH-doped periclase cylinder. **a**: Bright field image in transmission mode. In the center is a precipitate of $Mg(OH)_2$ (dark) and $Ca(OH)_2$ (bright) visible. These precipitates are only visible in foils extracted from the edge of the OH-doped periclase cylinder and not in foils extracted from the center. Red rectangle marks the position of an EDX-analysis **b**: EDX analysis of red rectangular, indicating that the precipitate consists of $Mg(OH)_2$ and $Ca(OH)_2$. Measured carbon intensities are stemming from the coating, copper intensities from the grid.

A precipitate of $Mg(OH)_2$ and $Ca(OH)_2$ of approximately rectangular shape with a side length of about 100 nm is visible within the periclase single crystal. Other measured elements were originally not part of the sample as carbon intensities are stemming from the coating and copper intensities from the grid. The precipitates are only present in foils extracted from the edge of the periclase cylinder. Foils extracted from the center do not show any precipitates but a perfect homogeneous periclase crystal. This may be explained by slow diffusion of molecular H_2O during OH-doping. Before quenching, molecular water is only present at the edge of the crystal because diffusion is not fast enough at 1200°C and 0.5 GPa to reach equilibrium after 20 h. During fast cooling, the brucite

stability field is reached at about 700°C and 0.5 GPa (Schramke et al. 1982). Consequently, $Mg(OH)_2$ precipitates are formed close to the edge of the periclase cylinder due to the reaction $MgO + H_2O \Rightarrow Mg(OH)_2$. The source for Ca remains unclear. As the precipitates are very small, it may be possible that small amounts of Ca were present in the double deionized water or, below the detection limit of the electron microprobe, in the periclase starting material.

7.1.1.2. Infrared Spectroscopy (IR)

7.1.1.2.1. Single measurements

The method of choice to quantify small amounts of water in periclase is Infrared Spectroscopy. IR-spectra of dry synthetic periclase show no bands (Fig. 30a) between 3000-4000 cm^{-1} that is the interval, in which vibrations of hydrous species are expected. We conclude that synthetic periclase starting material is completely dry within the accuracy of the measurement.

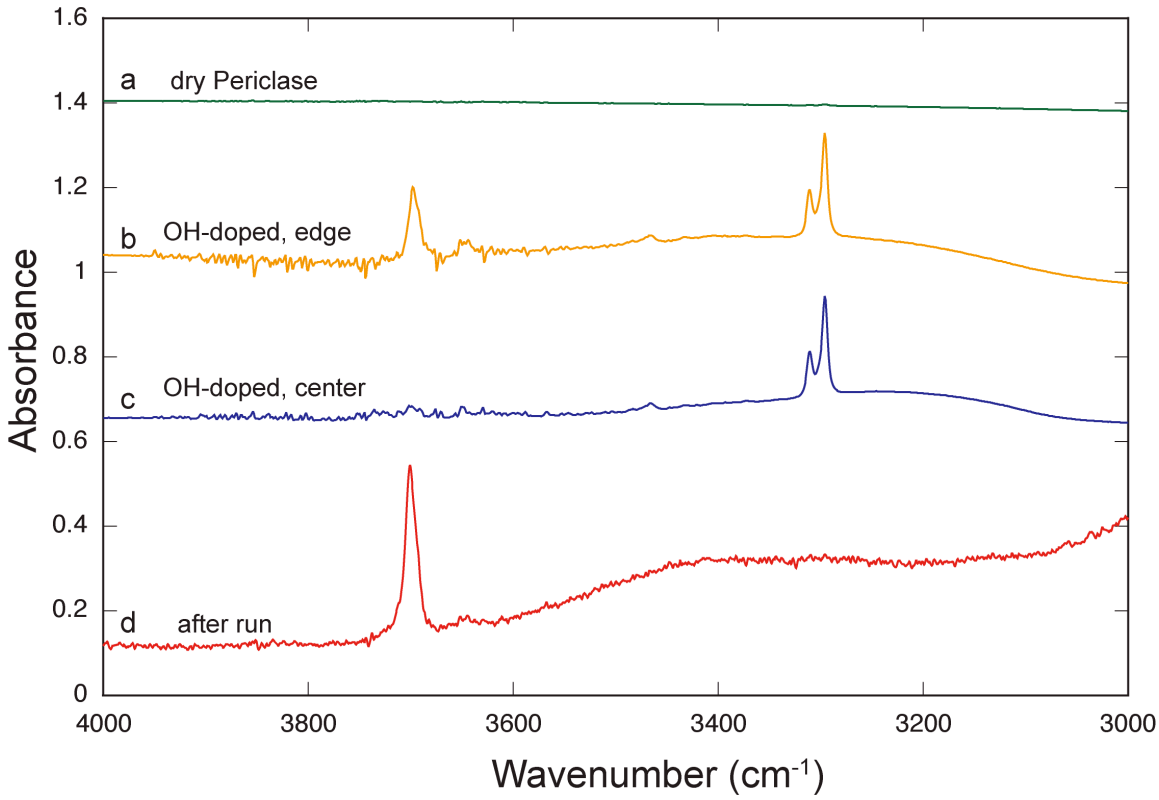

Fig. 30: IR-spectra of OH-doped periclase used for rim growth experiments **a**: Dry synthetic periclase before OH-doping. **b**: OH-doped periclase used as starting material for rim growth experiment IHPV-w1 (Table 7). Measurement was performed at the edge (Fig. 13) of a polished cylinder. The spectrum shows characteristic bands at 3295.5 and 3310.5 cm^{-1} indicating OH defects and bands at 3644 and 3697 cm^{-1} that are associated to $Ca(OH)_2$ respectively $Mg(OH)_2$ precipitates **c**: OH-doped periclase starting material (IHPV-w1) as shown in (b); the spectrum was measured in the center of a polished cylinder. Bands indicating precipitates are absent. **d**: OH-doped periclase after a rim growth experiment (IHPV-w1). Only a band at 3697 cm^{-1} that indicates $Mg(OH)_2$ precipitates and a broad band between 3200-3600 cm^{-1} indicating molecular H_2O is observed. Bands indicating OH-defects are absent. Cooling rate was 10 K/min.

After OH-doping, IR-measurements were performed in the center and at the edge of polished cylinders (Fig. 13). Spectra observed from measurements taken in the center of the crystals (Fig. 30c) show bands at 3297, 3302 and 3310.5 cm^{-1}. At least two of these bands may safely be associated to OH-defects in the MgO structure, as the bands at 3297 and 3310.5 cm^{-1} are interpreted as OH stretching vibrations (Freund and Wengeler, 1982). All three bands were also observed in IR-spectra recorded at the edge of the cylinder. The integrated intensity of these bands is almost identical independent from the position of the IR-measurements, implying that OH-defects are homogeneously distributed in the doped periclase. In contrast to measurements recorded in the center, IR-spectra measured at the edge of the periclase cylinder show additional bands at 3644 and 3697 cm^{-1}. These may be interpreted as OH stretching vibrations in $Ca(OH)_2$ (3644 cm^{-1}; Phillips et al. 1956) and $Mg(OH)_2$ (3697 cm^{-1}; Freund and Wengeler, 1982). This is in good agreement with results of TEM-images that show precipitates of $Mg(OH)_2$ and $Ca(OH)_2$ only in foils extracted from the edge of periclase cylinders (Fig. 29).

In order to use an OH-doped periclase as water source for rim growth experiments, a homogenous distribution of OH-defects within the crystal is required. As $Mg(OH)_2$ and $Ca(OH)_2$ precipitates are not homogenously distributed after the doping procedure, further preparation of the starting material was required before using it for rim growth experiments (*compare 4.1.1.*). This is demonstrated in Figure 31.

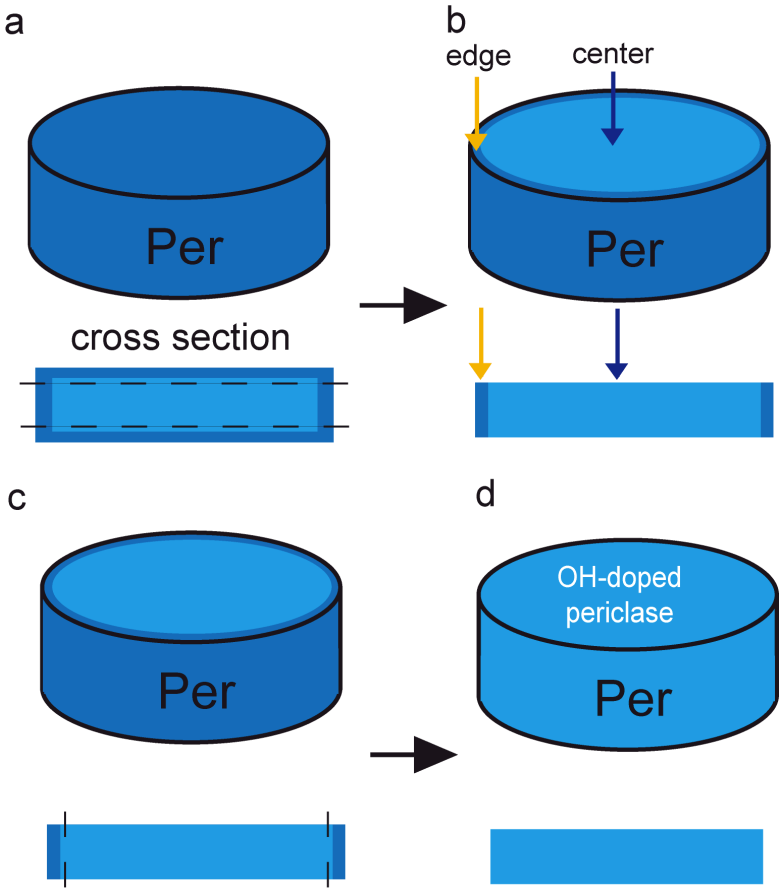

Fig. 31: Schematic three dimensional view and cross section of OH-doped periclase illustrating the preparation for rim growth experiments **a**: Unpolished periclase cylinder after doping experiment with core, in which only homogeneously distributed OH-defects are present (light blue) and outer layer (dark blue, thickness: ~ 100 µm), in which in addition to OH-defects, $Ca(OH)_2$ and $Mg(OH)_2$ precipitates have been observed. Dashed lines in cross section represent the first polishing step. **b**: Cylindric crystal after the first polishing step. The yellow and blue arrow mark the position of IR-measurements and extracted foils used for TEM-measurements. **c**: Dashed lines in cross section represent second polishing step. **d**: Only homogeneously distributed structural OH-defects are present in the completely prepared periclase cylinder, which is usable as starting material for rim growth experiments.

A schematic, three-dimensional sketch in Figure 31a illustrates the water distribution within a periclase cylinder after a doping experiment. In a cross section, it is visible that water in the center (light blue) of the crystal is only present as structural OH-defect. In the outer rim (dark blue), water is present as structural OH-defect and in addition to that in form of $Ca(OH)_2$ and $Mg(OH)_2$ precipitates. In a first step, both flat surfaces were polished. Figure 31b shows the position in the center and at the edge of the cylinder, where IR-measurements were performed and foils were extracted for Transmission Electron Microscopy. The color-coding in the cross section (Fig. 31b) illustrates, that $Ca(OH)_2$ and $Mg(OH)_2$ precipitates are only present at the edge of the periclase cylinder (dark blue). In a second polishing step, the outer rim (about 150 µm) was removed, so

that the diameter of the periclase cylinder was downsized from 2.8 to 2.5 mm (Fig. 31c). The observed crystal cylinder shows a homogeneous distribution of structural OH-defects and is usable as starting material for rim growth experiments.

Due to a lack of specific absorption coefficients for periclase, we use the calibration of Libowitzky and Rossmann (1997) to quantify the hydrogen concentration expressed as H_2O-equivalent in MgO-starting materials. Because spectra were measured in unpolarized light, total absorbance (A_i) has been calculated by multiplying the integrated absorbance by three. The absorption coefficient ε_i (cm^{-2}/mol H) for each band was calculated according to Libowitzky and Rossmann (1997)

$$\varepsilon_i = 246.6 \cdot \left[3753 - \nu\right] \qquad (25)$$

with ν being the mean wavenumber of the respective stretching band. The water concentration c (wt% H_2O) is given by

$$c_{\mathrm{H2O}} = \frac{A_i \cdot 1.8}{d \cdot \rho \cdot \varepsilon_i} \qquad (26)$$

with ρ being the density of periclase at 1 bar and 25°C (3.58 g/cm^3) and d (cm) the thickness of the sample. The Libowitzky and Rossmann (1997) calibration gives 6 ppm H_2O in doped periclase starting material. After a rim growth (IHPV-w1, Table 7) experiment, an average value of 10 ppm is obtained whereby the H_2O-concentration is affiliated to $Mg(OH)_2$ precipitates (band position: 3697 cm^{-1}) that are not homogeneously distributed in the MgO-crystal (*see chapter 7.1.2.2.*). It is important to note that the use of this calibration method has a high uncertainty, if it is used for minerals or glasses that contain only traces amounts of water on the ppm-level. Calculated values may differ from calibration curves estimated for specific nominally anhydrous minerals by up to a factor of four (Pawley et al. 1993, Koch-Müller et al. 2001). For that reason, Raman spectroscopy was used as an independent method to determine the water concentration in OH-doped periclase starting materials.

Figure 30d shows an IR-spectrum of an OH-doped periclase after a rim growth experiment. A broad band between 3200-3600 cm^{-1} and a strong band at 3697 cm^{-1} is observed. All bands related to structural OH-defects are absent (3297, 3302 and 3312 cm^{-1}). Rim growth experiments using OH-doped periclase as starting material were cooled down slowly (10 K/min) to minimize cracks and allow for preparation of the crystal sandwich. At high temperatures, protons are randomly distributed throughout the crystal and freeze in their substitutional sites during fast cooling, forming structural OH-defects as observed after water-doping of periclase starting material. However, if the

crystal is cooled down slowly the protons will move and have ample opportunity to aggregate in $Mg(OH)_2$ precipitates due to the reaction:

$$MgO + H_2O = Mg(OH)_2 \quad (27)$$

Therefore, the relative intensities of the 3296 cm^{-1} band related to structural OH-defects and the 3697 cm^{-1} band associated to $Mg(OH)_2$ precipitates are reversible indefinitely by alternate slow cooling and quenching. (Chen et al., 1977). Consequently, slow cooling after rim growth experiments, in which periclase with structural OH-defects as starting material was used, results in an increased absorption of the 3697 cm^{-1} band and a decrease in the intensity of the band at 3296 cm^{-1} (Fig. 30d). The broad band observed between 3200-3600 cm^{-1} may be associated to molecular H_2O, which was probably introduced during sample preparation and not during the experiment itself, as all samples were embedded in water containing epoxy before polishing that is still present in small cracks.

7.1.1.2.2. Mapping

After rim growth experiments, samples were cooled down slowly with 10 K/min to minimize cracks and allow for preparation. As a result, $Mg(OH)_2$ precipitates were formed instead of structural OH-defects, which were initially present in the quenched, OH-doped periclase starting material (see reaction 25). Consequently, a map of the distribution of $Mg(OH)_2$ precipitates after slow cooling is, if mobility during cooling is neglected, representative for the OH-defect distribution at the end of the rim growth experiment before cooling. Figure 32b displays a color-coded map of the relative ratio of the integral absorbance of the 3650-3750 cm^{-1} absorption band, which is related to $Mg(OH)_2$ (Freund and Wengeler, 1982).

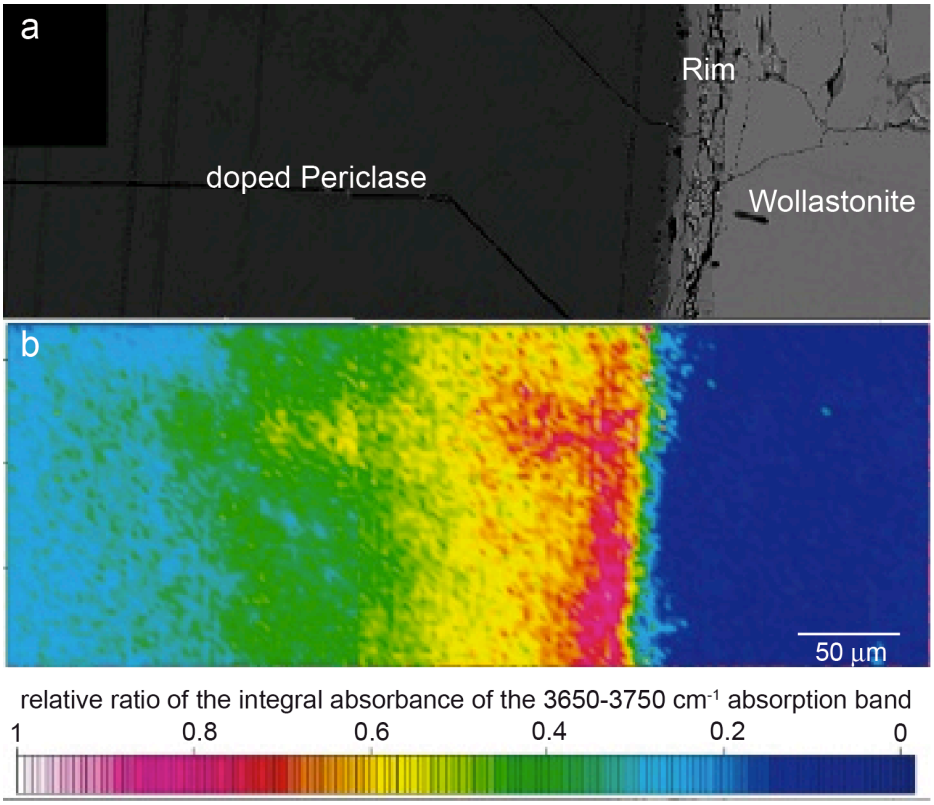

Fig. 32: a: BSE-image of the original periclase-wollastonite interface in experiment IHPV-w1 (Table 7), performed at 1200°C and 0.5 GPa for 20 h. **b:** Color-coded map of the same area, showing the relative ratio of the integral absorbance of the 3650-3750cm^{-1} absorption band in IR-spectra, representing the OH-defect distribution in periclase at the end of a rim growth experiment before slow cooling (10 K/min). By using a Focal Plane Area-detector, the spatial resolution of the MIR-signal is only limited by the wavelength of the IR-radiation (3.3 µm at 3000 cm^{-1}, Prechtel and Stalder, 2009)

Doped periclase starting materials show a homogeneous structural OH-defect distribution before a rim growth experiment. It is striking that after 20 h at 1200°C and 0.5 GPa, these defects are not distributed homogeneously anymore, but a concentration maximum has developed towards the reaction rim growing between periclase and wollastonite. The OH-defect concentration is decreasing with increasing distance to the reaction rim, until a minimum plateau is reached at a distance of about 200 µm. The concentration maximum was only observed towards the reaction rim and not elsewhere.

It is very likely that the reaction rim is not oriented perfectly perpendicular to the sample surface, so that parts of the $Mg(OH)_2$ containing periclase below the surface were measured, despite, according to the BSE-image, a measurement of product phases in the rim is expected. For that reason we assume that the observed relative ratio of the integral absorbance of 0.2-0.4 at a position, where a reaction rim is visible in the BSE-image may be interpreted as an artifact and not as presence of $Mg(OH)_2$ precipitates in the product phases.

7.1.1.3. Raman spectroscopy

For quantification of the water content in OH-doped periclase, which will afterwards be used as starting material for rim growth experiments, Raman spectroscopy was performed as an independent method in addition to infrared spectroscopy. Figure 33 shows a Raman spectrum measured in the center of a polished OH-doped periclase starting material.

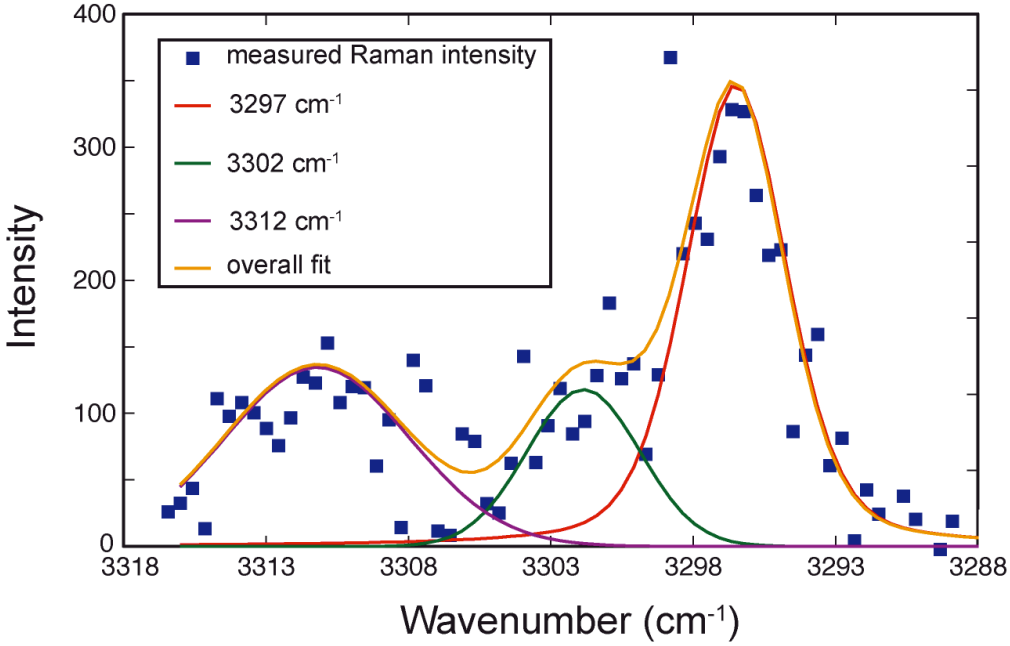

Fig.33: Raman spectrum measured in the center of OH-doped periclase starting material used for experiment IHPV-w1. The calculated fit (yellow line) is obtained by the sum of three single bands at 3297 cm^{-1} (red line), 3302 cm^{-1} (green line) and 3312 cm^{-1} (purple line).

In addition to measured Raman intensities, the calculated overall fit (yellow line) is displayed, which was obtained by using the PeakFit software from Jandel Scientific. The overall fit is based on the sum of three single bands at 3297, 3302 and 3312 cm^{-1}. At least two of these, namely the bands at 3297 and 3312 cm^{-1} may be safely related to OH-defects in the MgO-structure as they are in good agreement with obtained IR-spectra that show bands at almost identical positions (Fig. 30b,c). An H_2O-bearing SiO_2-glass with a known concentration of 332 ppm was measured as a reference in order to calculate the water content in OH-doped periclase starting materials (*see chapter 7.2.1.2.*).

The Comparator technique for water quantification developed by Thomas et al. (2008) was applied to derive the water concentration. Assuming that three single bands at 3297, 3302 and 3312 cm^{-1} are related to OH-defects in the periclase structure, the sum of the integral of these three bands was used to determine the water content. A glass standard with known water content (332 ppm) was measured as a reference. Counting times were normalized to 100 s. The water concentration was calculated according to Thomas et al. (2008),

$$c_{H_2O} = I_{corper} \frac{c_{H_2O\_ref}}{I_{ref}} \tag{28}$$

with I_{ref} being the intensity of the reference and I_{corper} the corrected intensity of the sample.

$$I_{corper} = I_{per} c_{V\_per} \frac{100}{c_{R\_per}} \tag{29}$$

Because measurement of Raman-spectra of periclase and glass are not depended on crystallographic orientation, sample orientation was neglected. C_{V_Per} is a correction factor accounting for the different sample volume in periclase compared to the reference glass and is given by ρ_{glass}/ρ_{per} (Thomas et al., 2008). C_{R_V} accounts for the difference in reflectivities between the glass standard and the OH-doped periclase (93.7). An average value of 7 ppm was obtained using the Comparator technique, which is in very good agreement with observed H_2O-concentration determined via IR-spectroscopy (6 ppm H_2O). Based on the very good agreement of two independent methods, it may safely be assumed that the water concentration of OH-doped periclase starting materials is in the dimension of 10 ppm.

7.1.2. Multilayered reaction rim growth

In all runs, a multilayered reaction rim formed. A summary of used setups, run conditions and observed rim sequences is given in Table 7.

Table 7: Run conditions, used capsule setups observed rim sequences at the original per-wo interface and original per-qtz interface if available and the forsterite/enstatite thickness ratio. Uncertainties are given in terms of 1σ. The periclase-quartz interface was not analyzed in sample IHPV-w-3 due to preparation problems. All experiments were performed at 0.5 GPa and 1200°C.

No. of Experiment	Run duration (h)	Capsule setup	Rim sequence: original interface per-qtz	Rim sequence original interface Per | Wo	Fo/En-thickness ratio
IHPV-d-1	20	syn wo | per | qtz	per | fo | en | qtz	per | ak | wo	2.4(3)
IHPV-w-1	20	Syn wo | OH-per | qtz	per | fo | en | qtz	per | fo | mtc | mer | ak | wo	10.4(4)
IHPV-d-3	1	syn wo | per | qtz	per | fo | en | qtz	per | ak | wo	2.5 (2)
IHPV-w-3	1	syn wo | OH-per | qtz	n.a.	per | fo | mtc | isolated mer lenses | ak | wo	n.a.
IHPV5	48.04	nat wo | OH-per | qtz	n.a.	per | fo | ak | wo	n.a.
IHPV3	33.71	mtc and per seeds | wo matrix	n.a.	per | fo | mtc | mer lenses | ak | wo	n.a.
IHPV6	48.04	mtc and per seeds | wo matrix	n.a.	per | fo | mtc | ak | wo	n.a.

7.1.2.1. System MgO-SiO$_2$

In both experiments, monomineralic double layers were formed between periclase and quartz showing the sequence quartz | enstatite | forsterite | periclase (Fig. 34).

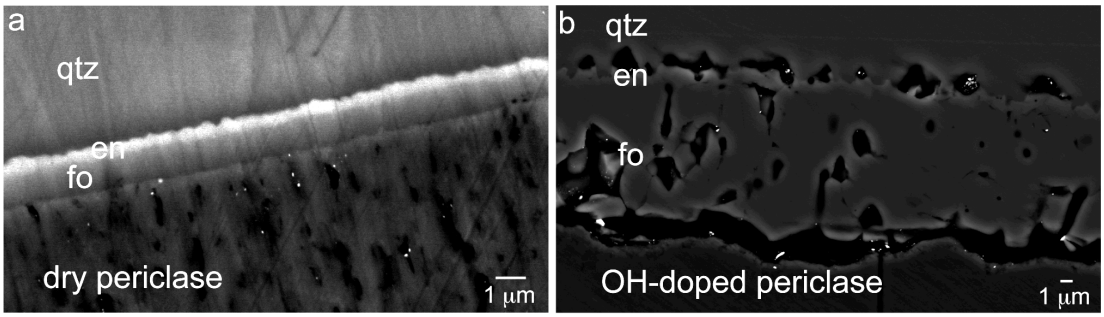

Fig.34: EMP backscattered electron micrographs of forsterite-enstatite double layers growing between periclase and quartz. **a:** Sandwich experiment (IHPV-d1; setup c, synthetic wo | per | qtz) performed at 1200°C and 0.5 GPa for 20 h using synthetic dry starting materials. Overall rim thickness is 1.3 ± 0.1 (1σ) μm with a forsterite-enstatite thickness ratio being 2.4 ± 0.3 (1σ). **b:** Sandwich experiment (IHPV-w1) performed at identical conditions using OH-doped periclase (setup d, synthetic wo | OH-doped per | qtz) as starting material. Overall rim thickness is 11.9 ± 0.3 (1σ) μm with a forsterite-enstatite thickness ratio being 10.4 ± 0.4 (1σ).

The overall reaction is given by Gardés et al. (2011):

$$\nu\ SiO_2\ (qtz) + MgO\ (per) = (2\nu\text{-}1)\ MgSiO_3\ (en) + (1\text{-}\nu)\ Mg_2SiO_4\ (fo) \qquad (30)$$

Reaction products showing this rim sequence were only formed along the original quartz-periclase interface. The phase sequence is in agreement with local equilibrium at the layer-interfaces (Fig. 8). The forsterite-enstatite interface as well as the interfaces towards the educts quartz and periclase are sharp in both setups. However, all interfaces are more irregular in the experiment using OH-doped periclase.

The overall rim thickness and thickness ratio of enstatite and forsterite varies significantly. In experiments that use OH-doped periclase as a source for small amounts of water, an increase in the overall rim thickness, i.e. 11.9 ± 0.3 (1σ) μm compared to 1.3 ± 0.1 (1σ) μm for dry synthetic periclase is observed at identical run duration. This is consistent with several other experimental studies (e.g. Yund 1997) and the results are displayed in chapter 5, which show that åkermanite growth between monticellite and wollastonite is drastically enhanced in the presence of small amounts of water.

The forsterite/enstatite thickness-ratio in dry experiments gives 2.4 ± 0.3 respectively 2.5 ± 0.2 (1σ; Table 7). This is in very good agreement with values observed by Gardés et al. 2011, who performed dry rim growth experiments between periclase and quartz at 1.5 GPa and 1200°C for 24 h in a piston cylinder apparatus. They observed the identical rim sequence with a forsterite/enstatite ratio of 2.4 ± 0.2 (1σ).

In experiments using OH-doped periclase as starting material, a forsterite/enstatite thickness ratio of 10.4 ± 0.4 (1σ) is observed. Consequently, small amounts of water do not only have a major effect on overall rim growth rates but also on relative thickness ratios in multilayered reaction rims.

7.1.2.2. System CaO-MgO-SiO$_2$

BSE-images of rim growth experiments using all four different setups are shown in Figure 35.

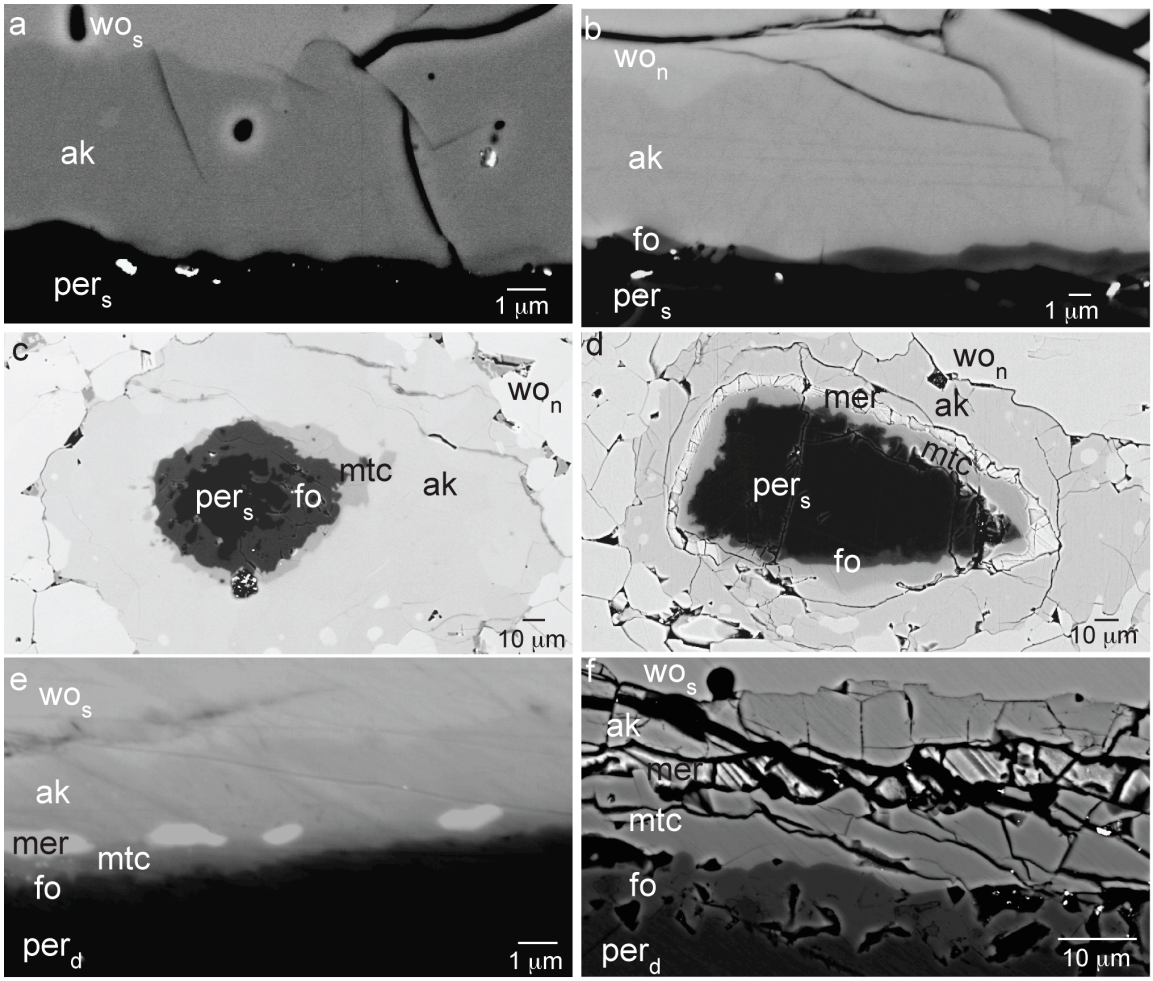

Fig.35: Backscattered electron image micrographs of reaction rims produced between periclase and wollastonite at 1200°C and 0.5 GPa in the presence of variable, small amounts of water. Footnotes mark the different starting materials of periclase and wollastonite used in the four capsule setups. "s" stands for synthetic, "n" for natural and "d" for OH-doped. **a:** Run No. IHPV-d-1 (Table 7) after 20 h run duration using dry synthetic cylindrical single crystals as starting material (setup c, synthetic wo$_s$ | per$_s$ | qtz). A monomineralic single layer of åkermanite formed. **b:** Run no. IHPV 5 after a run duration of 48 h. A natural wollastonite cylindrical single crystal was used as starting material (setup b, per$_s$ | natural wo$_n$ | qtz). A monomineralic åkermanite rim is observed. Forsterite is partly present in small lenses (left) or as a layer (right) separating periclase and åkermanite. **c:** Run No. IHPV 6 after 48.06 h run duration. Setup c (mtc and per$_s$ seeds in wo$_n$-matrix) was used. The rim sequence per$_s$ | fo | mtc | ak | wo$_n$ is observed. Remnants of periclase in forsterite and wollastonite in åkermanite are visible close to the respective starting material. **d:** Run no. IHPV 3 after 33.71 h. Conditions and starting materials were almost identical to run No. IHPV 6. Monticellite and åkermanite are partly separated by merwinite (upper part) so that the overall rim sequence per$_s$ | fo | mtc | mer | ak | wo$_n$ is observed. **e:** Run no. IHPV-w-3 after 1 h run duration using an OH-doped cylindrical periclase single crystal as starting material (setup d, synthetic wo$_s$ | OH-doped per$_d$ | qtz). The

rim sequence per_d | fo | mtc | ak | wo_s is observed. Monticellite and åkermanite are partly separated by small isolated merwinite lenses. **f:** Run no. IHPV-w-1 after 20 h run duration. Setup d (synthetic wo_s | OH-doped per_d | qtz) was used. The rim sequence per_d | fo | mtc | mer | ak | wo_s is observed with merwinite being a continuous layer in contrast to the short experiment IHPV-w-3 (Fig. 35f).

The below described reaction rim-sequences only formed at the original periclase-wollastonite interface. Very dry experiments using solely synthetic starting materials (setup c, synthetic wo | per | qtz) show the rim sequence periclase | åkermanite | wollastonite (Fig. 35a). Overall rim thickness is 5.3 ± 2.1 μm after 20 h at 1200°C and 0.5 GPa. It is important to note that neither monticellite nor any other phase was observed at the periclase-åkermanite interface, which was expected assuming local equilibrium at each interface. Interfaces between the åkermanite rim and the reactants are smooth and show occasionally notches in the μm range.

Experiments using natural, fluid inclusion bearing wollastonite instead of a synthetic one (setup b, per | natural wo | mtc) show the rim sequence periclase | forsterite | åkermanite | wollastonite. The overall rim thickness is 7.4 ± 2.4 μm after 48 h at identical P-T-conditions. The forsterite layer is partly continuous (Fig. 35b right) and partly present in the form of isolated lenses (Fig. 35b left). We assume that the presence of small amounts of water derived from the fluid inclusions that are locally present in the natural wollastonite starting material have an effect on forsterite nucleation and growth.

In powder experiments (Fig. 35c,d; setup a, mtc and per seeds in wo-matrix), water was introduced in fluid inclusions present in the natural wollastonite and in small but relevant amounts as adsorbed surface water present on the pre-dried starting materials. Two different rim sequences are observed. Experiment IHPV-3 (Fig. 35c) shows the rim sequence periclase | forsterite | monticellite | åkermanite | wollastonite, experiment IHPV-6 partly the identical rim sequence (Fig. 35d, lower part) and partly the rim sequence periclase | forsterite | monticellite | merwinite | åkermanite | wollastonite (Fig. 35d, upper part). All layers in powder-experiments are largely monomineralic despite the outer part of the åkermanite and the inner part of the forsterite layer, in which several wollastonite respectively periclase inclusions are present, interpreted as remnants of the starting materials that were overridden by quickly advancing reaction fronts. The interfaces of all layers are strongly corrugated. The wollastonite matrix shows strong recrystallisation with concomitant grain coarsening. Relative thickness ratios of the different phases match in the fact that the thickness of åkermanite is about two third of the thickness of the overall rim. This is not the case for the relative monticellite and forsterite thicknesses that vary significantly in different powder experiments (Fig. 35c and d), despite, the used

setup (a, mtc and per seeds in wo-matrix) as well as the P-T conditions (1200°C, 0.5 GPa) were identical.

Figures 35e and f show images of experiments using OH-doped cylindrical periclase single crystals (setup d, synthetic wo | OH-doped per | qtz) as starting material, so that controlled amounts of water were introduced. Water is first present in form of structural OH-defects in the MgO-structure. This implies that it is not available at the periclase-wollastonite interface at the beginning of the experiment. As reaction proceeds, periclase is consumed and simultaneously water is released, which is from that moment on available and may affect the rim growth reaction. Figure 35e and f show a multilayer rim, growing between OH-doped periclase and wollastonite after 1 h respectively 20 h. The one-hour experiment shows the rim sequence periclase | forsterite | monticellite | åkermanite | wollastonite. All layers are monomineralic and show smooth interfaces towards the neighboring phases. Some isolated lenses of merwinite separate the monticellite and the åkermanite layer. This is directly comparable to the observed rim sequence in powder experiment IHPV 3 (setup a, mtc and per seeds in wo-matrix), in which water was introduced as adsorbed surface water and in form of fluid inclusions present in the natural wollastonite. The 20-hour experiment shows the rim sequence periclase | forsterite | monticellite | merwinite | åkermanite, which is partly identical with the observed rim sequence in powder experiment IHPV 6 (Fig. 35d, upper part). Grains in the åkermanite layer display a palisade texture with elongation perpendicular to the original interface. Merwinite ($Ca_{2.98}Mg_{1.01}Si_{2.01}O_8$) and åkermanite ($Ca_{2.02}Mg_{0.98}Si_{2.00}O_7$) have almost ideal composition, whereas monticellite and forsterite deviate from endmember composition (Table 8).

Table 8: Composition of run products in experiment IHPV-w1. Values represent averages based on 5 to 20 point analyses using a JEOL FEG-EMP instrument. Uncertainties are given in terms of 1 σ.

	Forsterite	**Monticellite**	**Merwinite**	**Åkermanite**
CaO	2.97(12)	31.30(36)	48.27(31)	41.14(82)
MgO	52.79(38)	30.09(34)	11.53(16)	14.54(21)
SiO_2	42.16(68)	38.86(10)	36.06(50)	43.27(29)
Total	97.91(68)	100.25(28)	95.87(21)	99.00(92)
No. of cations based on	4 O	4 O	8 O	7 O
Ca	0.08	0.85	2.98	2.02
Mg	1.91	1.15	1.01	0.98
Si	1.01	1.00	2.01	2.00

EMP-analysis of forsterite gives $Ca_{0.08}Mg_{1.91}Si_{1.01}O_4$, the analysis of monticellite $Ca_{0.85}Mg_{1.15}Si_{1.00}O_4$, which implies that forsterite has some CaO-component and monticellite some forsterite component. The composition of these two phases lies close to the solvus published by Warner and Luth (1973) at 1.0 GPa and 1200°C. No compositional variation was detected within a single phase.

It is striking that the merwinite layer is continuous after a comparably long run duration (20 h, Fig. 35f) separating monticellite and åkermanite, which is not the case after 1 hour run duration (1h, Fig. 35e). Another important issue is that the thickness of the forsterite and monticellite layer significantly increases relative to the thickness of the åkermanite layer with increasing run duration.

7.2. Discussion

7.2.1. Water distribution after rim growth experiments using OH-doped periclase as starting material

Assuming that water has been released during the course of the reaction due to the consumption of OH-doped periclase, we may assume that it is present as a free fluid phase. If so, it will dissociate to a certain amount to $2H^+$ and O^{2-}. A possible explanation for the observed concentration maximum towards the reaction rim is the replacement of Mg^{2+} by $2H^+$ at this position. In combination with the remaining O^{2-} anion, a mobilized MgO-component is given, which is required for reaction rim growth. If this is true, we may conclude that an increase of structural OH-defects in the periclase lattice towards the rim is directly related to the reaction rim growth reaction. The OH-doped periclase starting material would not be consumed during this process.

7.2.2. Effect of H_2O on rim sequence and growth kinetics

7.2.2.1. System MgO-SiO_2

During consumption of OH-doped periclase, water is released, which is from that moment on available as a catalyst and may affect reaction rim growth. The overall rim thickness of a forsterite-enstatite double layered rim growing between periclase and quartz is increased by a factor of 8 after 20 h at 0.5 GPa and 1200°C in experiments using OH-doped instead of dry synthetic periclase as starting material. This is in good

agreement with results of several studies (e.g. Yund 1997, Fisler et al. 1997, Milke et al. 2009b, Joachim et al. 2011), which have shown that presence of minute amounts of water significantly enhances rim growth rates.

However, small amounts of water do not only affect overall rim growth rates but also the relative forsterite/enstatite thickness-ratio, which is 2.4 ± 0.3 (IHPV-d1, Table 7) at dry conditions using synthetic periclase and 10.4 ± 0.4 (IHPV-w1) using OH-doped periclase at identical P-T-t-conditions (0.5 GPa, 1200°C, 20 h). Gardés et al. (2011) showed that growth of a forsterite-enstatite double rim between periclase and quartz is solely controlled by MgO-diffusion at dry conditions. The forsterite/enstatite thickness ratio is proportional to the $D^{fo}_{MgO} / D^{en}_{MgO}$-ratio. If we assume that this is also the case in presence of small amounts of water, an increase in the relative forsterite/enstatite thickness-ratio may be explained by an increase of the MgO-diffusivity in forsterite relative to enstatite by a factor 5. Another possibility is, that SiO_2 is mobilized in presence of water, so that diffusion of two components, MgO and SiO_2, controls overall rim growth. Relatively slow SiO_2-diffusion in enstatite compared to forsterite may increase the forsterite/enstatite thickness ratio. Regardless of which component mobility is rate limiting, it is striking that the relative mobility ratio(s) of the growth rate limiting component(s) control the thickness ratio of individual layers in a multilayered rim sequence. Gardés et al. (2011) have shown that the thickness distribution of layers in a reaction rim is affected by temperature variations. This study shows that this is also the case for variations in water concentration.

7.2.2.2. System CaO-MgO-SiO_2

All experiments were performed at identical p-T-conditions (1200°C, 0.5 GPa), so that they are only affected by the presence of different water concentrations. Variable amounts of water are introduced into the capsule by using four different setups (*see chapter 7.1.2.2.*). Very dry rim growth experiments (setup c, synthetic wo | per | qtz) show a single, monomineralic åkermanite layer growing between synthetic periclase and synthetic wollastonite single crystals (Fig. 35a). For the growth of this layer, only MgO-mobility is required as the CaO/SiO_2-ratio is constant in the product phase and the reactants (Fig. 8b). With increasing water concentration, first forsterite (Fig. 35b), followed by monticellite (Fig. 35c) and finally merwinite (Fig. 35d) appear in the rim sequence, so that in experiments having the highest water concentration within this study, the rim sequence per | fo | mtc | mer | wo (Fig. 35d) is observed. Growth of forsterite and

merwinite requires mobility of either CaO or SiO_2 or both as the CaO/SiO_2-ratio of these product phases differs compared to the CaO/SiO_2-ratio of the reactants. This implies, that the presence of small amounts of water significantly enhances the mobility of either CaO or SiO_2 or both relative to MgO, which is in good agreement with results observed in chapter 6. There, it has been shown that small amounts of water significantly increase the mobility of either CaO or SiO_2 or both relative to the MgO-mobility, which results in a reorganization of the internal microstructure of a bimineralic diopside + merwinite reaction rim growing between monticellite and wollastonite that develops from a "cellular type" towards a "multilayer type" (*see chapter 6.2.2.2.*). Consequently, seeing forsterite and merwinite in the layer sequence growing between periclase and wollastonite implies that a change of relative component mobilities caused by introduction of small amounts of water may not only affect the internal microstructure of bimineralic layers but also the layer sequence in a multilayered reaction rim.

Another striking point is that at very dry conditions (setup c, synthetic wo | per | qtz) only a monomineralic single rim of åkermanite grows between periclase and wollastonite. The absence of other phases in the reaction rim implies that the assumption of local equilibrium at the layer-interfaces is not fulfilled. A simple collinear rim-sequence respecting local equilibrium at the layer interfaces with MgO as only mobile component is given by periclase | monticellite | åkermanite | wollastonite (Holland and Powell 1998, Fig. 8b). However, monticellite is only observed in experiments using setup a (mtc and per seeds in wo-matrix; Fig. 35c, d) and setup d (wo | OH-doped per | qtz) having a small but higher water concentration compared to very dry experiments. A comparable phenomenon has already been observed in experiments concerning the formation of small isolated bimineralic diopside + merwinite lenses between monticellite and wollastonite in dry cylinder experiments as reported in chapter 6. Their formation was predicted in terms of local equilibrium at the layer interfaces but was only observed at places where trace amounts of water were present derived from fluid inclusions that may have been present locally in the natural wollastonite reactant used as starting material. At places where no water was released, no rim growth occurred even after 25 h run duration.

This implies that a minimum water concentration is required to obtain a reaction rim sequence respecting local equilibrium at the layer interfaces. At very dry conditions, the absence of water impedes nucleation of product phases because it is required as a catalyst for the nucleation process.

Now immediately the question occurs why åkermanite is nucleating at very dry conditions but not monticellite?

The growth of a monomineralic single layer of åkermanite between periclase and wollastonite and absence of monticellite implies that the water concentration that is required to initiate nucleation of monticellite is higher than for åkermanite. Consequently, every single phase in a multilayered rim sequence has an individual minimum water concentration that is required to initiate its nucleation. A rim sequence that respects local equilibrium at the interfaces is only observed, if the water concentration in the experiment is higher than the respective minimum water concentration of all required product phases. Based on the observed layer sequences developing between periclase and wollastonite at 1200°C and 0.5 GPa in presence of various water concentrations (Fig. 35, Table 7), we conclude that the minimum water concentration required for åkermanite growth is smaller than the respective for forsterite, followed by monticellite and finally merwinite.

It is important to note that mass balance is not fulfilled in the rim sequences per | fo | ak | wo (Fig. 35b) and per | fo | mtc | ak | wo (Fig. 35c) due to the presence of forsterite, which is the only non-linear phase in these layer sequences (Fig. 8b). The rim sequence per | ak | wo (Fig. 35a) and the rim sequence per | fo | mtc | mer | ak | wo (Fig. 35d) respect mass balance. As the system is closed and no other phases were observed elsewhere, we assume that in non-linear layer sequences, in which forsterite and no merwinite is observed, CaO is present as a mobile component in the fluid, so that mass balance is respected.

We assume that the water concentration in experiments using OH-doped periclase as starting material (setup d, synthetic wo | OH-doped per | qtz) is increasing with increasing experiment duration due to the continuous consumption of periclase during rim growth and the accompanied release of water. After one hour at 1200°C and 0.5 GPa (Fig. 35e), the observed rim sequence is comparable to experiments performed using setup a (mtc and per seeds in a wo-matrix; Fig. 35d). Presence of isolated merwinite lenses between monticellite and åkermanite indicates that the water concentration is in the range of the minimum concentration that is required to initiate merwinite nucleation and growth. After 20 hours run duration, the merwinite layer is continuous. The overall rim thickness increased from 3.6 ± 0.2 μm after one hour to 28.7 ± 1.9 μm after 20 hours. This indicates that with ongoing reaction, a larger amount of OH-doped periclase has been consumed and consequently more water has been released, so that the water

concentration is above the minimum concentration required for nucleation of all four phases, forsterite, monticellite, merwinite and åkermanite, that are observed in the overall rim sequence. Consequently, presence of small amounts of water not only affects relative thickness ratios but also the layer sequence in a multilayered reaction rim.

Apart from that, reaction rims growing between periclase and wollastonite also show a variation in relative thickness ratios of the individual layers in presence of variable amounts of water. The increased water concentration after a run duration of 20 hours results in a significant increase of the thicknesses of forsterite and monticellite relative to åkermanite, which is displayed in Table 9.

Table 9: Evolution of relative forsterite/åkermanite, monticellite/åkermanite and merwinite/åkermanite thickness ratios in the rim sequence developing between wollastonite and OH-doped periclase (setup d, synthetic wo | OH-doped per | qtz) with increasing run duration. Experiment IHPV-w-3 (1 h run duration) shows only isolated lenses of merwinite (Fig. 35 e). Longer experiment duration is equivalent to higher water availability due to the continuous consumption of periclase during rim growth and simultaneous release of water, initially incorporated as OH-defect in the periclase structure.

	Fo/Ak	Mtc/Ak	Mer/Ak
IHPV-w-3 (1 h run duration)	0.3 ± 0.1	0.4 ± 0.1	n.a.
IHPV-w-1 (20 h run duration)	0.6 ± 0.2	0.9 ± 0.2	0.4 ± 0.2

This implies, that the mobility of the rim growth-controlling component(s) is increasing in these layers relative to the respective mobility in åkermanite in presence of higher amounts of available water. A comparable effect has been shown above, concerning changes in the thickness distribution of forsterite-enstatite double-layered rims growing between periclase and quartz that is strongly affected by the presence of minute amounts of water.

7.3. Conclusions

(i) Periclase, doped with water at 1200°C and 0.5 GPa for 20 h in the IHPV, shows a homogeneous distribution of structural OH-defects with a concentration of about 10 ppm, expressed as H_2O-equivalent. This has been shown via IR- and Raman spectroscopy. (ii) Reactants are consumed during reaction rim growth. During the consumption of OH-doped periclase water is released. The amount of consumed periclase and thus released water increases with increasing run duration. (iii) The use of OH-doped nominally anhydrous minerals as starting material allows performing rim growth experiments in presence of small controlled amounts of water. (iv) Minute amounts of water are a necessary catalyst to enhance nucleation. Every layer in a multilayered rim structure has an individual minimum water availability that is required to promote nucleation and

growth. Concerning rim growth between wollastonite and periclase at 1200°C and 0.5 GPa, åkermanite requires the lowest minimum H_2O-availability for nucleation, followed by forsterite, monticellite and finally merwinite. The layer sequence of a multilayered rim has thus the potential to act as an indicator for small amounts of water. (v) Minute amounts of water drastically accelerate overall rim growth in single and multilayered reaction rims. (vi) Variations in the water availability may change the relative mobility of growth rate controlling component(s) in the individual layers of a multilayered rim sequence. The thickness ratio of the respective layers may therefore act as an indicator for small amounts of water.

8. Outlook

In chapter 5, it has been concluded that there is a fundamental difference in the transport mechanism of the MgO-component diffusing through enstatite layers growing between forsterite and quartz, and åkermanite layers growing between monticellite and wollastonite. In contrast to enstatite reaction rim growth, growth rates of åkermanite reaction rims remain constant as reaction proceeds and do not show a decrease. This led us to the assumption that a change in the grain boundary density does not affect åkermanite grain growth and that, consequently, åkermanite reaction rim growth is mainly controlled by volume diffusion, whereas enstatite rim growth is mainly grain boundary diffusion controlled. A possible explanation for the completely different development of the effective bulk diffusion coefficient of MgO in the enstatite respectively åkermanite reaction rim is that the misorientation of adjacent grains and, consequently, the transport properties along grain boundaries differ significantly in the two systems. Electron backscatter diffraction measurements of the orientation of enstatite and åkermanite rims will give information about a potential difference between the grain boundaries present in both systems and may check this assumption. Another possibility is that increase of the grain boundary width during grain coarsening would result in a higher transport efficiency of the grain boundaries. This effect would be restrained by the decrease in grain boundary density. If these two effects were perfectly counterbalancing, this would also yield to a constant åkermanite growth rate despite rim growth is grain boundary diffusion controlled. EBSD-measurements of the orientation of åkermanite crystals within the reaction rim at different time steps are required to examine, if grain misorientation and therefore transport properties of grain boundaries change during rim growth.

In chapter 6, a model has been developed that describes evolution of the microstructure of a bimineralic diopside + merwinite reaction rim growing between monticellite and wollastonite at 900°C and 1.2 GPa from a "cellular type" towards a "segregated multilayer type" as a result of increasing water availability. It has been shown that only MgO-mobility controls overall rim growth. An increase of the relative mobility of either CaO or SiO_2 or both compared to MgO results in reorganization of the rim microstructure. Performing rim growth experiments using isotopically doped wollastonite ($^{44}Ca^{29}SiO_3$) followed by nano-SIMS measurements allow to distinguish in the reaction rim between calcium and silicon stemming from wollastonite respectively monticellite. If the model and the relative fluxes described in chapter 6 (Fig. 27) are correct, the two merwinite layers should show completely different isotopic composition with $^{44}Ca_3Mg^{29}Si_2O_8$ at the rim-wollastonite interface and $^{40}Ca_3Mg^{28}Si_2O_8$ at the rim-monticellite interface.

In chapter 7, rim growth experiments were performed between periclase and quartz respectively periclase and wollastonite in presence of various amounts of water. The usage of OH-doped periclase as starting material allows introducing controlled minute amounts of water into the experimental setup. During the course of the experiment, OH-doped periclase is consumed and water is released. For exact quantification of the amount of released water and the estimation of component mobilities, it is necessary to identify the original interface between the starting materials. There are two possible ways that may lead to the identification of the exact position of the original interface after a rim growth experiment: (i) Inert platinum markers deposited on the surface of starting materials may mark the original interface as shown in experiments producing a single layer of åkermanite between monticellite and wollastonite (*see chapter 5*). (ii) Crystal orientation maps measured via EBSD may give textural information on the position of the original interface as shown by Abart et al. (2004).

Svoboda et al. (2010) developed a model that allows direct calculation of the position of layer interfaces and Kirkendall planes in a multilayered rim sequence grown between multi component starting materials subject to relative diffusivities of the respective components in the individual layers. It is based on the assumption that the velocities of the interfaces relative to the lattice are the kinetic controlling variables and uses the Onsager principle of maximum dissipation to derive the equations. By knowing the temporal evolution of the exact interface and Kirkendall plane positions, which could be visualized via EBSD measurements or Pt-markers, we could use this model to estimate

relative diffusivities of MgO, CaO and SiO_2 in every individual layer of the observed layer sequences growing between periclase and wollastonite.

We were able to measure the water distribution in formerly OH-doped periclase after a rim growth experiment (Fig. 32). In order to estimate the amount of water that was available as a catalyst for nucleation and growth, it is important to have detailed information about the water distribution in every phase involved in the experimental setup. We were not able to measure this because water-containing glue was used to stabilize the product phases inside the reaction rim during polishing. Consequently, it is not known if bands in Raman- or IR-spectra, measured on the product phases, are related to water that was present during the rim growth reaction itself or to water incorporated in glue that was used for preparation. Therefore, a completely dry preparation method is needed. This will allow quantification of free molecular water and structural OH-defects in quartz and wollastonite starting materials via IR- or Raman-spectroscopy. Product phases in reaction rims need, due to their small thickness in the μm-range, to be analyzed using a quantification method with high spatial resolution, which is e.g. provided by synchrotron Infrared-spectroscopy.

We assume that all phases in a multilayered reaction rim differ in the minimum water availability that is required to promote nucleation and growth of the respective phase. The amount of available water in experiments using OH-doped periclase as starting material is increasing with increasing experiment duration due to the continuous consumption of OH-doped periclase during rim growth. We assume that after one hour experiment duration, the amount of available water is close to the minimum availability required for nucleation of merwinite, indicated by the presence of isolated lenses (*see chapter 7.2.3.2.*, Fig. 35e). The minimum water availability for nucleation of åkermanite, forsterite and monticellite is somewhat lower as they are continuous layers. Experiments performed with various small undefined amounts of water introduced into the capsule by the use of different setups (setup c, synthetic wo | per | qtz; setup b, per | natural wo | qtz; setup a, mtc and per seeds in wo-matrix) indicate that the minimum water availability required for nucleation and growth of åkermanite is smaller than for forsterite, followed by monticellite and finally merwinite. A time series with durations ranging from a few minutes to one hour followed by determination of the position of the original interface as well as of the water distribution in all educt and product phases allows the quantification of minimum water availabilities required for nucleation and growth of all four product phases.

9. References

Abart R, Petrishcheva E, Joachim B (submitted) Thermodynamic model for growth of cellular reaction rims. *American Mineralogist*.

Abart R, Kunze K, Milke R, Sperb R, Heinrich W (2004) Silicon and oxygen self-diffusion in enstatite polycrystals: the Milke et al. (2001) rim growth experiments revisited. *Contributions to Mineralogy and Petrology* **147**, 633-646.

Abart R, Petrishcheva E, Fisscher FD, Svoboda J (2009) Thermodynamic model for diffusion controlled reaction rim growth in a binary system: application tot he forsterite-enstatite-quartz system. *American Journal of Science* **309**, 114-131.

Abart R, Schmid R, Harlov D (2001) Metasomatic coronas around hornblendite xenoliths in granulite facies marble, Ivrea zone, N-Itally II: oxygen isotope patterns. *Contributions to Mineralogy and Petrology* **141**, 494-504.

Abart R, Sperb R (2001) Metasomatic coronas around hornblendite xenoliths in granulite facies marble, Ivrea Zone, N-Italy II: oxygen isotope patterns. *Contributions to Mineralogy and Petrology* **141**, 473-493.

Ashworth JR, Birdi JJ (1990) Diffusion modelling of coronas around olivine in an open system. *Geochimica et Cosmochimica Acta* **54**, 2389-2401.

Ashworth JR, Sheplev VS (1997) Diffusion modelling of metamorphic layered coronas with stability criterion and consideration of affinity. *Geochimica et Cosmochimica Acta* **61**, 3671-3689.

Ashworth JR, Sheplev VS, Bryxina NA, Kolobov VY, Reverdatto VV (1998) Diffusion controlled corona reaction and overstepping of equilibrium in a garnet granulite. Yenisey Ridge, Siberia. *Journal of Metamorphic Geology* **16**, 231-246.

Bolfan-Casanova N, Keppler H, Rubie DC (2000) Water partitioning between nominally anhydrous minerals in the MgO-SiO_2-H_2O system up to 24 GPa: implications fort he distribution of water in the Earth´s mantle. *Earth and Planetary Science Letters* **182**, 209-221.

Cahn JW (1959) The kinetics of cellular segregation reactions. *Acta Metallurgica* **7**, 18-28.

Carlson WD (2002) Scales of disequilibrium and rates of equilibration during metamorphism. *American Mineralogist* **87**, 185-204.

Carlson WD (2010) Dependence of reaction kinetics on H_2O activity as inferred from rates of intergranular diffusion of aluminium. *Journal of Metamorphic Geology*, doi:10/1111/j.1525-1314.2010.00886.x

Carlson WD, Gordon CL (2004) Effects of matrix grain size on the kinetics of intergranular diffusion. Journal of Metamorphic Geology **22**, 733-742.

Chakraborty S, Farver JR, Yund RA, Rubie DC (1994) Mg tracer diffusion in synthetic forsterite and San Carlos olivine as a function of P, T and fO_2. *Physics and Chemistry of Minerals* **21**, 489-500.

Chen Y, Abraham MM, Templeton LC (1977) Radiation-induced mobility of substitutional hydrogen in MgO. *Journal of the American Ceramic Society* **60**, 101-104.

De Groot SR, Mazur S (1984) Non Equilibrium Thermodynamics. New York, Dover, 544.

Dégi J, Abart R, Török K, Bali E, Wirth R, Rhede D (2009) Symplectite formation during decompression induced garnet breakdown in lower crustal mafic granulite xenoliths: mechanisms and rates. *Contributions to Mineralogy and Petrology*. doi:10.1007/s00410-009-0428-z.

Dohmen R, Chakraborty S, Becker HW (2002) Si and O diffusion in olivine and implications for characterizing plastic flow in the mantle. *Geophysical Research Letters* **29**, 2030.

Patino Douce AE, Beard JS (1994) H_2O loss from hydrous melts during fluid-absent piston cylinder experiments. *American Mineralogist* **79**, 585-588.

Fisher GW (1973) Nonequilibrum thermodynamics as a model for diffusion-controlled metamorphic processes. *American Journal of Science* **273**, 897-924.

Fisher GW (1978) Rate laws in metamorphism. *Geochimica et Cosmochimica Acta* **42**, 1035-1050.

Fisler DK, Mackwell SJ, Petsch S (1997) Grain boundary diffusion in enstatite. Physics and Chemistry of Minerals **24**, 264-273.

Frantz JD, Mao HK (1976) Bimetasomatism resulting from intergranular diffusion: I. A theoretical model for monomineralic reaction zone sequences. *American Journal of Science* **276**, 817-840.

Freund F, Wengeler H (1982) The infrared spectrum of OH-compensated defect sites in C-doped MgO and CaO single crystals. *Journal of Physics and Chemistry of Solids* **43**, 129-145.

Gardés E, Wunder B, Wirth R, Heinrich W (2011) Growth of multilayered polycrystalline reaction rims in the MgO-SiO_2 system, part I: experiments. *Contributions to Mineralogy and Petrology* **161**, 1-12.

Gardés E, Heinrich W (2010) Growth of multilayered polycristalline reaction rims in the MgO-SiO_2 system, part II: modelling. *Contributions to Mineralogy and Petrology*, doi:10.1007/s00410-010-0581-4

Götze LC, Abart R, Rybacki E, Keller LM, Petrishcheva E, Dresen G (2009) Reaction rim growth in the system MgO-Al_2O_3-SiO_2 under uniaxial stress. *Mineralogy and Petrology*. doi:10.1007/s00710-009-0080-3

Harrison LG (1961) Influence of dislocations on diffusion kinetics in solids with particular reference to alkali halides. *Transactions of the Faraday Socie*ty **57**, 1191-1199.

Holland TJB, Powell R (1998) An internally consistent thermodynamic data set for phases of petrologic interest. *Journal of Metamorphic Geology* **16**, 309-343.

Ingrin J, Pacaud L, Jaoul O (2001) Anisotropy of oxygen diffusion in diopside. *Earth and Planetary Science Letters* **192**, 347-361.

Ito M, Ganguly J (2009) Mg diffusion in CAIs: new experimental data for melilites and implications fort he Al-Mg chronometer and thermal history of CAIs. *40th Lunar and Planetary Science Conference*, 1753.pdf

Ito M, Yourimoto H, Morioka M, Nagasawa H (2001) Mg diffusion in akermanite, gehlenite and Ak30Geh70 solid solution. *Lunar and Planetary Science XXXII*:1518.

Joachim B, Gardés E, Abart R, Heinrich W (2011) Experimental growth of åkermanite reaction rims between wollastonite and monticellite: evidence for volume diffusion control. *Contributions to Mineralogy and Petrology* **161**, 389-399.

Joachim B, Gardés E, Velickov B, Abart R, Heinrich W (submitted) Experimental growth of diopside + merwinite reaction rims: the effect of water on microstructure development. *American Mineralogist*.

Joesten R (1977) Evolution of mineral assemblage zoning in diffusion metasomatism. *Geochimica et Cosmochimica Acta* **41**, 649-670.

Joesten R (1991a) Grain-boundary diffusion kinetics in silicate and oxide minerals. In: Ganguly J (ed) Diffusion, atomic ordering, and mass transport. Springer, Berlin, 345-395.

Joesten R (1991b) Kinetics of coarsening and diffusion-controlled mineral growth. In: Kerrick DM (ed) Contact metamorphism. *Reviews in Mineralogy* **26**, Washington DC, 507-582.

Joesten R, Fisher G (1988) Kinetics of diffusion-controlled mineral growth in the Christmas Mountains (Texas) contact aureole. *Geological Society of America Bulletin* **100**, 714-732.

Johnson CD, Carlson WD (1990) The origin of olivine-plagioclase coronas in metagabbros from the Adirondack Mountains, New York. *Journal of Metamorphic Geology* **8**, 697-717.

Kaur I, Mishin Y, Gust W (1995) Fundamentals of grain and interphase boundary diffusion. 3rd edition. Wiley, Chichester.

Keller LM, Abart R, Wirth R, Schmid DW, Kunze K (2006) Enhanced mass transfer through short-circuit diffusion: growth of garnet reaction rims at eclogite facies conditions. *American Mineralogist* **91**, 1024-1038.

Keller LM, Hauzenberger CA, Abart R (2007) Diffusion along interphase boundaries and ist effects on retrograde zoning pattern of metamorphic minerals. *Contributions to Mineralogy and Petrology* **154**, 205-216.

Keller LM, Wunder B, Rhede D, Wirth R (2008) Component mobility at 900°C and 18 kbar from experimentally grown coronas in a natural gabbro. *Geochimica et Cosmochimica Acta* **72**, 4307-4322.

Kirkaldy JS, Young DJ (1987) Diffusion in the condensed state. The Institute of Metals, London.

Kretz R (1983) Symbols for rock-forming minerals. *American Mineralogist* **68**, 277-279.

Laqua W (1978) Kinetics of the spinel formation reaction, a critical review. *Berichte der Deutschen Keramischen Gesellschaft* **55**, 175-180.

Lasaga AC (1983) Geospeedometry: an extension of geothermometry. Saxena, S.K. (Ed.), Kinetics and Equilibrium in Mineral Reactions, Springer, New York, 82-114.

Libowitzky E, Rossmann GR (1997) An IR absorption calibration for water in minerals. *American Mineralogist* **82**, 1111-1115.

Markl G, Foster CT, Bucher K (1998) Diffusion-controlled olivine corona textures in granitic rocks from Lofoten, Norway: calculation of Onsager diffusion coefficients, thermodynamic modelling and petrological implications. *Journal of Metamorphic Geology* **16**, 607-623.

Marquardt K, Petrishcheva E, Gardés E, Wirth R, Abart R, Heinrich W (2011) Grain boundary and volume diffusion experiments in yttrium aluminium garnet bicrystals at 1723 K: a miniaturized study. *Contributions to Mineralogy and Petrology*, doi: 10.1007/s00410-011-0622-7.

Milke R, Wiedenbeck M, Heinrich W (2001) Grain boundary diffusion of Si, Mg, and O in enstatite reaction rims: a SIMS study using isotopically doped reactants. *Contributions to Mineralogy and Petrology* **142**, 15-26.

Milke R, Heinrich W (2002) Diffusion-controlled growth of wollastonite rims between quartz and calcite: comparism between nature and experiment. *Journal of Metamorphic Geology* **20**, 467-480.

Milke R, Dohmen R, Becker HW, Wirth R (2007) Growth kinetics of enstatite reaction rims studied on nano-scale, Part I: methodology, microscopic observations and the role of water. *Contributions to Mineralogy and Petrology* **142**, 519-533.

Milke R, Abart R, Kunze K, Koch-Müller M, Schmid D, Ulmer P (2009a) Matrix rheology effects on reaction rim growth I: evidence from orthopyroxene rim growth experiments. *Journal of Metamorphic Geology* **27**, 71-82.

Milke R, Kolzer K, Koch-Müller M, Wunder B (2009b) Orthopyroxene rim growth between olivine and quartz at low temperatures (750-950°C) and low water concentration. *Contributions to Mineralogy and Petrology* **97**, 223-232.

Phillips BA, Busing WR (1956) Comparism of the infrared and raman spectra of some crystalline hydroxides. Contribution No. 1404 from the Sterling Chemistry Laboratory, Yale University, New Haven, Conneticut, **61**, 502.

Prenzel J, Abart R, Keller L (2008) Complex chemical zoning in eclogite facies garnet reaction rims: the role of grain boundary diffusion. *Contributions to Mineralogy and Petrology* **95**, 303-313.

Rossi RC, Fulrath RM (1962) Epitaxial growth of spinel by the reaction in solid state. *Journal of the American Ceramic Society* **46**, 145-149.

Ryerson FJ, Mc Keegan D (1994) Determination of oxygen self diffusion in akermanite, anorthite, diopside and spinel: implications for oxygen isotopic anomalies and the thermal histories of Ca-Al-rich inclusions. *Geochimica et Cosmochimica Acta* **17**, 3713-3734.

Schramke JA, Kerrick DM, Blencoe JG (1982) Experimental determination of the brucite = periclase + water equilibrium with a new volumetric technique. *American Mineralogist* **67**, 269-276.

Svoboda J, Fischer FD, Abart R (2010) Modelling of diffusional phase transformation in multi-component systems with stoichiometric phases. *Acta Materialia* **58**, 2905-2911.

Thomas SM, Thomas R, Davidson P, Reichart P, Koch-Müller M, Dollinger G (2008) Application of Raman spectroscopy to quantify trace water concentrations in glasses and garnets. *American Mineralogist* **93**, 1550-1557.

Thompson JB Jr (1959) Local equilibrium in metasomatic processes. In: Abelson PH (ed) Researches in geochemistry **1**, 427-457.

Truckenbrodt J, Johannes W (1999) H2O loss during piston-cylinder experiments. *American Mineralogist* **84**, 1333-1335.

Watson EB, Price JD (2001) Kinetics oft he reaction MgO + Al_2O_3 = 3 $MgAl_2O_4$ and Al-Mg interdiffusion in spinel at 1200-2000°C and 1.0 to 4.0 GPa. Geochimica et Cosmochimica Acta **66**, 2123-2138.

Warner RD, Luth WC (1973) Two-phase data for the join monticellite ($CaMgSiO_4$)-forsterite (Mg_2SiO_4): experimental results and numerical analysis. *American Mineralogist* **58**, 998-1008.

Whitney WP, Stubican VS (1971) Interdiffusion studies in the system MgO-Al_2O_3. *Journal of Physical and Chemical Solids* **32**, 305-312.

Wirth R (2004) Focused Ion Beam (FIB): A novel technology for advanced application of micro- and nanoanalysis in geosciences and applied mineralogy. *European Journal of Mineralogy* **16**, 863-876.

Yund RA (1997) Rates of grain boundary diffusion through enstatite and forsterite reaction rims. *Contributions to Mineralogy and Petrology* **126**, 224-236.

Yurimoto H, Morioka M, Nagasawa H (1989) Diffusion in single crystals of melilite: I. Oxygen. *Geochimica et Cosmochimica Acta* **53**, 2387-2394.

Zhang XY, Ganguly J, Ito M (2010) Self diffusivities of Ca and Mg in clinopyroxene: experimental studies, and planetary applications. *Lunar and Planetary Science, XXXIX* 2049.pdf.

Appendix

AI Eidesstattliche Versicherung

Hiermit versichere ich, Bastian Joachim, dass ich die vorliegende Arbeit selbstständig und ausschließlich unter Benutzung der angegebenen Hilfsmittel verfasst habe. Stellen der Arbeit, die anderen Werken wörtlich oder inhaltlich entnommen sind, wurden durch entsprechende Angaben der Quellen kenntlich gemacht. Die vorliegende Arbeit hat in dieser oder ähnlicher Form noch keiner Prüfungsbehörde vorgelegen.

Berlin, den 27.09.2011

Bastian Joachim

AII Angaben zum Eigenanteil

Die Idee zu dieser Abeit stammt von Prof. Wilhelm Heinrich und Prof. Rainer Abart. Finanziert wurde diese von der Deutschen Forschungsgemeinschaft im Rahmen der Forschergruppe 741 (nanoscale processes and geomaterial properties).

Die Planung und Durchführung der Experimente erfolgte eigenständig, wobei ich die grundsätzliche Vorgehensweise häufig mit Dr. Emmanuel Gardés diskutierte. Die Kooperation mit der Universität Innsbruck wurde durch mich eingeleitet und kam in enger Absprache mit Prof. Wilhelm Heinrich zustande.

Synthetische Startmaterialien wurden vom IKZ bereitgestellt. Zylindrische Ausgangsmaterialien stellte Matthias Kreplin her. Experimente im Pistonzylinder wurden selbstständig nach initialer Einweisung durch Dr. Bernd Wunder, IHPV-Experimente in Zusammenarbeit mit Dr. Max Wilke, Andreas Ebert und Rainer Schulz durchgeführt. Die Idee, welche zur Entwicklung eines neuen Probenhalters für die IHPV führte, stammt von Dr. Emmanuel Gardés und mir.

Die Präparation der Schliffe für Mikrosonden und IR-Analysen wurde in einzelnen Fällen von Gerhard Berger und in einem Fall von Otto Diedrich, bei einem Großteil der Proben von mir selber durchgeführt. Die Mikrosondenanalysen wurden in enger Zusammenarbeit mit Dieter Rhede und Oona Appelt durchgeführt. Bei den TEM-Analysen wurden die benötigten Folien von Anja Schreiber präpariert. Die Aufnahmen entstanden unter der Mithilfe von Dr. Richard Wirth. IR-Messungen wurden nach initialer Einweisung durch Prof. Monika Koch-Müller eigenständig von mir durchgeführt. Die Erstellung von IR-Mappings erfolgte in Kooperation mit Felix Prechtel an der Universität Innsbruck. Bei ramanspektroskopischen Untersuchungen erhielt ich Unterstützung von Nicholas Norberg.

Die in Kapitel 5 dargestellten Resultate und deren Diskussion wurden in abgewandelter Form veröffentlicht unter dem Titel: “Experimental growth of åkermanite reaction rims between wollastonite and monticellite: evidence for volume diffusion control” in der Fachzeitschrift Contributions to Mineralogy and Petrology (vol. 161, pp.389-399, 2011). Die Auswertung der Ergebnisse, sowie Idee und Ausarbeitung des Manuskriptes erfolgte eigenständig, jedoch mit Unterstützung von Prof. Wilhelm Heinrich, Prof. Rainer Abart und Dr. Emmanuel Gardés, wobei die Verbesserungsvorschläge hauptsächlich Struktur und Aufbau betrafen.

Die in Kapitel 6 dargestellten Resultate und deren Diskussion wurden in 2 verschiedenen Manuskripten bei der Fachzeitschrift American Mineralogist eingereicht (Abart R,

Petrishcheva E, Joachim B (submitted) Thermodynamic model for growth of cellular reaction rims. American Mineralogist; Joachim B, Gardés E, Velickov B, Abart R, Heinrich W (submitted) Experimental growth of diopside + merwinite reaction rims: the effect of water on microstructure development. American Mineralogist.) und befinden sich derzeit im Review-Prozess. Die Experimente und deren Auswertung wurde eigenständig, die Entwicklung des beschreibenden Models in Zusammenarbeit mit Prof. Rainer Abart und Elena Petrishcheva durchgeführt. Das Manuskript wurde eigenständig erstellt und später in zahlreichen Diskussionen mit den Co-Autoren sowohl inhaltlich als auch strukturell verbessert.

Die in Kapitel 7 beschriebene Idee, OH-gedopte Startmaterialien für Saumwachstumsexperimente zu verwenden stammt von Dr. Emmanuel Gardés und mir. Die Entwickung, Durchführung und Auswertung der Experimente wurde eigenständig vorgenommen. Bei der schriftlichen Ausarbeitung des Kapitels erhielt ich Verbesserungsvorschläge von Dr. Emmanuel Gardés.

AIII Lebenslauf

Persönliche Daten

Name:	Bastian Joachim
Geburtsdatum:	04.12.1981
Geburtsort:	Bremen
Mutter:	Renate Graul Joachim , geb. 07.01.1953
Vater:	Hans Georg Joachim, geb. 01.06.1945
Adresse:	Hochkirchstraße 3, 10829 Berlin Schöneberg

Schulbildung

07.1988-06.1992	Grundschule am Reesenbüttel, Ahrensburg
07.1992-06.2001	Gymnasium Stormarnschule, Ahrensburg
24.06.2001	Abschluss: Abitur

Ersatzdienst

01.10.2001-30.06.2002	Ersatzdienst bei der Lebenshilfe Stormarn, ev. in Ahrensburg

akademische Laufbahn

01.10.2002-15.01.2008	Studium der Geowissenschaften an der Universität Hannover.
15.01.2008	Abschluss: Diplom (Titel der Diplomarbeit: Konvektive Auflösung von Mineralen in basaltischer Schmelze)
seit 15.02.2008	Promotion im Rahmen der Forschergruppe 741 an der Freien Universität Berlin und dem GeoForschungsZentrum Potsdam mit dem Titel: Diffusion controlled growth of complex reaction rims: bridging the gap between rim growth experiments and metamorphic coronas.

Praktika

01.08.2005-30.09.2005	Praktikum am Department of Geological Sciences der University of Missouri, Columbia, USA
01.02.2007-30.04.2007	Praktikum bei Corus Research, Development & Technology, Ijmuiden, Niederlande

Auszeichnungen

- Paul-Ramdohr-Preis 2010 der Deutschen Mineralogischen Gesellschaft (DMG) für den Vortrag: Diffusion-controlled growth of monomineralic Åkermanite reaction rims in the ternary system CaO-MgO-SiO_2

- 2010 MRP Outstanding Student Paper Award für den Vortrag: Reaction rim growth in the ternary system CaO-MgO-SiO_2: Diffusion pathways and the effect of water

Mitgliedschaften

- Deutsche Mineralogische Gesellschaft (DMG)
- Österreichische Mineralogische Gesellschaft (ÖMG)
- American Geophysical union (AGU)

AIV Publications

Articles

2011

B. Joachim, E. Gardés, R. Abart, W. Heinrich (submitted) Experimental growth of diopside + merwinite reaction rims: the effect of water on microstructure development, submitted to American Mineralogist.

B. Joachim, E. Gardés, R. Abart, W. Heinrich (2011) Experimental growth of åkermanite reaction rims between wollastonite and monticellite: evidence for volume diffusion control, Contrib. Mineral. Petrol. 161:389-399.

R. Abart, E. Petrishcheva, **B. Joachim** (submitted) Thermodynamic model for growth of cellular reaction rims, submitted to American Mineralogist.

2009

A. G. Whittington, B.M. Hellwig, H. Behrens**, B. Joachim**, A. Stechern, F. Vetere (2009) The viscosity of hydrous dacitic liquids: implications for the rheology of evolving silicic magmas. Bulletin of Volcanology.

Abstracts

2011

B. Joachim, E. Gardés, W. Heinrich, R. Abart (2011), The effect of water on the internal organization of bimineralic diopside-merwinite reaction rims, European Geosciences Union General Assembly 2011, Vienna, Austria

R. Abart, E. Petrishcheva, **B. Joachim** (2011), Thermodynamic model for the growth of a cellular reaction rim, European Geosciences Union General Assembly 2011, Vienna, Austria

2010

B. Joachim, E. Gardés, W. Heinrich, R. Abart (2010), The effect of minute amounts of water on reaction rim growth kinetics.
ExperimentalMineralogyPetrologyGeochemistryXIII International Conference 2010, Toulouse, France

B. Joachim, E. Gardés, R. Abart, W. Heinrich (2010), The effect of water on component mobilities in bimineralic diopside-merwinite reaction rims,
88. Tagung der Deutschen Mineralogischen Gesellschaft, Münster, 2010.

B. Joachim, F. Prechtl, E. Gardés, R. Abart, W. Heinrich, R. Stalder (2010), The effect of minute amounts of water on reaction rim growth mechanisms,
88. Tagung der Deutschen Mineralogischen Gesellschaft, Münster, 2010.

B. Joachim, E. Gardés, R. Abart, W. Heinrich (2010): Reaction rim growth in the ternary system CaO-MgO-SiO_2: Diffusion pathways and the effect of water, American Geophysical Union (AGU) Fall meeting (San Francisco, California, USA).

R. Abart, K. Hartmann, L. Keller, **B. Joachim** (2010)
Chemical mass transfer in polycrystals and polyphase aggregates. Geocanada 2010, Calgary, Canada

G. Neusser, **B. Joachim**, E. Gardés (2010), EBSD measurements on surfaces prepared by FIB: a case study on an experimentally grown reaction rim,
88. Tagung der Deutschen Mineralogischen Gesellschaft, Münster, 2010.

2009

B. Joachim , E. Gardés, W. Heinrich, R. Abart (2009)
Diffusion controlled growth of bimineralic merwinite-diopside reaction rims between wollastonite-monticellite interfaces. European Geosciences Union General Assembly 2009, Vienna, Austria

B. Joachim , E. Gardés, R. Abart W. Heinrich, (2009)
Diffusion-controlled growth of monomineralic Åkermanite reaction rims in the ternary system CaO-MgO-SiO_2, Hallesches Jahrbuch für Geowissenschaften, 87. Tagung der Deutschen Mineralogischen Gesellschaft vom 13.-16. September 2009 an der Martin-Luther-Universität Halle-Wittenberg, Band 31, pp. 114.

B. Joachim, E. Gardés. W. Heinrich, R. Abart (2009)
Volume diffusion controlled growth of an Akermanite reaction rim in the system CaO-MgOI-SiO_2, MAPT: Micro-Analysis, Processes, Time, Edinburgh, UK, pp. 121-122

R. Abart, L. Keller, K. Hartmann, **B. Joachim**, J. Degi
A clue on the transport properties of grain- and phase boundaries in rocks, MAPT: Micro-Analysis, Processes, Time, Edinburgh, UK, pp. 58-59.

R. Abart, B. **Joachim**, I. Svoboda, F.D. Fischer (2009) A thermodynamic model for reaction rim growth in multicomponent systems, Geochimica et Cosmochimica Acta, 73, 13, Suppl. 1, A2.

E. Gardés, **B. Joachim**, W. Heinrich, R. Milke, R. Abart (2009)
Diffusion-controlled growth of forsterite and enstatite double layer between periclase and quartz: determination of MgO diffusion in forsterite and enstatite grain boundaries. European Geosciences Union General Assembly 2009, Vienna, Austria

2008

B. Joachim, E. Gardés, R. Abart, W. Heinrich (2008): Experimental growth of complex reaction rims in the system CaO-MgO-SiO2, 86. Jahrestagung der Deutschen Mineralogischen Gesellschaft (Berlin 2008), 502.

A. Quetscher, **B. Joachim**, H. Behrens, Y. Zhang (2008) Diffusive olivine dissolution in haplobasaltic melt, ExperimentalMineralogyPetrologyGeochemistryXII International Conference, Innsbruck, Austria